Study of Fast Ion Production and Confinement in Ion Cyclotron Range of Frequency Heating of Heliotron E(Dissertation_全文)

AUTHOR(S):

Okada, Hiroyuki

STUDY OF FAST ION PRODUCTION AND CONFINEMENT IN ION CYCLOTRON RANGE OF FREQUENCY HEATING OF HELIOTRON E

HIROYUKI OKADA

1999

Abstract

The ion cyclotron range of frequency (ICRF) heating is one of the most efficient heating methods for toroidally confined plasmas. While there are many heating schemes in ICRF heating, the minority-heating scheme was adopted in the Heliotron-E experiment since the study of fast ion production and confinement is particularly important for the reactor oriented research in the helical system. In the minority heating, fast minority ions are produced since the minority ions are heated selectively by the radio frequency (RF) electric field. The produced non-Maxwellian fast ions play a crucial role in ICRF heating since the heating of the bulk plasma is caused through Coulomb collisions of the fast ions with bulk plasma particles. Therefore, the production of fast ions by ICRF heating and their confinement have been investigated for Heliotron-E plasmas, and this thesis describes the results of this investigation.

For radiating ICRF waves, the twisted loop antennas for the minority heating were developed so that the antenna surface closely fitted the three-dimensional shape of Heliotron-E plasma. The plasma heating and the fast ions production were successfully carried out by using these high-field side antenna loops. High power up to 2.0 MW could be introduced into the plasma through four ports using these antenna loops. A typical experiment showed that the ion temperature increased up to about 1 keV at the line average electron density of about 2.0×10^{19} m^{-3} by the minority heating with the input power of 1.0 MW. Furthermore, the fast ions with the energy up to 100 keV were observed by a neutral particle energy analyzer designed for measuring high-energy particle fluxes.

In the fast ion production experiment, however, the rapid decay of the high-energy particle fluxes was observed just after the turn-off of the ICRF wave. It was much shorter (about one fifth) than that expected from the classical collisional processes. In order to clarify the reason for this discrepancy, a Monte Carlo code in which the acceleration, the collision and the orbit following are treated self-consistently was developed. It was found that the orbit loss affects the fast ion confinement seriously and that the efficiency of the minority ICRF heating depends significantly on the confinement of fast ions. The observed short decay times of the fast ion fluxes were explained with the orbit loss, which was enhanced by the small pitch angle scattering as well as the loss cone in the high-energy region of velocity space. It was shown that the ratio of the deposited power to the input power depends on the density and the input power. The deposition ratio by the simulation became larger as the electron density increased whereas it became smaller as the input power increased. The maximum deposition ratio of Heliotron E was estimated numerically, which was between 0.55 and 0.70 for deuterium plasmas with hydrogen-minority ions. The more efficient heating in the ^{3}He-minority case was also examined by using this code.

The production and confinement of the fast ions by the minority heating were investigated experimentally in Heliotron E and their results were explained by using the model combined with the RF acceleration, Coulomb collisions and the orbit following. The procedure of estimating the production of the high-energy ions as well as the energy deposition ratio was established for the minority heating in the helical devices. It is noted that the loss energy by orbit loss is larger than that by the energy transfer to the bulk particles by Coulomb collisions in the case where an appreciable amount of the

high-energy ions exist. The sufficiently high-density operation or the utilization of the minority species with the large ratio of the mass to the electric charge will be needed for the reduction of the orbit loss.

In conclusion, the minority heating experiments in Heliotron E were quantitatively understandable in the aspect of fast ion production and confinement by the Monte Carlo simulation code developed for heliotron and stellarator devices. This approach will be useful for the prediction and estimation of the minority heating in LHD and future helical systems.

Acknowledgments

First of all, the author would like to thank Prof. F. Sano, Prof. M. Wakatani and Prof. K. Kondo for continuous encouragement and productive suggestions in completing this thesis.

The author also wishes to acknowledge the collaboration with Prof. T. Mutoh who gave me fruitful suggestions for the ICRF experiments in Heliotron E.

The author would like to express his gratitude to Prof. M. Okamoto and Prof. M. Ohnishi for affording the opportunity of applying the Monte Carlo code to the ICRF heating analysis in Heliotron E.

The author acknowledges the discussions with Prof. H. Zushi about the experimental data of the charge exchange neutral fluxes.

It is a great pleasure to thank Prof. T. Obiki, Emeritus Prof. A. Iiyoshi, the late Emeritus Prof. K. UO and Emeritus Prof. H. Nishihara for giving me not only the opportunity to study plasma physics for fusion energy research but also the continuous encouragement to complete this thesis.

The author is grateful to heliotron staff for supporting the experiments in Heliotron E. This research would not have been conducted without their help.

Finally, the author would like to thank graduates of Nishihara seminar for the valuable discussions and the continuous encouragement.

Contents

Chapter 1
Introduction

1.1 Background of the Research

Energy consumption in the world increases continuously as the population increases rapidly. It is urgent to look for the clean and safe energy source for the future. The technology for reducing the contamination of the atmosphere and the earth due to oil and coal is being improved, however, acid rain and CO_2 problems are not resolved. Fossil materials have been still used for the main energy source. It is noted that they are limited resources and that they are not distributed uniformly in the world. In order to develop a new energy source in the 21st century, controlled thermonuclear fusion has been investigated for about a half century. In the case of deuterium fuel fusion, the resource taken from seawater has no limitation and is distributed almost uniformly [1].

Nuclear reactions relevant to fusion reactors are considered as follows [2, 3]:

$$D + D \rightarrow T(1.01\,MeV) + p(3.03\,MeV) \quad (1.1)$$

$$D + D \rightarrow {}^3He(0.82MeV) + n(2.45MeV) \quad (1.2)$$

$$D + T \rightarrow {}^4He(3.52MeV) + n(14.06MeV) \quad (1.3)$$

$$D + {}^3He \rightarrow {}^4He(3.67MeV) + p(14.67MeV) \quad (1.4)$$

$${}^6Li + n \rightarrow T + {}^4He + 4.8MeV \quad (1.5)$$

$${}^7Li + n \rightarrow T + {}^4He + n - 2.5MeV \quad (1.6)$$

The first four reactions are possible in high temperature plasmas. In the case of D-T fusion reactor, the last two are necessary in the blanket for breeding tritium. To produce the net

output power in the fusion power plant, sufficiently long confinement time is required in high-temperature and high-density plasma. This condition is called the Lawson criterion [4]. This criterion can be satisfied most easily in the D-T case [3], therefore, the fusion research is concentrated on developing the fusion reactor using deuterium and tritium as fuels. Production of high-temperature and high-density plasmas and their stable confinement are the main subjects of fusion plasma research.

Confinement methods of fusion plasma are divided into two major categories; magnetic confinement [5, 6, 7] and inertial confinement [8]. So far many types of experimental devices were constructed. Each device has merits and demerits for realizing fusion reactor. Among them, tokamaks have made striking progress in these decades and the demonstration of the production of break-even fusion plasmas is almost satisfactory in the large tokamaks such as JET [9, 10], TFTR [11, 12] and JT-60U [13, 14]. In TFTR, the peak deuteron-triton fusion power reached 10.7 MW in supershot discharges with the neutral beam injection (NBI) heating of 39.5 MW[15]. Experimental studies on alpha heating and alpha-driven instabilities have already been started in JET and TFTR. The project of the next-generation device called International Thermonuclear Experimental Reactor (ITER) [16] has been promoted as the international collaboration. In the experiment of ITER, many frontier works will be done for fusion plasma physics, material engineering, and safety assessment for the commercial fusion reactors. However, there remain a number of problems to be solved for establishing the tokamak fusion power plant even from the confinement viewpoint. The major problems are: (1) the plasma confinement properties can be extrapolated from the present tokamak plasma level to the ignited plasma level with fusion reactions? (2) the operation is reasonably stable? and so

on. For the former problem, the physics of fusion alpha particles will be important [17]. For the latter, the fueling/exhaust efficiency for hydrogen isotopes and helium ash must be controlled while the impurity density must be suppressed to give tolerable radiative power loss as well. The procedure for avoiding disruptions must be established for tokamaks.

Helical devices or stellarators have been developed as an alternative system for investigating the confinement of toroidal plasmas. It is interesting to study the different type of magnetic configurations compared with that of tokamak. In helical devices, the toroidal current, which sometimes causes the disruption in tokamaks, is not required for the formation of the confinement magnetic field. Therefore, in principle, the current-driven phenomena can be avoided for studying confinement properties [18, 19]. Thus alternative confinement schemes of a toroidal plasma are useful for understanding physical processes in tokamak plasmas.

There are many types of helical devices, for example, classical stellarator (W7-A [20], L-2 [21]), heliotron/torsatron (Heliotron D [22], Heliotron DM [23], Heliotron DR [24], Heliotron E [25], LHD [26], ATF [27], CHS [28], Uragan-2M [29]), heliac (TJ-II [30], H-1NF [31]), helias (W7-AS [32], W7-X [33]), and so on. Heliotron E belongs to the heliotron/torsatron configuration. In Heliotron E experiments, currentless plasmas are produced by applying electron cyclotron heating (ECH) to hydrogen or deuterium gas. ECH can heat electrons effectively, however, the heat transfer from electrons to ions is not efficient in the standard density range. Therefore, the direct heating method for ions is required. For this purpose, ion cyclotron range of frequency (ICRF) wave [34, 35] and/or

neutral beam injection heating [18, 36] have been adopted. This thesis mainly treats the research of the ICRF heating in Helitoron E.

ICRF heating is one of the plasma heating methods, which is widely applied to toroidal plasmas in various devices [37, 38, 39]. There are many types of heating schemes in the ICRF heating, therefore, many kinds of waves were studied and a lot of coupling apparatuses of electromagnetic or electrostatic waves (a loop antenna, a grid antenna, and so on) were tested. These are, shear Alfvén heating [40], slow wave heating [41, 42], fast wave heating [43], ion Bernstein wave heating [44] and so on. Their frequencies are on the order of 10 MHz due to the magnetic field strength of the present magnetic confinement devices. For the fusion oriented heating scheme, the application of the ICRF heating to the high-density toroidal plasma is important. For this purpose, minority heating and second harmonic heating are considered to be most suitable for tokamaks and stellarators.

The effectiveness of ICRF heating was firstly demonstrated in the Model C stellarator [42]. In this case, the ion cyclotron wave (slow wave) was utilized in the magnetic beach configuration. The ion temperature of 550 eV was reported near the end of the U bend section of the racetrack-shape vacuum chamber. 'Stix coil' antennas were installed in the straight section. This heating mode was effective for low density plasmas ($< 1.0\times10^{19}$ m^{-3}), however, the high density region of a plasma became evanescent for the propagation of this wave. Therefore, some alternative heating scheme was required for denser fusion plasmas. The use of the fast wave at the fundamental and the second harmonic of the ion cyclotron frequency in toroidal devices was first proposed by Adam and Samain [45]. In 1970s, the propagation and the heating with the fast wave were demonstrated in several

tokamaks. For example, the change of plasma loading impedance in respect to electron density due to toroidal eigenmode resonance was observed in ST tokamak [46]. The explanation of the occurrence of this resonance was that the toroidal vacuum vessel acted as a resonant cavity for the wave since the damping of fast wave was weak and the wave might propagate around the torus many times. The increment of the ion temperature (about 100 eV) was also measured in the parallel and the perpendicular directions to the magnetic field. Two-ion hybrid resonance, which must be considered in the minority-heating scheme, was discovered by Buchsbaum [47]. In the minority heating, the two ion species are contained. The minority ions, which are ordinarily a few percents of the majority ions, are heated selectively in the minority-heating scheme. Electron heating by the ICRF waves is made through a series of mode conversions followed by Landau damping. The minority heating and second harmonic heating have been utilized as the major heating methods in fusion devices.

The minority heating was also investigated the heliotron/torsatron type device such as ATF device [48]. The increment of the ion temperature was not observed in this experiment, since the plasma loading resistance was low in comparison with the vacuum loading and the RF power was also in the low range up to 200 kW. The charge exchange effect on the confinement of the fast ions whose energy was under 50 keV was studied in detail in ATF. The Fokker-Planck code with one real-space dimension was used for the analysis of the fast ions. In this calculation, the loss cone was assumed to be simple area in velocity space with minor-radius dependence.

In Heliotron E, the minority heating was started in 1984 [34, 49]. In the initial experiment, three kinds of waves such as the fast wave (minority heating), the ion

Bernstein wave and the slow wave (the ion cyclotron wave) were studied by applying them to ECH target plasmas. The coupling between the antenna and the core plasma is an important issue for the ICRF heating. The loading resistance by the antenna and plasma coupling depends on the plasma density, minority concentration, magnetic field, and so on. Experimental results were compared to the theoretical prediction with the two-dimensional wave analysis code [50]. The dependence of the resistance on these parameters in both of the experiments and calculations agreed well qualitatively. For the investigation of the coupling between an RF antenna and a plasma, a small movable antenna was made. This antenna could be rotated, therefore, the angle between the magnetic field and the RF current was changeable [51]. A numerical code based on the theory of Ref. [52] was developed, including the model of the angle between the antenna and the magnetic field. The increment of the ion temperature was about 200 eV for the input power on the order of 0.3 MW in the initial fast wave experiment. The maximum input power in this experiment was 0.55 MW. The heating efficiency $\bar{n}_e(\Delta T_i(0)+\Delta T_e(0))/P_{ICRF}$ of the minority heating by fast wave increases with density and 2.0×10^{19} $keVm^{-3}MW^{-1}$ was obtained [49], where $\bar{n}_e$ is the line density, $\Delta T_i(0)$ ($\Delta T_e(0)$) is the change of the ion (electron) temperature at the center of a plasma and P_{ICRF} is the ICRF input power.

One characteristic property of the minority heating is the formation of high-energy tail in the velocity distribution. The particle distribution realized in a thermal equilibrium is called the Maxwellian velocity distribution, which is obtained by the collisional relaxation process. When the minority heating is applied to a plasma with the Maxwellian distribution, the particles with higher energy tend to be accelerated easier by the RF

electric field since the collisions of such particles with other particles decrease. In consequence, the high-energy part of the velocity distribution in the RF heated plasma is distorted from the Maxwellian. This distorted part of the distribution function is called 'high-energy tail'. The temperature of a bulk plasma is defined as the derivative of the logarithm of the velocity distribution with respect to the energy in the lower energy range.

The production of the high-energy tail and the confinement of the resultant fast particles are important issues in the minority heating with the fast wave. The high-energy tail enhances the fusion energy output from the D-T burn plasma. The heating efficiency depends on the confinement of the high-energy ions since the bulk particles are heated via collisions with these particles. The mechanism of the production and confinement of the high-energy ions is considered to be the most important issue for the ICRF heating of the helical confinement device since there could be many types of loss regions in velocity space for these devices.

1.2 Research Objectives

There are several key issues for the ICRF heating. They are the antenna design to radiate large RF power to a plasma, the accessibility of the waves to the centeral region of a target plasma and the confinement of high-energy ions to realize efficient heating. The first objective of this thesis is to develop an ICRF antenna for the minority heating in Heliotron E in order to realize high power heating up to 0.5 MW through each heating port. The second objective, which is the main concern of this thesis, is the investigation of the production and confinement of the high-energy ions. The third one is the comparison

of the fast ion confinement in the proton-minority case with that in the ^{3}He-minority case, since D-^{3}He fusion has an advantage in designing reactors.

In the minority heating, the wave energy is mostly absorbed by minority ions. The absorbed energy is transferred from minority ions to bulk ions via Coulomb collisions. Confinement of high-energy minority ions is crucial, since the heating efficiency depends on the slowing down process of such fast ions. If they escape from the core plasma during the slowing down process, the energy-transfer rate to the bulk plasma decreases. This investigation of high-energy ions also provides an insight for the confinement of the fusion alpha particles, when the ripple loss exists.

Firstly, the behavior of fast ions produced by ICRF wave in Heliotron E has been clarified experimentally [24, 53]. As the wave energy source, the two high power ICRF transmitters were utilized. Fast neutral particles, which are produced by the charge exchange reaction between the slow neutrals and the fast ions accelerated by RF electric field, are measured by a neutral particle energy analyzer. The high-energy tail was easily produced in the low to medium density region in the minority heating experiment. The time scale of the high-energy tail production and the decay after the termination of the ICRF pulse were investigated with respect to the RF input energy and the line average electron density.

The numerical simulation is useful for interpretation of the experimental data. The Monte Carlo code named 'MOMOCO' [54] for the analysis of the high-energy ions produced by ICRF heating has been developed. The one point analytic model [55] based on Fokker-Planck equation is not sufficient for understanding the behavior of the fast particles in the three-dimensional configurations such as in Heliotron E. The orbit

following calculation, the pitch angle scattering due to Coulomb collisions and ICRF wave acceleration must be combined to understand the behavior of fast ions and the estimation of power deposition ratio. The experimental data of the fast ions in the minority-heating scheme will be analyzed by using 'MOMOCO' code, which includes all these processes.

The experiment of the ^{3}He-minority heating [56] will be discussed as the final topic of this thesis. The mass of ^{3}He is heavier than that of H or D. The mean free path of $^3He^{2+}$ ions is shorter and the gyro-radius is smaller than that of H^+ in case of the same ion temperature. Therefore, the confinement of ^{3}He is considered to be better than that of H and the higher heating efficiency in the ^{3}He-minority heating is expected. D-^{3}He fusion reaction is also expected as a candidate for the next-generation fusion concept since the neutron production can be reduced (see Eq. (1.4)). It is noted that only charged particles are created by the D-^{3}He reaction. Charged particles will be utilized for the direct generation of electric power. The D-^{3}He fusion has the possibility to reduce the severe requirement for plasma-facing materials since the neutron production can be reduced [57]. The advantage for the plasma heating will be discussed based on the experiment of the ^{3}He-minority heating in Heliotron E.

The major experimental equipment was described in Chap. 2. The ICRF heating pulse was injected into the ECH target plasma in Heliotron E. The properties of the Heliotron-E magnetic field and the ECH system were presented. The neutral particle energy analyzer (NPA) was used in order to investigate high-energy ions produced by ICRF heating. Here the features and the specifications of NPA were described. The ICRF system consisted of the transmitters, the matching circuits and the loop antennas. Among them, the most

important parts were the loop antennas. The design principle of the antenna was described and the analysis of antenna loading resistance and the matching area of the system were also discussed.

In Chap. 3, the experimental results of the heating and the fast ion production were described. The high-energy hydrogen fluxes up to 100 keV were observed in the minority-heating experiment. The confinement of the fast ions was investigated by the measurement of the decay times of the fluxes. The decay times were very short in comparison with the expected values by classical collision theory.

The analysis models for the formation and confinement of high-energy tail were described in Chap. 4. This code includes physical models of orbit following, Coulomb collision and RF acceleration processes. The analytic solutions for the collision operators were derived and compared with the numerical results.

In Chap. 5, the experimental results were explained by the physical models in Chap. 4. The orbit loss was found to be significant for the confinement of the fast ions in Heliotron E. It was also found that the combination of the orbit following and collisional processes enhanced the orbit loss in Heliotron E.

In Chap.6, the experimental result of the ^{3}He-minority heating was presented. The discussion about the heating efficiency with the Monte Carlo code was described.

International System of Units (SI) is employed throughout this thesis, except that temperatures appearing in formulae are in a unit of joules to avoid Boltzmann's constant. However, the energy and temperature are sometimes shown in electron-volts (eV) for comparison with the references. It is also noted that 'density' means 'number density' instead of 'mass density' throughout this thesis.

Chapter 2

Experimental Setup for ICRF Heating in Heliotron E

2.1 Introduction

In this chapter, the Heliotron-E device is described from the point of view of the ICRF heating experiment. Heliotron E is a plasma confinement device with the helical heliotron magnetic field. A currentless plasma can be produced in order to study high-energy particle confinement without major current disruption. ECH system is used for making breakdown of filling hydrogen gas in the vacuum chamber. The electron temperature increases with an increase in the ECH power. Ions are heated up via Coulomb collisions with fast electrons in the initial plasma production phase, whereas the ion temperature is much lower than the electron temperature.

For the experimental analysis of the ICRF heating, the diagnostics of high-energy neutral particles are crucial under the condition where the high-energy neutral particles are emitted by the charge exchange reaction of plasma ions with hydrogen atoms. For this purpose, a neutral particle energy analyze (NPA) is prepared. The characteristics of NPA are described in Sec. 2.4.

The ICRF heating system, which is essential for the production of the fast ions with the energy beyond 30 keV in Heliotron E, is described in Sec. 2.5. Since the energy of fast ions injected by neutral beams is lower than 30 keV, these fast ions can be produced only by the ICRF heating. Two transmitters were used for Heliotron E. Each of them can deliver RF output power of 1.5 MW. The antenna design is one of the most important

issues for the ICRF heating in toroidal plasmas such as tokamaks and heliotrons. The design concept of the antenna for Heliotron E is presented. A brief summary is given in Sec. 2.6.

2.2 The Heliotron-E Device

Heliotron E was completed in 1980 for the 'proof of principle' experiments of the heliotron configuration [25]. It has the major radius of 2.2 m and the elliptic plasma cross section with the area of $\pi \times 0.3\ \mathrm{m} \times 0.15\ \mathrm{m}$. The heliotron configuration is produced by (1) the helical coil with the magnetic pole number $\ell = 2$ and the pitch number $\kappa = 9.5$ and (2) a pair of vertical coils. The maximum field strength at the magnetic axis is 2.0 T. It is noted that the magnetic surfaces can be produced without a net plasma current. Therefore, the plasma behavior without the net plasma current can be studied in this device. A schematic view of Heliotron E is shown in Fig. 2.1. As for the optional control of the magnetic configuration, there are nineteen toroidal coils, which are not drawn in this figure, since the standard magnetic configuration used for studying the ICRF heating is produced without the toroidal coils. The vacuum chamber is made of stainless steel of 0.03 m in thickness. An example of the poloidal cross section of magnetic flux surfaces is shown in Fig. 2.2 which shows the position of the helical coil and the chamber wall. In Fig.2.2, this toroidal angle corresponds to the position of the ICRF antenna port. The Heliotron-E magnetic configuration [58] is characterized by a large rotational transform and a strong magnetic shear near the outermost flux surface as shown in Fig. 2.3. The rotational transform, ι, has the minimum value of about 0.51 on the axis and the maximum value of about 2.5 at the

outermost magnetic flux surface. Here the approximate profile of the rotational transform is given by Eq. (4.43) in Chap. 4. The magnetic shear parameter, Θ, reaches 0.5 at the plasma edge. In order to produce the large rotational transform, the magnetic field has the large helical ripple $\varepsilon_h \cong 0.3$ in the edge region. This helical ripple generates trapped particles whose number fraction is on the order of $\sqrt{\varepsilon_h}$. Trapped particles affect the transport in the collisionless regime. The contribution of the trapped particles is important for the estimation of the neoclassical diffusion coefficient of the bulk plasma in this regime [59, 60]. When we consider the confinement of the high-energy ions, the velocity space loss region can be determined from the trapped particles with the various orbit types.

2.3 Electron Cyclotron Heating (ECH) System for Plasma Production and Heating

In Heliotron-E experiments, initial plasmas are usually produced by ECH [18, 34]. The parameters of the gyrotorn tubes are shown in Table 2.1. Since the wave frequency of ECH is high, the wave power can be introduced into a plasma confinement device with the waveguide. The gyrotron power is injected through the window attached to the port #13.5 of the vacuum chamber. The arrangement of the heating and diagnostic systems in the ICRF experiments is shown in Fig.3.4 in Sec. 3.2. The mode of gyrotron output wave is the TE_{02} circular polarized mode, therefore both the ordinary (O) mode and the extra-ordinary (X) mode are transmitted simultaneously. Since the ECH power is injected from the weak field side of Helitoron E, the X mode component is reflected at the right-hand cutoff layer. This wave is reflected at the chamber wall surface several times. After these reflections at the wall surface, the mode can be changed from the X

mode to the O mode. Finally, nearly all of the wave power is expected to be absorbed since the reflection ratio at the wall surface is considered to be greater than 0.9. However, for high-density plasmas, the absorption ratio of the wave power decreases. In this case, the cutoff of the O mode appears inside the plasma, and the wave cannot reach the central region.

2.4 Neutral Particle Energy Analyzer (NPA) for Measuring Fast Ion Energy Spectrum

The neutral particle fluxes are measured by NPA [61]. Since neutral particles exist even in the central region of a plasma with high temperature due to cascade charge exchange reactions, the bulk ions can be neutralized and the resultant neutrals escape from the plasma. The production rate of neutral particles per unit volume is given by $n_i n_0 \langle \sigma_{CX} v \rangle$, where n_i is the ion density, n_0 is the neutral density, σ_{CX} is the cross section of charge exchange reaction and $\langle \sigma_{CX} v \rangle$ is the charge exchange reaction rate. The values with brackets denote the average value over the velocity distribution. The measured neutral flux by NPA is proportional to $\int \Delta\Omega n_i n_0 \sigma_{CX} \left(2E/m_i \right)^{\frac{1}{2}} E^{\frac{1}{2}} f_i \Delta E d\ell$, where $\Delta\Omega$ is the solid angle of NPA aperture, E is the energy of the detector channel of the NPA, m_i is the ion mass, $f_i(v)$ is the velocity distribution of the ions, ΔE is the energy resolution of the detector channel, and the integration is made along the line of sight. When the bulk ion temperature, T_i, is estimated from the NPA data, the Maxwellian distribution is assumed, i.e. $f_i(v) = (m_i/2\pi T_i)^{3/2} \exp(-m_i v^2/2T_i)$, where v is the velocity of the bulk ion ($E = m_i v^2/2$).

A schematic view of the NPA is shown in Fig. 2.4. The NPA analyzes the energy and mass of the escaped neutral particle. This analyzer is the type of E//B. Here, the directions of the magnetic and the electric fields are parallel. The neutral particles are reionized in a cold gas cell, and they are guided into the magnet field of the bending magnet. Singly charged ions are dominant among the ions produced in the gas cell. Ion trajectories in the bending magnet depend on the product of mass and energy. The deflecting electrodes separate ion trajectories based on particle energy. The analyzer has 20 detectors for protons and deuterons. The energy resolution is estimated as 6.3% at the channel corresponding to 80 keV. This diagnostic device observes the hydrogen neutral fluxes with the pitch angle from $7\pi/18$ to $5\pi/9$ rad along the given line of sight. Another NPA is used to determine the bulk ion temperature [62] from the deuteron fluxes. The number of the detector channels is 10. The measurable energy range is from 0.1 to 25 keV for deuterium atoms and the energy resolution is in the range of 10 to 25%. The energy spectra obtained by these two NPAs provide important information about the fast ion behavior in the ICRF experiments.

2.5 ICRF Heating System

2.5.1 ICRF Transmitter

ICRF heating system consists of transmitters, matching circuits and antennas. In Heliotron E, two transmitter sets for ICRF heating [24, 35] are installed. Each can deliver 1.5 MW power with the 0.2-sec pulse. The ICRF system is shown in Fig. 2.5. The initial oscillator is a signal generator (SG) with a small output power. This output is

introduced to the four cascade power amplifiers in Fig. 2.5. Parameters of ICRF amplifier system are summarized in Table 2.2. Three vacuum tube amplifiers are the grid grounded tuning type. The main amplifier has the distributed-circuit cavity made by Thomson CSF [63]. With these components, the transmitter has a wide power range and a wide frequency band width. The frequency range of 17.8 - 53.4 MHz is chosen for studying various ICRF heating methods such as minority heating with hydrogen or helium minority, second-harmonic heating and slow-mode ion cyclotron wave heating. The pre-amplifier II and the driver amplifier use the LC oscillating circuit with the vacuum variable condenser and Lecher lines. The power is transmitted by the co-axial copper lines from the main amplifier to the Heliotron-E experimental room. The diameter of the co-axial line is 0.152 m and the characteristic impedance is 50 Ω. Since ICRF antennas and these transmission lines have different impedances, a matching circuit is required. One matching circuit consists of a serial and a parallel vacuum variable condensers (System I). Two stub tuners by the distributed constant circuit are used for the other matching circuit (System II). To avoid the DC coupling between ICRF transmitters and the Heliotron-E device, DC cuts are installed between the main amplifiers and the matching circuits. In the transmission line between the matching circuit and the ICRF antenna, the standing wave appears. The voltage in this section becomes very high compared to that between the transmitter and the matching circuit. Thus the larger co-axial line (0.203 m in diameter) which is filled with SF_6 gas are used to suppress breakdown.

2.5.2 Voltage Distribution in Matching Circuit with Antenna Vacuum Feedthrough

The breakdown problem of the vacuum feedthrough and transmission line must be solved in order to establish the effective coupling between the ICRF waves and the magnetically confined plasmas [64]. Here the critical components are the vacuum feedthrough and the vacuum variable condenser. The maximum rated voltage of the condenser is 33 kV at the peak. While there is little information for designing the vacuum feedthrough in this frequency range, the special design of the matching circuit and feedthrough is required in order to avoid breakdown. The main purpose of this design is to keep the voltage as low as possible at the matching condensers (stub tuners) and feedthroughs in order to introduce the RF power of 1 MW per a transmitter into the antennas. The voltage and current in the circuit are calculated according to Ref. [65]. The voltage at x = 0 is denoted as V_0, the current as I_0, and the impedance as Z_0 (see Fig. 2.6(a)). These parameters at x = s are represented to be

$$V_s = V_0 \cos(\beta s) + iWI_0 \sin(\beta s), \tag{2.1}$$

$$I_s = i\frac{V_0}{W}\sin(\beta s) + I_0 \cos(\beta s), \tag{2.2}$$

$$Z_s = W\frac{\frac{Z_0}{W} + i\tan(\beta s)}{1 + i\frac{Z_0}{W}\tan(\beta s)}, \tag{2.3}$$

where W (= 50 Ω) is the characteristic impedance, β is the wave number ($\beta = 2\pi/\lambda$, λ:wavelength) and $i = \sqrt{-1}$. Here the time dependent parts of the each variable ($e^{-i\omega t}$) are omitted. RF voltage V_a at the connection point of the antenna is calculated from the antenna impedance Z_a and ICRF power P_{RF},

$$Z_a = R_a + iX_a, \tag{2.4}$$

$$|V_a| = \sqrt{\frac{R_a^2 + X_a^2}{R_a} P_{RF}}\ , \tag{2.5}$$

where R_a is the resistance and X_a is the reactance of the antenna impedance.

A large value of R_a is preferable because V_a should be small under the condition that X_a is much larger than R_a for a fixed P_{RF} value. This condition is usually satisfied in the ICRF heating device. The impedance of the serial and parallel condensers can be calculated easily. (Z_{D_1}, Z_{D_2}) or (Z_{E_1}, Z_{E_2}) for the each element are used as shown in Fig. 2.6(b) with the following relations:

Parallel condenser: $$\frac{1}{Z_{D_2}} = \frac{1}{Z_{D_1}} + i\omega C_1, \tag{2.6}$$

Serial condenser: $$Z_{E_2} = Z_{E_1} + \frac{1}{i\omega C_2}, \tag{2.7}$$

Stub Tuner by the distributed constant circuit:

$$\frac{1}{Z_{D_2 \text{ or } E_2}} = \frac{1}{Z_{D_1 \text{ or } E_1}} + \frac{1}{iW \tan(\beta \ell_{s_1 \text{ or } s_2})}. \tag{2.8}$$

Here C_1 and C_2 are the capacitances of the condensers and ℓ_{s_1} and ℓ_{s_2} are the electric lengths of the stub tuners of 1 and 2, respectively. To minimize the reflected power, the impedance Z_{E_2} must be tuned to be W = 50 Ω. An expected antenna resistance is in the range of 1 to 5 Ω. A variable range for the electric length between the components such as the condensers must be determined to obtain the matching condition with the antenna impedance. For the circuit systems I and II in Fig. 2.6(b), the specifications are given in Table 2.3. The range of the tunable antenna impedance is visualized on the Smith charts [65] as shown in Figs. 2.7 (a) and 2.7(b). The range of the experimental antenna impedance is also presented as the area surrounded by the solid line.

An example of the voltage distribution is shown in Fig. 2.8 for the system I. The measured antenna impedance (Z_a = (0.97 Ω, 23.0 Ω) for a pair of antennas) in the ICRF experiment is used for calculating the voltage distribution. As a consequence, the voltages at the condensers for 0.8 MW level ICRF heating are sufficiently low compared with the specification of the transmission system.

2.5.3 ICRF Antenna for the Heliotron-E Device

The ICRF antenna as a radiating system of the electromagnetic wave is one of the most important components of the ICRF heating apparatus. Electromagnetic waves in the frequency range of 15 - 50 MHz can not be radiated from a waveguide as in the case of ECH. The wave characteristics of ICRF will be explained in Sec. 3.2. The first demonstration of the high power ICRF heating was carried out in the Model C stellarator using the Stix coil as described in Sec. 1.1. Single or half-turn loop antennas were installed in ST [46], TFR [66] and DIVA [67] for exciting a fast wave. At the beginning of the ICRF experiments of Heliotron E, however, there was little experimental data of ICRF antennas in helical devices. The half-turn type was adopted after the R&D in Heliotron DR [68] preceding the ICRF experiments in Heliotron E since it was most effective for the fast wave excitation.

Key issues for the ICRF antenna development are as follows:

(1) The antenna resistance, when a plasma is loaded, should be sufficiently large to reduce the voltage at the feedthrough.

(2) The net plasma loading resistance should be large compared with the antenna resistance without a plasma. If this condition is not satisfied, the most RF power is

dissipated through Joule loss in the antenna loop.

(3) The impurity emission from the antenna structure into the core plasma should be avoided. Protection of the antenna structure from the heat and particle fluxes should be taken into account in the design of the antenna.

As for the issue (2), Joule loss in each antenna loop of about 4 mΩ calculated from the stainless-steel resistivity is considered to be negligibly small. The practical value of the antenna impedance without a plasma is much larger as mentioned later since the RF power is radiated even in the vacuum and there is a contact resistance at the junction of the component.

As for the issues of (1) and (2), the antenna impedance was calculated using Adam's model [69] with the experimental parameters in the beginning of the experiment. This model is useful for the survey of the antenna design parameters. The geometry of this model is shown in Fig. 2.9. A plasma is located in the region of $x < x_D$, and the RF current flows in the y direction at $x = x_2$. The ideal conductor wall is situated at $x = x_3$. In this geometry, the antenna impedance is expressed separately for the resistive part (R_a) and the reactive part (X_a),

$$\frac{R_a}{L} = \frac{\omega}{10^9}\int_{-\infty}^{+\infty}\frac{\sin k_z w/2}{k_z w/2}\cdot\frac{\gamma k_x \cos k_z z}{(k_z\beta_+)^2+(k_x\beta_-)^2}\left[\alpha_+\beta_- - \alpha_-\beta_+\right]dk_z, \qquad (2.9)$$

$$\frac{X_a}{L} = \frac{\omega}{10^9}\int_{-\infty}^{+\infty}\frac{\sin k_z w/2}{k_z w/2}\cdot\frac{\gamma k_z \cos k_z z}{(k_z\beta_+)^2+(k_x\beta_-)^2}\left[\alpha_+\beta_+ + \frac{k_x^2\alpha_-\beta_-}{k_z^2}\right]dk_z, \qquad (2.10)$$

where L is the length of the antenna in the y direction, k_z is the wave number in the magnetic field direction or the z direction, w is the width of the antenna in the z direction and k_x is the component of the wave number in the x direction. In Eq. (2.9) and

Eq. (2.10), $\alpha_\pm, \beta_\pm$ and γ are defined as follows:

$$\alpha_\pm = e^{k_z(x_2-x_1)} \pm e^{-k_z(x_2-x_1)}, \qquad (2.11)$$

$$\beta_\pm = e^{k_z(x_3-x_1)} \pm e^{-k_z(x_3-x_1)}, \qquad (2.12)$$

$$\gamma = e^{k_z(x_3-x_2)} - e^{-k_z(x_3-x_2)}. \qquad (2.13)$$

From this formula, our antenna resistance is in the range of 1 - 5 Ω and the reactance is about 10 - 30 Ω. The voltage calculated from Eq. (2.5) is 15 kV for the case of 2 Ω resistance, 30 Ω reactance and 1 MW RF power. This voltage is sufficiently small compared with the specifications of the vacuum variable condensers in the matching circuit and the vacuum feedthough.

The ICRF antenna for the Heliotron-E device consists of the central conductor, the return conductor, the side limiters and the double-layer Faraday screen. To suppress the parallel RF field and protect the antenna loops from the particle fluxes, the antenna has a Faraday screen [70]. Since the magnetic field line crossed the antenna structure in the Heliotron-E configuration, the double-layer Faraday screen was selected as shown in Fig. 2.10. The outer and inner screens are made of titanium and stainless steel, respectively. The antenna strap is also made of stainless steel. The graphite plates are installed on both sides of each pair of antennas for the protection of the whole antenna structure from the charged particle fluxes along the magnetic field line. A photograph of the antenna structure is shown in Fig. 2.11. The twisted structure of the antenna is designed for facing the helically distorted plasma shape. The distance between the plasma and the antenna is designed to be kept constant. The loading resistance of the antenna can be increased owing to the decreased effective distance between the plasma and the antenna. Therefore, such a complicated shaping was required in order to obtain sufficiently large

loading resistance without the impurity contamination. This three-dimensional structure characterized the ICRF antenna for Heliotron E while simply curved antennas are used in tokamaks. This type antenna was also utilized in the fast wave experiment in CHS [71].

Both ICRF transmitters can generate the maximum RF power of 1.5 MW for a period of 0.2 sec. The RF power can be fed to the four pairs of ICRF antennas through the vacuum feedthroughs from the horizontal ports. Since two pairs of antennas (four antenna straps) are connected to one transmitter, the total number of antenna straps is eight. These antennas are designed for the fast wave heating and are positioned outside the last closed magnetic surface. The distance between the last closed magnetic surface and the antenna Faraday screen is about 1 cm. Most part of the antenna loop is set on the high field side, since the waves reach the two-ion hybrid resonance layer after crossing the right-hand cutoff layer in the edge region as shown in Fig. 3.1.

The resistance of a pair of the antennas without the plasma was about 0.2 Ω. The increment of the resistance with the plasma was typically 1 Ω. This increment of the resistance is mainly due to the resistivity of the plasma. The antenna current is fed through the outer horizontal port and the pair of the antenna loops is installed on the wall on upper or lower high-field side (see Fig. 2.2, only the lower antenna is illustrated). The antenna parameters are summarized in Table 2.4. In typical ICRF experiments, the ICRF power up to 1.0 MW was injected through the vacuum feedthroughs (see Fig. 3.4). The maximum input power of 2 MW was injected by using the eight antenna loops from four feedthroughs. About 70% of the input power were radiated from the antennas to the Heliotron-E plasma. The arc spots inside the antenna were not found after the ICRF

experiments. The charged particle penetration into the antenna was found to be successfully suppressed by the double-layer Faraday screen.

2.6 Summary

The Heliotron-E device utilizes the $\ell = 2$, m = 19 helical coil and a pair of vertical field coils to obtain the standard magnetic configuration for plasma confinement without a net plasma current. For ICRF heating experiments, a target plasma was initiated by ECH pulse, which was injected from 1 - 4 gyrotrons with the frequency of 53.2 GHz and the output power of 0.2 MW/tube. The two transmitters of ICRF heating with the frequency of 17.8 - 53.4 MHz and the output power of 1.5 MW/transmitter were equipped. ICRF pulse was applied to the plasma maintained by ECH. The produced fast ions by the ICRF heating were measured by NPA. This diagnostic was applicable for the fast ion measurement in the range up to the 100 keV.

The ICRF antennas for the ICRF heating of Heliotron-E plasmas have been carefully designed. It was necessary to obtain the antenna resistance in the range of 1 - 5 Ω for the efficient heating. To avoid the breakdown in the components of the transmission line, the antenna resistance must be kept large. By the analysis according to Adam's model, this condition was predicted to be satisfied under the design parameters of the developed twisted loop antennas. The predicted resistance of the antennas (> 1 Ω for each antenna loop) was attained experimentally under the Heliotron-E circumstances. It was demonstrated that the developed twisted structure makes it possible to optimize the distance between the antenna and the plasma edge without the increment of the impurity contamination. In the tokamak case, only a simply curved antenna would be enough

since the last closed magnetic surface of the tokamak configuration has the toroidal symmetry. In the Heliotron-E experiment, the elaborate antenna design was necessary and its performance was found to be encouraging, providing a valuable guideline for developing ICRF antennas for large-scale devices such as LHD [72]. The double-layer Faraday screen was useful to avoid charged particle penetration into the antenna loop. The maximum input power reached 2 MW with the eight antenna loops from four vacuum feedthroughs. In order to maximize RF loading, the phase array antennas might be useful. It was noted that the electron density control is difficult in the high power region in the Heliotron-E experiment since the impurity penetration actually occurred near the antenna. One candidate for the suppression of the impurity is the phase control (in-phased or out-of-phased excitation) of the current in the array antenna [73]. For helical devices, the wide antenna with the four RF feeders has been tested in WS-7AS in order to control $k_{//}$ [74]. Such a design study remains as a future work.

Gyrotron Tube	Varian VGE 8053 × 4
Output Power	200 kW/tube
Frequency	53.2 GHz
Pulse Width	200 ms
Mode	TE_{02}
Transmission Loss	2-3%

Table 2.1. Parameters of ECH system in Heliotron E.

	Signal Generator	Pre. Amp. I	Pre. Amp. II	Driver Amp.	Main Amp.
Vacuum Tube	(SG, MG523B)	(Transistor Amp., ENI3200L)	4CX5000A	4CW100000E	TH518
Cooling	Air	Air	Air	Water	Water
RF Input	--	0 dBm	200 W	4 kW	75 kW
RF Output	0 dBm	200 W	4 kW	75 kW	1.5 MW
Power Gain	--	53 dB	13 dB	12.7 dB	13 dB
Coaxial Line	RG-55/U	RG-8/U	RG-8/U	WX-77D	WX-152D

Table 2.2. Parameters of ICRF amplifier system.

System I

	C_1(pF)	C_2(pF)
minimum	34.2	50.0
maximum	675.7	255.9

System II

	ℓ_{S_1} (λ at 26.7MHz)	ℓ_{S_2} (λ at 26.7MHz)
minimum	0.5307	0.4184
maximum	0.7356	0.4999

Table 2.3. Specification of matching circuit systems, system I and system II.

Number of antenna loops	8
Area of the current strap of each antenna	486 x 50 mm^2
Material of the antenna	Stainless steel
Double-layer Faraday screen	Inner one is made of stainless steel; outer one of titanium
Side protectors	Graphite tiles
Resistance without the plasma of each pair of antennas	0.2 Ω
Phase between the two antenna straps	0 rad

Table 2.4. Antenna Parameters

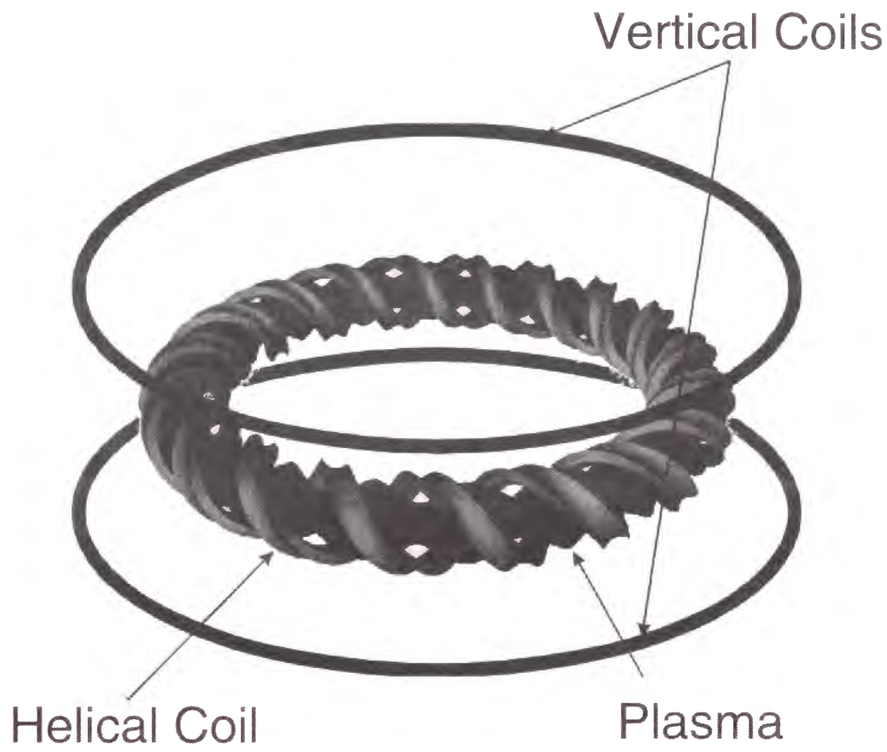

Fig. 2.1. A schematic view of the Heliotron-E device. In this figure, the coil system used in the standard configuration and the plasma shape are illustrated. The major radius and the average minor radius of Heliotron E are 2.2 m and 0.2 m, respectively. The maximum magnetic field strength at the magnetic axis is 2.0 T.

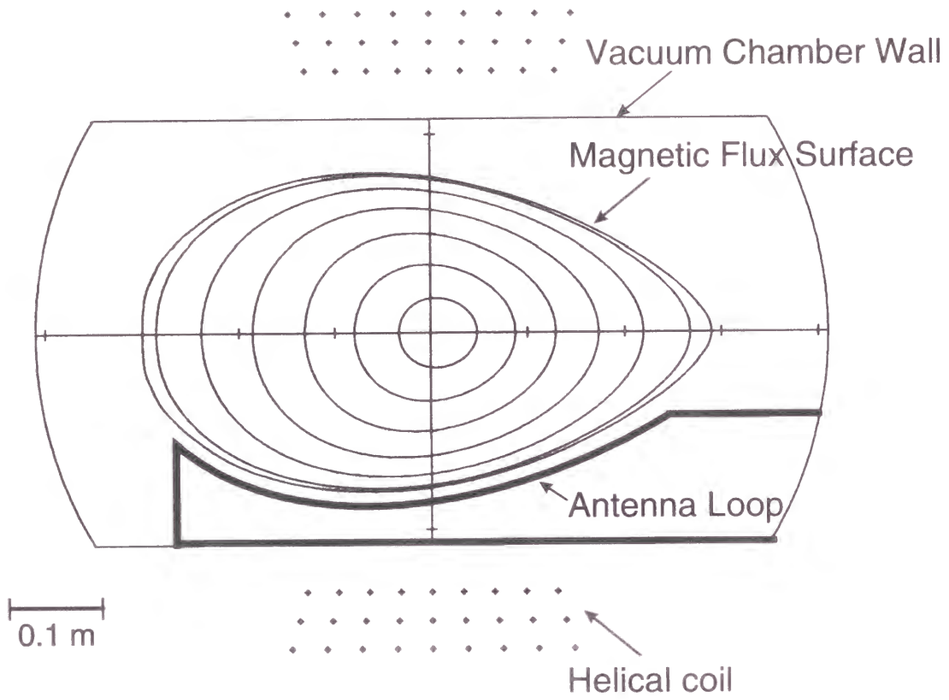

Fig. 2.2. Poloidal cross section of magnetic flux surfaces are shown at the toroidal position where the helical coils are located on the top and bottom outside the vacuum chamber.

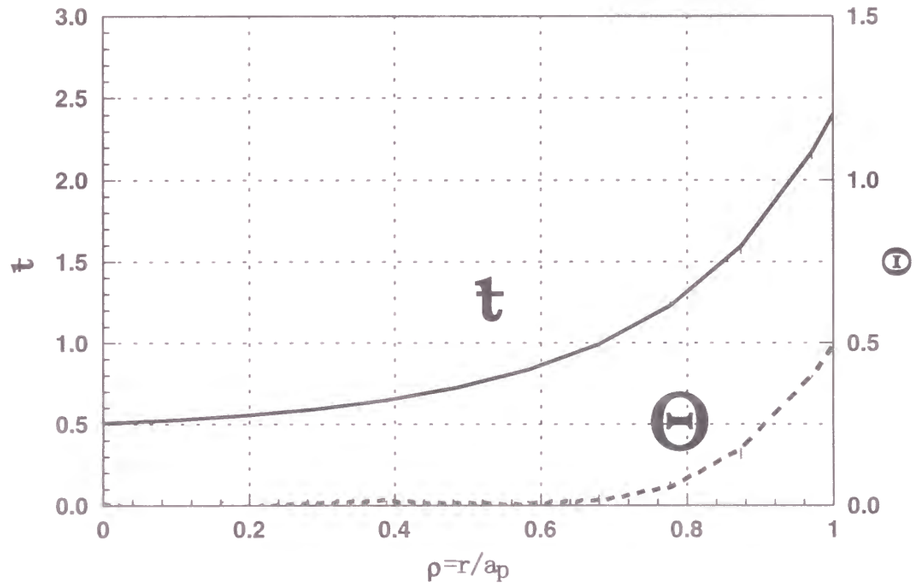

Fig. 2.3. Rotational transform and magnetic shear profiles of the standard Heliotron-E magnetic configuration.

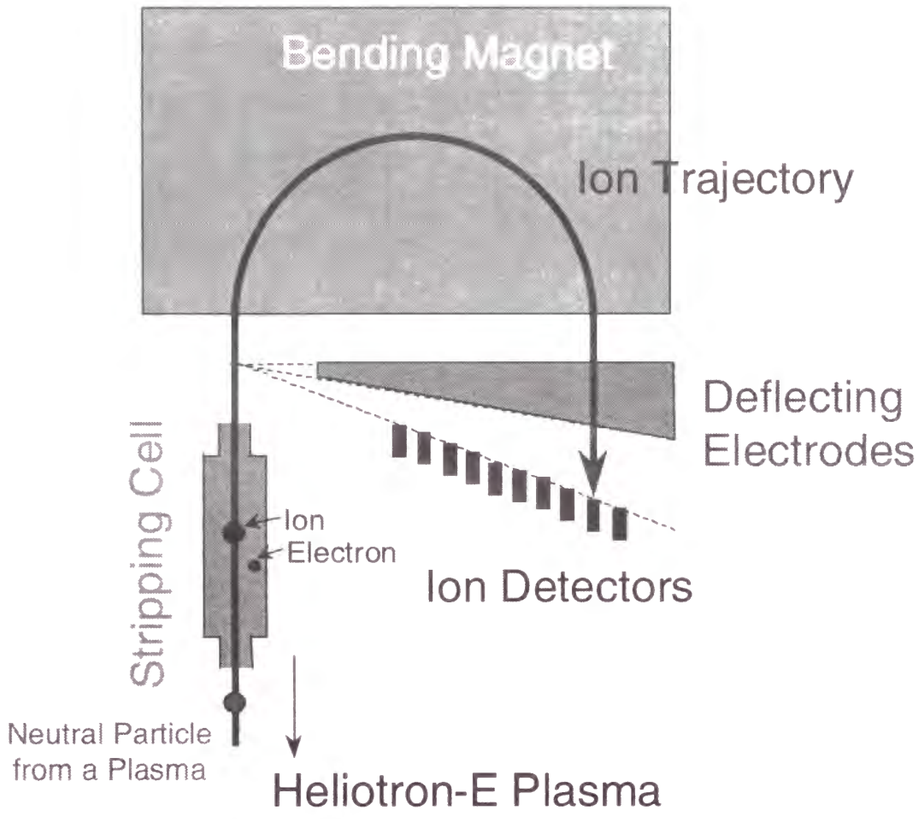

Fig. 2.4. A schematic view of neutral particle energy analyzer (NPA). This diagnostic device consists of a stripping cell, a bending magnet, deflecting electrodes and ion detectors.

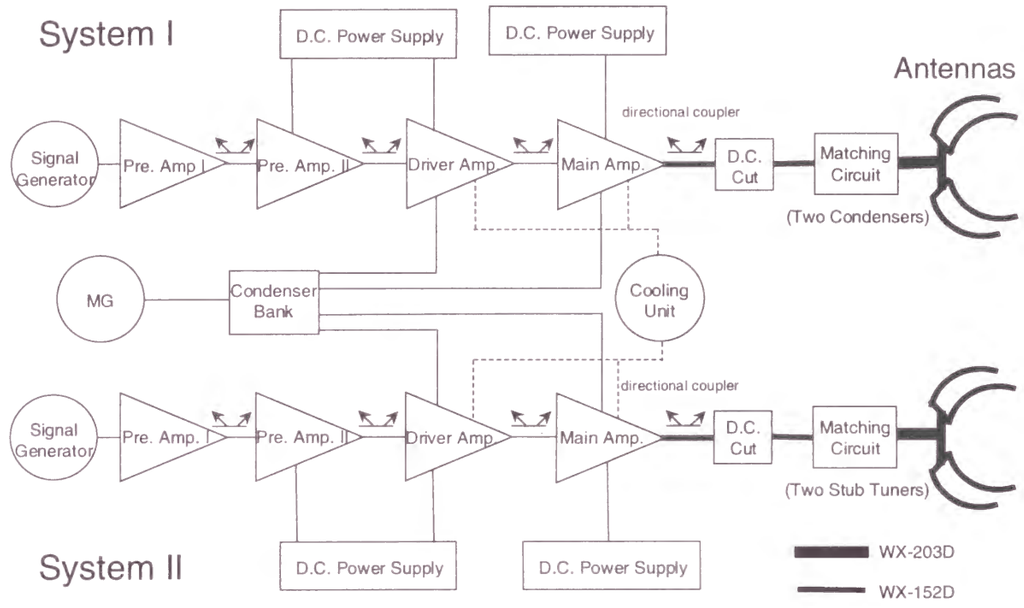

Fig. 2.5. ICRF system diagram for Heliotron E. Two sets of transmitter are installed. Each has power transmission capability of 1.5 MW with a pulse width of up to 0.2 sec.

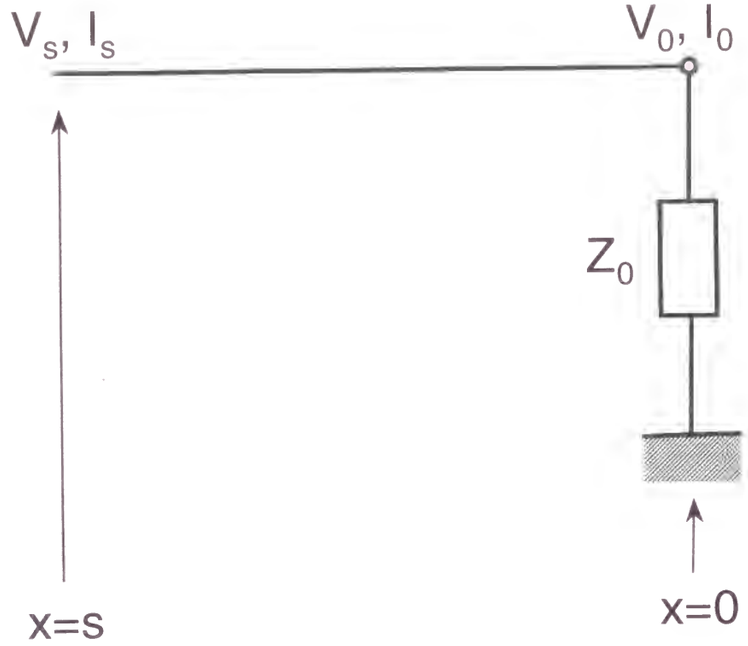

Fig. 2.6(a). A basic model to calculate the voltage and current in the distributed constant circuit. Z_0, V_0 and I_0 are the impedance, the voltage and the current at the point x = 0, respectively.

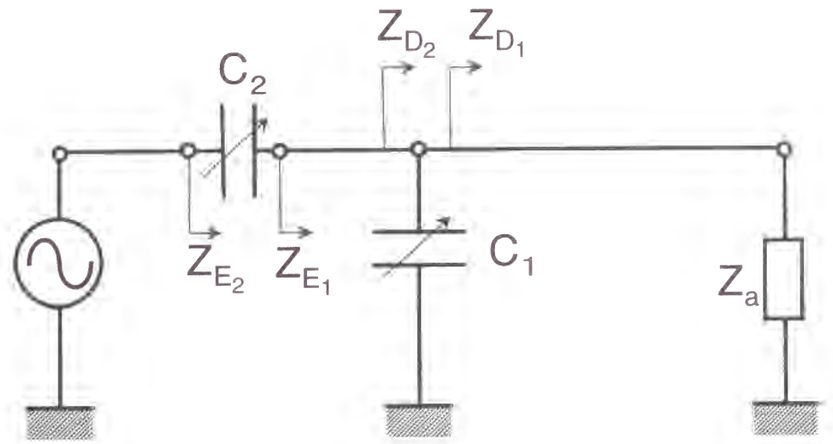

SYSTEM I

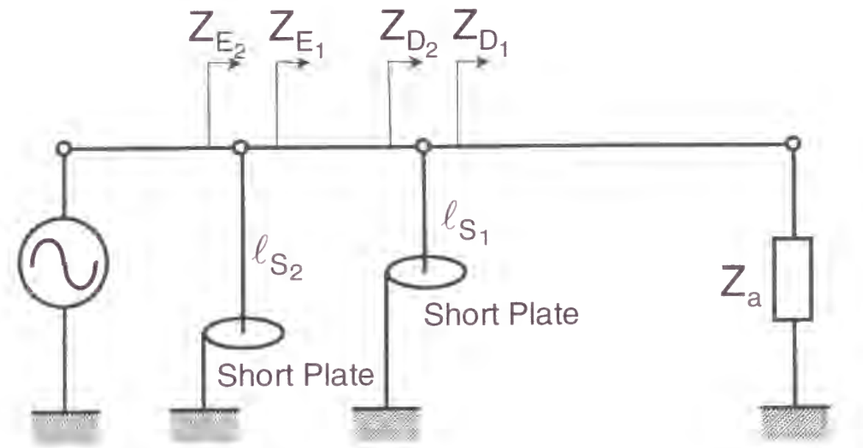

SYSTEM II

Fig. 2.6(b). Two types of circuit system. The upper type has two vacuum condensers as a matching circuit. Impedance variables (Z_{D_1}, Z_{D_2}) and (Z_{E_1}, Z_{E_2}) are defined on the both sides of each condenser. The lower circuit has two stub tuners by the distributed constant circuit. The impedance variables are also defined on the both sides of each stub tuner.

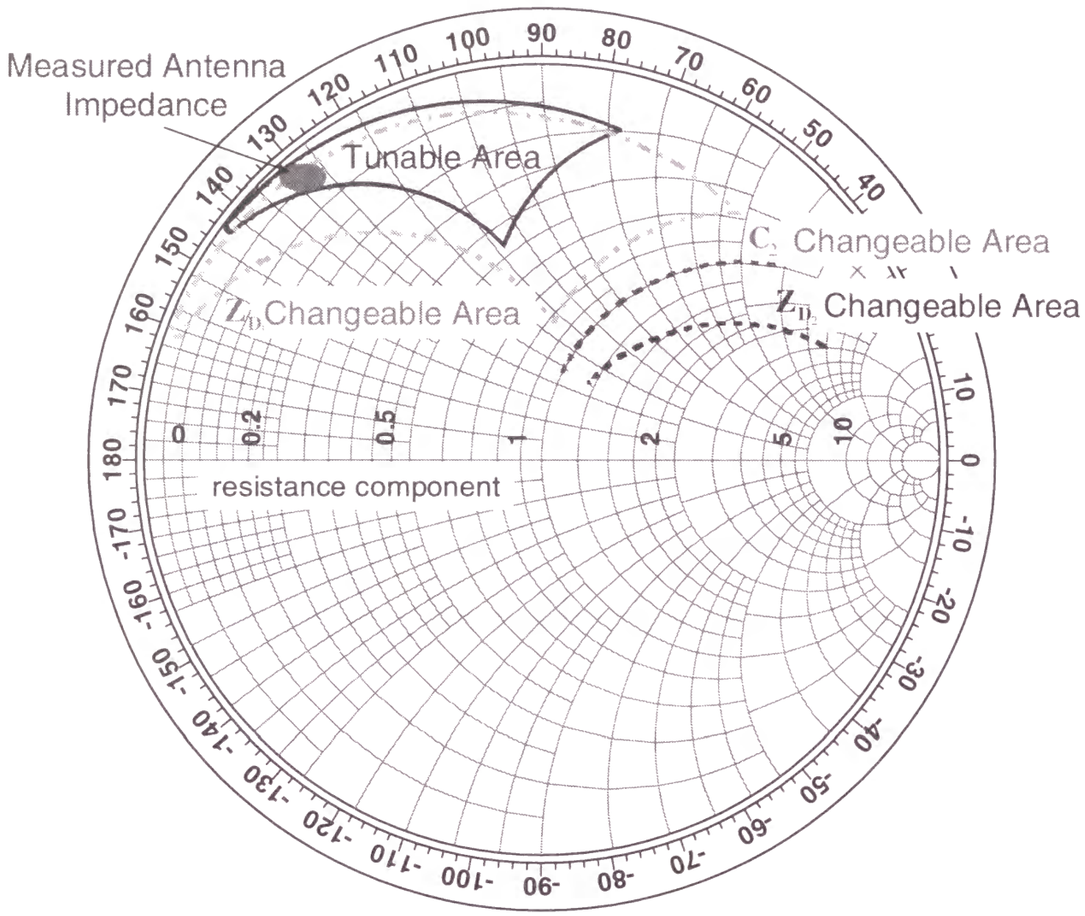

Fig. 2.7(a). The Smith chart of the circuit system I in Fig. 2.6(b). The area surrounded by the solid line shows the tunable area of the loading impedance. The area surrounded by the dash-dotted line corresponds to the impedance range of Z_{D1}. The sizes of these two areas are different because the transmission line is branched into two at the point between Z_{D1} and Z_a.

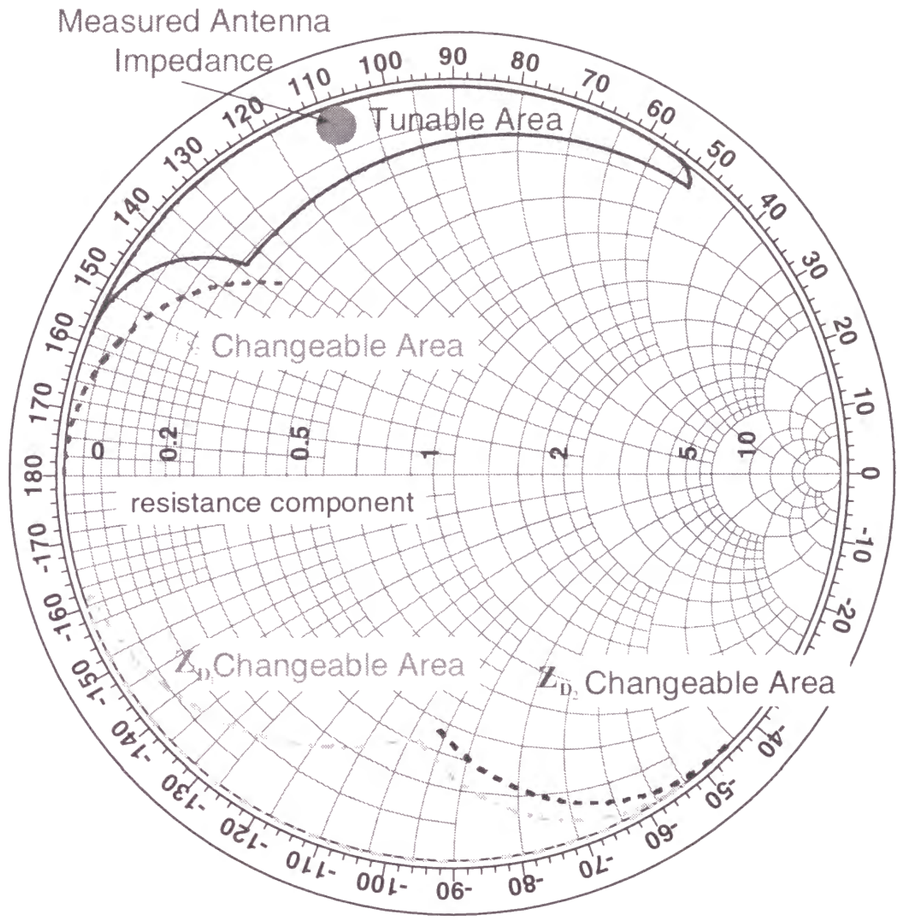

Fig. 2.7(b). The Smith chart of the circuit system II in Fig. 2.6(b). The area surrounded by the solid line shows the tunable area of the antenna impedance. The area surrounded by the dash-dotted line corresponds to the impedance range of Z_{D1}. The sizes of these two areas are different because the transmission line is branched into two at the point between Z_{D1} and Z_a.

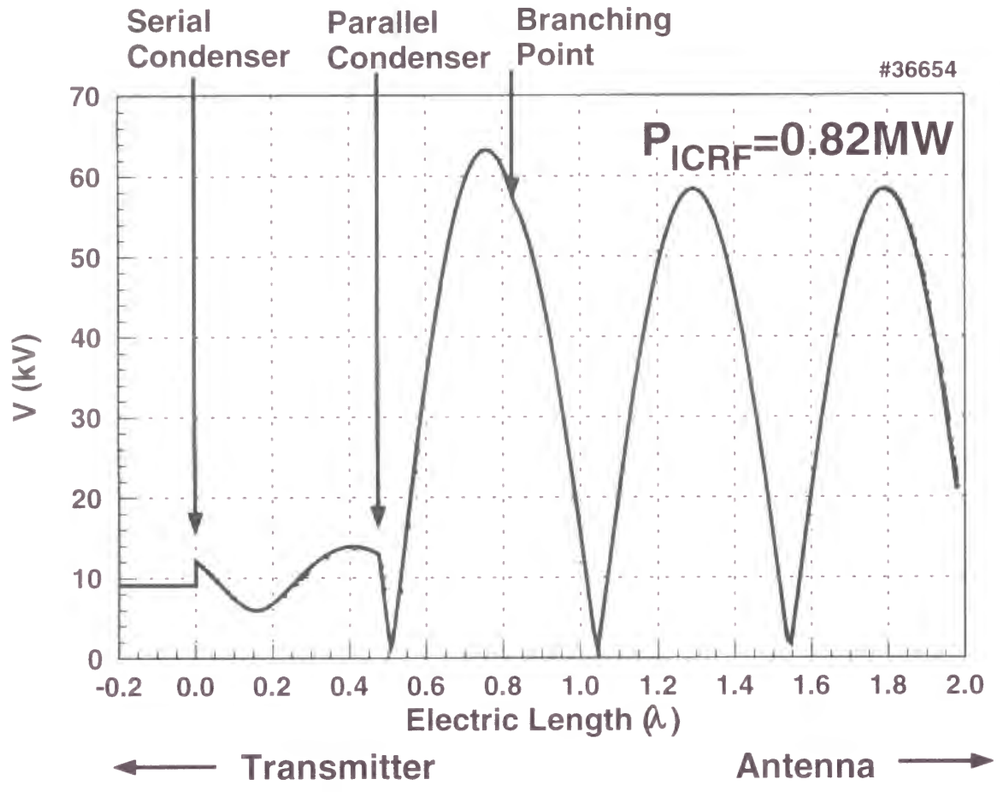

Fig. 2.8. The voltage distribution along the transmission line of system I. The origin of the abscissa is the position of the serial condenser and the distance from the condenser is written in a unit of the wavelength λ of 11.2 m for the frequency 26.7 MHz. The power of RF transmitter is 0.82 MW. The maximum voltage (peak to peak) is 63 kV. The voltage at the feedthrough (at the right-side end in this figure) is 21 kV in this case.

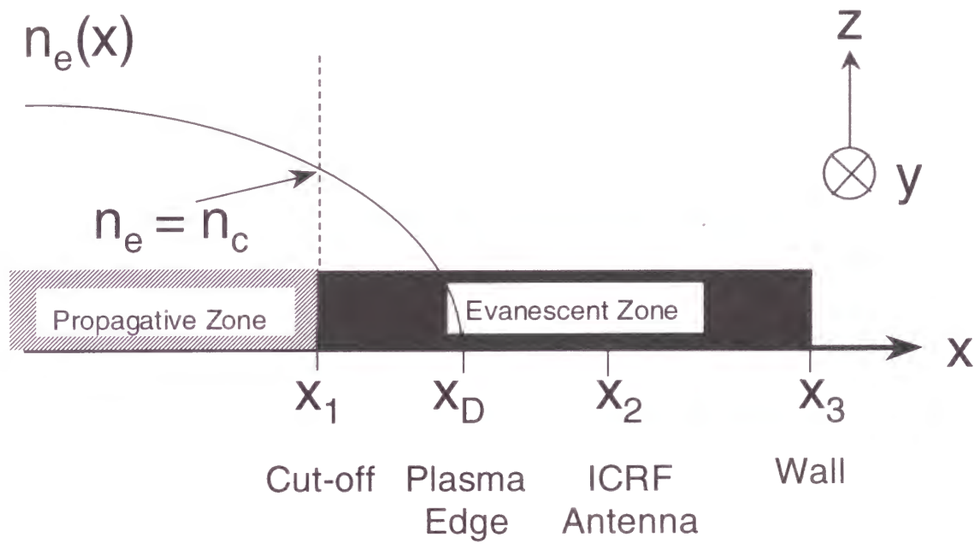

Fig. 2.9. A schematic view of Adam's model for the antenna impedance calculation. The boundary of the propagation zone, x_1, is determined by the equation: $k_x^2 = 0$. The rest parameters are chosen as follows. x_d = 0.2 m (the average plasma minor radius), x_2 = 0.22 m, and x_3 = 0.25 m. The electron density at the center of the magnetic axis is 2.0 $\times$ 10^{19} m^{-3} and the profile is assumed to be parabolic. The magnetic field strength is 1.9 or 1.76 T.

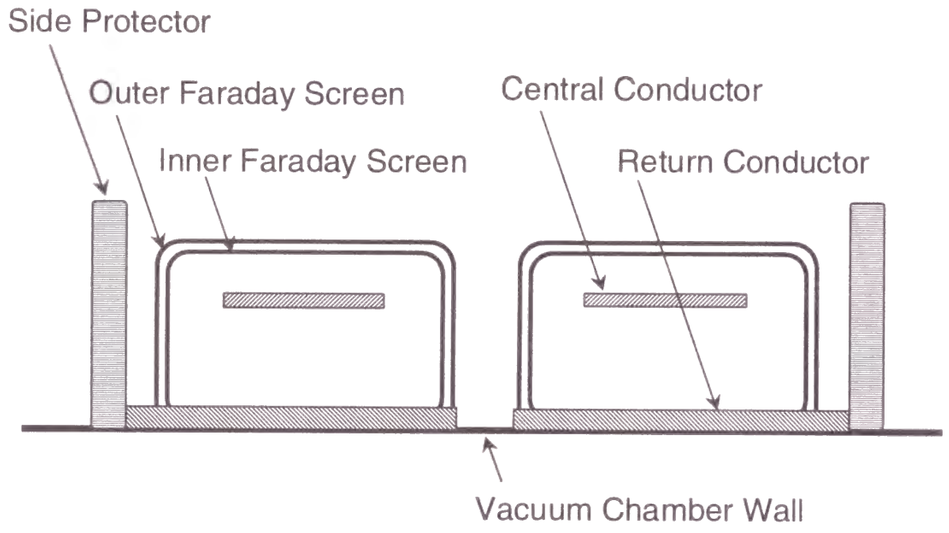

Fig. 2.10. A schematic view of the cross-section of the pair of antennas in Heliotron E. These antennas consist of central conductors, return conductors, double-layer Faraday screen and side protectors.

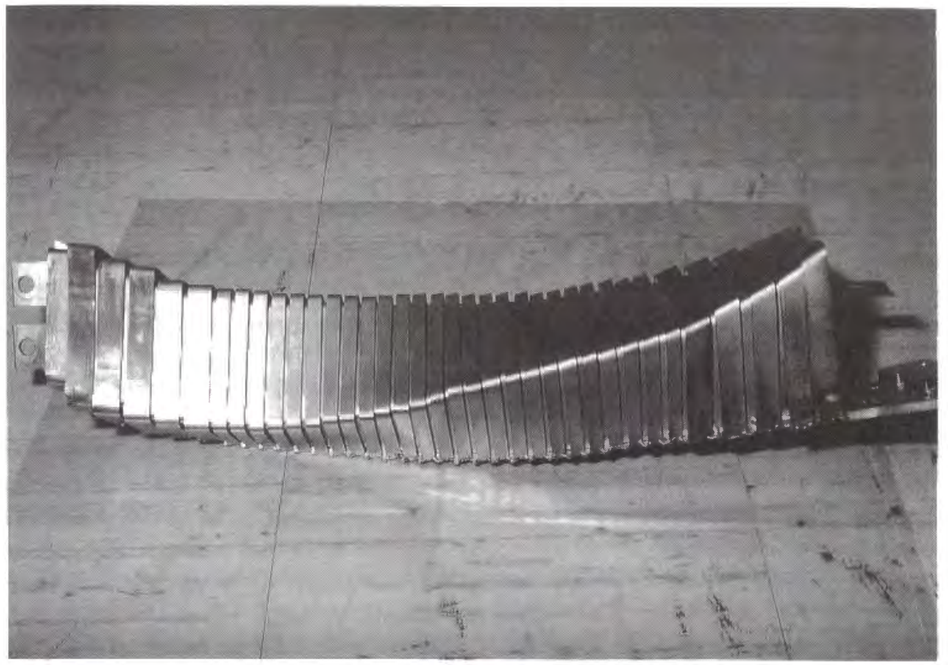

Fig. 2.11. Photograph of one piece of antenna strap. The twisted structure is designed for facing the helically distorted plasma shape.

Chapter 3

Fast Ion Production by ICRF Heating in Hydrogen Minority Plasma

3.1 Introduction

In the Heliotron-E device, the ICRF heating experiment [24, 35, 49] accompanied with the fast ion particle production has been executed with special regard to the first-step simulation of alpha particle confinement. ICRF power up to 1.0 MW was injected into the Heliotron-E plasma. Fast ions up to 100 keV were produced under the low-density conditions. The maximum energy of such fast ions is not limited to the specific value as in NBI heating [75, 76], but it is determined by the balance among the acceleration by the ICRF wave, the relaxation by Coulomb collisions with bulk particles, and the loss mechanisms such as charge exchange losses and orbit losses.

The fast ions would be utilized to heat the bulk plasmas and to enhance the fusion reactions in future experiments [77]. However, the high-energy ions must be confined for a sufficiently long time to establish a high-energy tail and to make nuclear fusion reactions effectively. For three-dimensional helical confinement devices, high-energy ion confinement is a crucial problem, since there can be a loss cone in velocity space for collisionless orbits [78, 79]. In the minority heating using fast wave [80] the minority ions are accelerated first, then the bulk particles are heated through Coulomb collisions with these accelerated ions. For toroidal devices with the loss cone in velocity space, the estimation of the confinement time of the accelerated high-energy ions is important for

the discussion of the heating efficiency especially in the minority-heating scheme. The high-energy tail formation has already been observed in many tokamak minority-heating experiments [81].

In this chapter, the behavior of the fast ions produced by the ICRF minority heating in Heliotron E is described with regard to the production and relaxation of these particles. The high-energy tail in the range from 17 keV to 33 keV was observed to be formed within 1 msec. The higher-energy tail above this range developed within about 10 msec. The flux decay time after the termination of the ICRF pulse was unexpectedly short compared with the values from the classical collision processes.

First of all, wave characteristic in the target plasma will be discussed, then, the arrangement of the experimental equipment in the ICRF heating is briefly described in Sec. 3.2. The standard fast wave heating experiment with minority protons was carried out before studying the details of the fast ion production. In Sec. 3.3, the results of the ICRF experiment in the Heliotron-E device is described. The charge exchange hydrogen fluxes were measured up to 100 keV using the neutral particle analyzer (NPA) and the results are presented in Sec. 3.4. Confinement properties of fast ions are discussed in Sec. 3.5.

3.2 Wave Characteristics in the Target Plasma

Figure 3.1 shows the typical position of the resonance and cutoff layers for the ICRF heating of the Heliotron-E plasma. Most part of the antenna loop is installed on the high field side, however, the antenna loops cross the fundamental cyclotron resonance layer of

the minority proton satisfying $\omega = \omega_{cH}$ at the both ends of the antenna. Photograph of the antenna loops installed inside the Heliotron-E vacuum vessel is shown in Fig. 3.2.

The magnetic field strength and the minority proton ratio given by $n_H/(n_H+n_D)$ are controlled to change the position of the cyclotron resonance, the two-ion hybrid resonance, the right-hand cutoff and the left-hand cutoff layers, where n_H (n_D) is a proton (deuteron) density. It is assumed that the parallel wave length, $k_{//}$, should be equal to one helical pitch length. Since the phase between a pair of the antennas is 0 rad (see Table 2.4), the $k_{//}$ spectrum becomes broad. But the locations of the resonance and the cutoff layers are insensitive for the $k_{//}$ value except the right-hand cutoff layer ($n_{//}^2 = R$). In most of the fast ion production experiments, the wave frequency was 26.7 MHz and the magnetic field strength was 1.76 T. In this case, the cyclotron layer ($\omega = \omega_{cH}$) is located near the magnetic axis. In the case of a minority proton ratio of 0.05, two-ion hybrid resonance layers satisfying $n_{//}^2 = S$ are located on the high field side.

The wave equation [80] for the fast wave under the low-frequency and high-conductivity approximation is written as

$$\begin{pmatrix} R+L-2n_{//}^2 & -i(R-L) \\ i(R-L) & R+L-2n^2 \end{pmatrix} \begin{pmatrix} E_x \\ E_y \end{pmatrix} \approx 0 . \tag{3.1}$$

Here E_x and E_y are defined as RF electric field components in the plane normal to the z direction in the Cartesian coordinates. The magnetic field is assumed to be in the z direction. R, L, S and D are the cold plasma dielectric tensor elements and are given by

$$R = 1 - \sum_j \frac{\omega_{pj}^2}{\omega(\omega + \varepsilon_j \omega_{cj})}, \tag{3.2}$$

$$L = 1 - \sum_j \frac{\omega_{pj}^2}{\omega(\omega - \varepsilon_j \omega_{cj})}, \tag{3.3}$$

$$S = \frac{1}{2}(R+L), \tag{3.4}$$

$$D = \frac{1}{2}(R-L), \tag{3.5}$$

where ω_{pj} and ω_{cj} are the plasma frequency and the cyclotron frequency of the j-th species, respectively. ε_j is the sign of the charge of the j-th species and $n_{//}$ and n are the parallel component of the vector refractive index and the scalar refractive index. Here we also define $n_\perp$ as the perpendicular component of the vector refractive index. In these equations, the y component of the vector refractive index is assumed to be zero. From Eq. (3.1), the dispersion relation is given by

$$n_\perp^2 = \frac{(R - n_{//}^2)(L - n_{//}^2)}{S - n_{//}^2}. \tag{3.6}$$

Cyclotron acceleration of the ions depends principally on the amplitude of the left-hand circularly polarized component of the wave electric field $\vec{E}$ in a plasma. Here we consider the ratio of the left-hand E component E_+ to iE_y is

$$\frac{E_+}{iE_y} = 1 + \frac{D}{S - n_{//}^2}, \tag{3.7}$$

where $E_+ = E_x + iE_y$. Figure 3.3 shows this ratio along the line A-A' in Fig. 3.1. This value becomes infinity at the two-ion hybrid resonance layer ($n_{//}^2 = S$). At this layer, the RF electric field is linearly polarized in the x direction. The field is purely left-hand polarized at the left-hand cutoff layer ($n_{//}^2 = L$), linearly polarized in the y direction at the D = 0 surface, and purely right-hand polarized at the cyclotron resonance layer. These properties

are explained under the cold plasma approximation. In the consideration of (1) the Doppler effect on cyclotron resonance ($\omega - k_{//}v_{//} = \omega_{cH}$) and (2) the hot plasma effect, the cyclotron resonance layer becomes broader than in the case of the cold plasma approximation. The left-hand component is sufficiently large at the cyclotron resonance layer. Therefore, the left-hand polarized component, which contributes to the ion acceleration, plays the major role in the minority heating. At the hybrid resonance layer, the mode conversion from the fast wave to the ion Bernstein wave occurs. The ion Bernstein wave contributes toward the electron heating via Landau damping and transit-time damping. Second harmonic cyclotron damping for deuterons may occur at fundamental cyclotron resonance for protons. These contributions will be considered in Chap. 5.2.

The arrangement of the equipment in the ICRF experiment is shown in Fig. 3.4. Diagnostic systems are also shown here. The electron temperature is measured by Thomson scattering [82] and ECE [83] systems, the ion temperature as well as the high-energy ion tail spectra by a charge exchange neutral particle energy analyzer [62], the impurity line intensity by a VUV monochromator [84], and the electron density by a 2-mm microwave [85] and a far infrared interferometer [86]. With a visible monochromator [87], the H_α and D_α line intensity ratio can be monitored for estimating the minority ratio in the ICRF minority heating experiment.

3.3 Bulk Heating Result in the ICRF Heating

The ICRF experiments were carried out from the following two viewpoints: one is the heating efficiency with reference to the ICRF input power and the other is the production

and the confinement of the fast ions. The minority-heating experiments using fast wave were done in the range of line average density from 1×10^{19} m^{-3} to 3×10^{19} m^{-3}. Here the proton cyclotron resonance layers were located on the weak magnetic field side and two-ion hybrid resonance layers were at the center of the plasma under the conditions where the RF frequency, f, was 26.7 MHz and the toroidal magnetic field strength at the magnetic axis, $B_{\phi 0}$, was 1.9 T. A target plasma was produced and sustained by 53 GHz ECH with the power of 0.32 - 0.48 MW. The electron cyclotron resonance was also located at the center of the plasma at $B_{\phi 0}$ = 1.9 T. A high ion temperature of 1.0 keV (the increment of the ion temperature was 0.8 keV) was achieved by conditioning the antennas and the chamber wall. Key issues of this conditioning were (1) degassing and (2) recycling control. The surfaces of the antennas were degassed by a number of successive discharges with high power ICRF pulses. Recycling control was achieved with the titanium flushing toward the wall. The proton ratio of the plasma was chosen at around 0.05, which was an optimal value for the ion heating. This ratio increased gradually during the discharge pulse. The typical time evolutions of the plasma parameters are shown in Fig. 3.5(a). ICRF power was turned on at 328 msec and ramped up to 0.96 MW at 350 msec. The ion temperature of the majority deuterons was increased from 300 eV to 600 eV gradually. Radiation power and oxygen impurity line intensity also gradually increased during the ICRF pulse. In this case, the plasma density was sustained only by the wall recycling without gas puffing.

In this parameter regime, the plasma was heated by the ICRF power through the minority-heating scheme. Throughout the ICRF fast wave experiments, the high-energy tail of minority ions was usually observed by NPA under the lower-density conditions. In

the minority-heating scheme, the RF power is absorbed mainly by the minority ions via cyclotron damping. The physical picture of cyclotron damping will be described in Sec. 4.2. A high-energy ion tail was observed to be formed just after the RF pulse was turned on and then the majority ions and electrons were heated by Coulomb collisions with fast minority ions. As shown in Fig. 3.5(a), the ICRF minority-heating scheme worked well. It is also noted that the electron temperature was increased with the ICRF heating. The results of the bulk heating with respect to the input power are summarized in Fig. 3.5(b). The hydrogen minority results are shown here. The increment of the ion temperature in the hydrogen minority case saturated at about 0.5 MW. This saturation might be related to the orbit loss through the velocity space loss cone. However, in the ^{3}He-minority case as mentioned later it continued to increase until the power range of 1 MW. The difference of the bulk heating efficiency between the two cases will be discussed in Chap. 6.

3.4 Production of Fast Ions by ICRF Waves

To investigate the behavior of the high-energy ions, the neutral fluxes for the ICRF heated plasma with relatively low electron density were intensively measured by NPA. The maximum detectable energy of NPA was 100 keV. The proton minority tail temperature, which was defined as the derivative of the logarithm of the velocity distribution f(v) with respect to $(1/2)mv^2$ in the range of 20 keV to 60 keV, was estimated to clarify the tail formation condition with respect to the input power and the electron density. Figure 3.6 shows the tail temperature as functions of the line average electron density and the RF power. Here the highest tail temperature is almost 100 keV. The tail temperature increased with the ICRF input power in the low power region of $\leq$ 1 MW.

However, the tail temperature was not increased monotonically in the higher-power region due to the degradation of the plasma by the increased radiation loss. The high-energy tail could be produced below 2.0×10^{19} m^{-3}.

The typical time evolutions of the charge exchange neutral fluxes from 17.2 keV to 80.3 keV are shown in Fig. 3.7 for $B_{\phi 0} = 1.76$ T. For the fast ion production experiment, it is preferable that the ion cyclotron resonance layer is located at the center of the plasma. For the bulk heating experiments, the two-ion hybrid resonance layer is located at the center in the case of $B_{\phi 0} = 1.9$ T, since electron heating is also expected via mode conversion at the two-ion hybrid resonance layer [80]. Here the line average electron density was 0.7×10^{19} m^{-3} and the input power was 0.82 MW. The particle fluxes in the energy range below 33.0 keV increased with the ICRF input power and saturated at 348 msec when the radiated ICRF power also saturated. However, the higher-energy particle fluxes above 39.3 keV continued to increase during the RF pulse. The high-energy tail formation was seen more clearly in the case of the higher RF power and the lower plasma density at the fixed minority ion ratio. Also the smaller minority ion ratio was effective for the fast ion production. The measured velocity distributions of the minority proton for the various power levels are shown in Fig. 3.8(a). The plasma density and the electron temperature were almost constant as shown in Fig. 3.5(a). The ICRF power was changed from 0.12 MW to 0.82 MW. The bulk deuteron temperatures during ICRF pulse were in the range of 400 eV to 800 eV. As the power was increased, the tail temperature increased from 14 keV to 45 keV. The detectable highest energy was limited by the setting of NPA. These results presented the evidence of the high-energy ion production during the ICRF minority heating in the heliotron configuration.

The observed velocity distributions were compared with the theoretical prediction given by a point model without the direct orbit loss. The distributions calculated with Stix's expression [86] are shown in Fig. 3.8(b). The expression of the velocity distribution function f(v) is given by

$$\ln f(v) = -\frac{E}{T_e(1+\xi)}\left[1+\frac{R_j(T_e - T_j + \xi T_e)}{T_j(1+R_j+\xi)}H\left(\frac{E}{E_j}\right)\right], \tag{3.8}$$

where $E = mv^2/2$, $R_j = n_j Z_j^2 a_j / n_e a_e$, $a_j = (m_j / 2T_j)^{1/2}$,

$$H(x) = \frac{1}{x}\int_0^x \frac{du}{1+u^{3/2}},$$

$$\xi = \frac{m < P >}{8\pi^{1/2} n_e n Z^2 e^4 \Lambda}\left(\frac{2T_e}{m_e}\right)^{1/2} \text{ and } E_j = \frac{mT_j}{m_j}\left[\frac{1+R_j+\xi}{2\varepsilon(1+\xi)}\right]^{2/3}$$

Here m is the mass, n is the density, T is the temperature, Z is the ionic charge, and $\varepsilon = 2/3\pi^{1/2}$. The parameters with suffix j (e) denote those of the background ion (electron) and the parameters without suffix denote those of the minority ion. Λ is the Coulomb logarithm [89]. <P> is the wave-heating power per unit volume delivered to the minority ions, averaged over a magnetic surface. The ξ parameter (the ratio of the quasi-linear diffusion term to the Coulomb collision terms in the Fokker-Planck equation) in this model was estimated with experimental plasma parameters. This distribution function provides an ideal production of the high-energy tail. The ξ parameters are 242, 110 and 52, which correspond to the input powers 0.82 MW, 0.23 MW and 0.12 MW, respectively. The experimental velocity distributions in Fig. 3.8(a) show that the tail temperatures were lower than those in Fig. 3.8(b). It should be noted that we assumed the uniform absorption of the ICRF wave for Stix's expression. Orbit and transport losses and

the profile effects are not included in this model. For a more accurate analysis of the experimental data, a more realistic model including the orbit following calculation is required. The improved model will be discussed in the next chapter.

3.5 Confinement of Fast Ions

In order to investigate the confinement of the fast ions experimentally, the decay times of the measured high-energy fluxes in Fig. 3.7, were determined as shown in Fig. 3.9. The decay time is defined as the 1/e fall time after the ICRF pulse is terminated. The decay times became shorter in the higher-energy region at the various input powers. The errors of the measurement of the decay time were within 1 msec, since the sampling rate was 1 msec in these experiments. The decay time in the higher-energy range could not be measured due to its shortness. The slowing down time τ_{sl}, the pitch-angle scattering time τ_d, the energy exchange time τ_E and the charge exchange time τ_{cx} calculated with the experimental plasma parameters are shown in Fig. 3.10. τ_{sl} is given by [90]

$$\tau_{sl} = \frac{\tau_s}{3}\log\left[1+\left(\frac{E}{E_{crit}}\right)^{3/2}\right], \tag{3.9}$$

$$\tau_s = \frac{(2\pi)^{1/2} 6\pi\varepsilon_0^2 m_i m_e^{-1/2} T_e^{3/2}}{Z^2 n_e e^4 \Lambda}, \tag{3.10}$$

$$E_{crit} = \left(\frac{9\pi m_p}{16 m_e}\right)^{\frac{1}{3}}\left(\frac{1}{n_e}\sum_i \frac{n_i Z_i^2}{A_i}\right)^{\frac{2}{3}} T_e A, \tag{3.11}$$

where E is the energy of fast ion, ε_0 is the permittivity in vacuum, e is the electronic charge, m_i and m_e are the masses of the bulk ion and the electron, T_e and n_e are the electron temperature and density, Z and A are the ionic charge and the atomic mass of the fast ion,

m_p is the proton mass, ni, Z_i and A_i are the density, the ionic charge and the atomic mass of the i-th bulk ions, respectively. The summation in Eq. (3.11) is taken for the bulk ion species. $\tau_d = 1/\nu_d$, $\tau_E = 1/\nu_E$, where ν_d and ν_E are given in Chap. 4. τ_{cx} is given by [91]

$$\tau_{cx} = \frac{1}{n_0 \sigma_{CX} v_{rel}}, \tag{3.12}$$

$$\sigma_{CX} = \frac{6.937\times10^{-19}(1.0-0.155\log_{10} b)^2}{1.0+1.12\times10^{-15} b^{3.3}}, \tag{3.13}$$

$$b = \left(\frac{E}{e} + \frac{4.0T_i}{\pi e}\right), \tag{3.14}$$

$$v_{rel} = \left(\frac{2.0eb}{Am_p}\right)^{1/2}, \tag{3.15}$$

where T_i is the bulk ion temperature. Here the neutral density n_0 was assumed to be 1.0 $\times10^{15}$ m^{-3} for evaluating τ_{cx}. This value was estimated from the empirical scaling law deduced from the laser induced fluorescence technique [92]. The total reaction time, , is defines by,

$$\frac{1}{\tau_{total}} = \frac{1}{\tau_{sl}} + \frac{1}{\tau_d} + \frac{1}{\tau_E} + \frac{1}{\tau_{cx}}. \tag{3.16}$$

All characteristic times shown in Fig. 3.10 are longer than the experimental decay time. It is noted that the decay time of the lower energy fluxes is longer probably owing to the fact that the slowing down ions from the upper energy regime play the role of a source term in the generation of the lower energy ions. Therefore, the experimental tendency that the decay time is longer in the lower energy regime seems to be reasonable. But the absolute value was much shorter than that based on the classical collision theory. The predictions in Fig. 3.10 were deduced without consideration of the collisionless orbit losses. The

effects of the orbit losses on the confinement of the fast ions in the helical confinement devices can be serious [59, 60]. It is considered that the discrepancy between the results of Fig. 3.9 and Fig. 3.10 is attributed to the orbit losses of the tail ions. The relevant analysis and simulation are given in the following chapters.

3.6 Summary

ICRF heating experiments have been carried out successfully in the Heliotron-E device. In the medium density regime, the substantial increment of the ion and electron temperatures was observed (see Fig. 3.5(a)). The achieved ion temperatures were 0.6 keV for the hydrogen minority and 1.0 keV for the ^{3}He minority in the density range from 1.5 $\times10^{19}$ m^{-3} to 2.5$\times10^{19}$ m^{-3}. The radiation loss was small in the case that the input power was less than 1.0 MW. The obtained ion temperature about 1 keV is the highest in the ICRF experiments among the middle-size heliotron/trosatron devices in the world.

In the minority-heating scheme, it was confirmed that the fast ions are produced substantially as expected from the scenario that RF power is mainly absorbed by the minority species of ions. The confinement of the fast ions up to 100 keV by ICRF minority heating in heliotron/torsatron was firstly investigated experimentally in Heliotron E. The high-energy tail in the range from 17 keV to 33 keV was observed to be formed within 1 msec. However, the decay time of the minority ion fluxes after the termination of the ICRF pulse was unexpectedly short compared with the characteristic times of the various collisional processes such as slowing down, charge exchange and so on. It was about one fifth of the characteristic time determined by the total collisional

processes without orbit loss. A guess was that the orbit loss is not negligible for the energy loss of the high-energy ions.

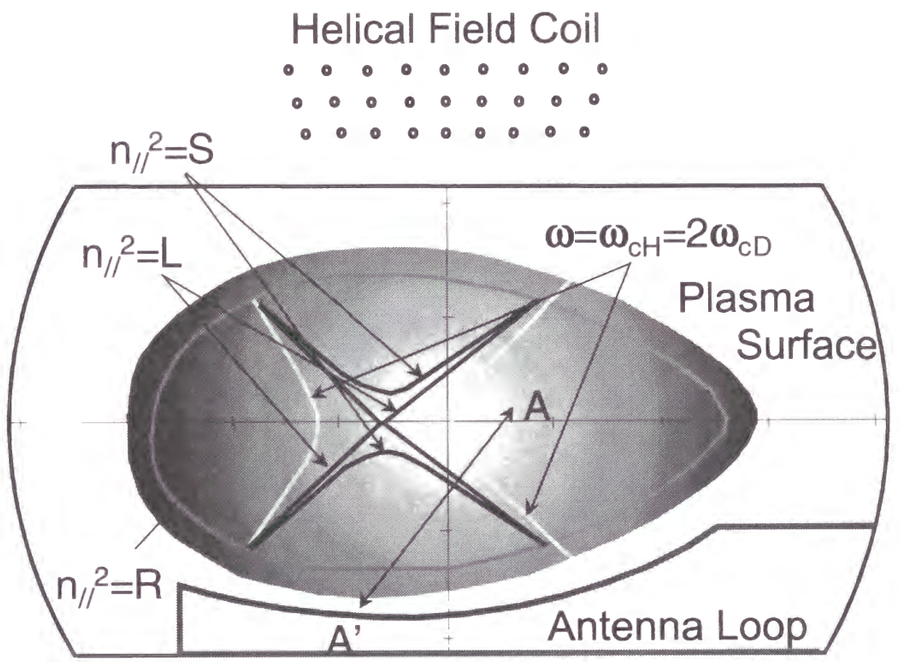

Fig. 3.1. A schematic view of the plasma cross-section for ICRF heating. The cyclotron resonance($\omega = \omega_{cH}$), the two-ion hybrid resonance ($n_{//}^2 = S$), the right-hand cutoff ($n_{//}^2 = R$), and the left-hand cutoff ($n_{//}^2 = L$) layers are shown for the parameters: $B_{\phi 0}$ = 1.76 T, $n_e(0) = 2.0\times10^{19}$ m^{-3}, the frequency f = 26.7 MHz and the minority proton ratio $n_H/(n_H+n_D) = 0.05$, where $n_{//} = k_{//}c/\omega$, $k_{//}$ is the parallel wave number and n_H (n_D) is the proton (deuteron) density. Antenna loops were installed on the high field side. Helical coils are located at the top and bottom in this cross-section. A - A' line presented here is for the explanation of the wave characteristic in Fig. 3.3.

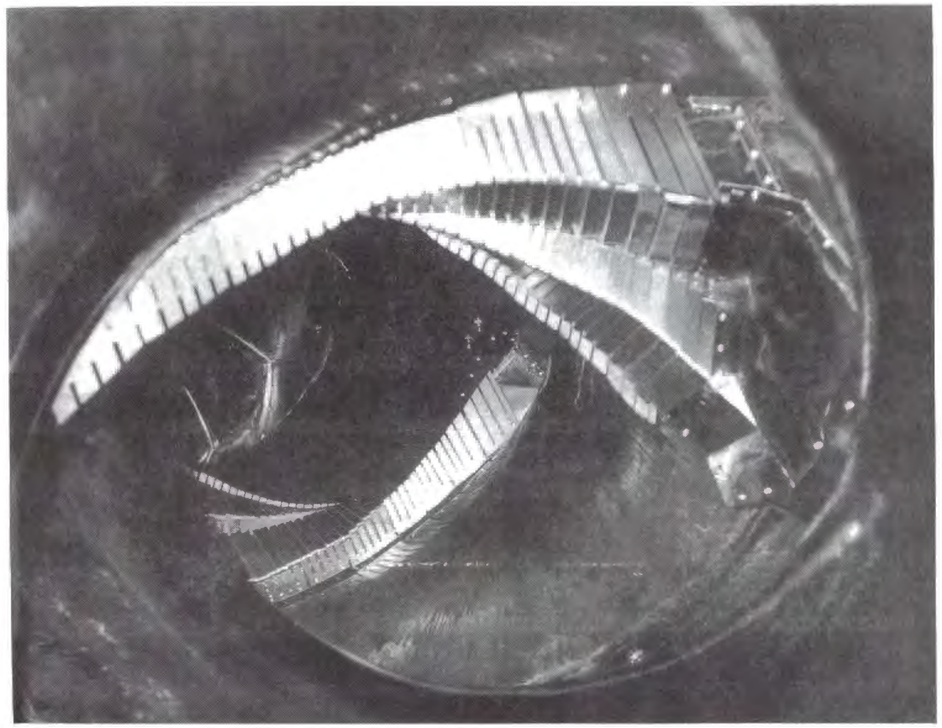

Fig. 3.2. Photograph of the antenna loops installed inside the Heliotron-E vacuum vessel.

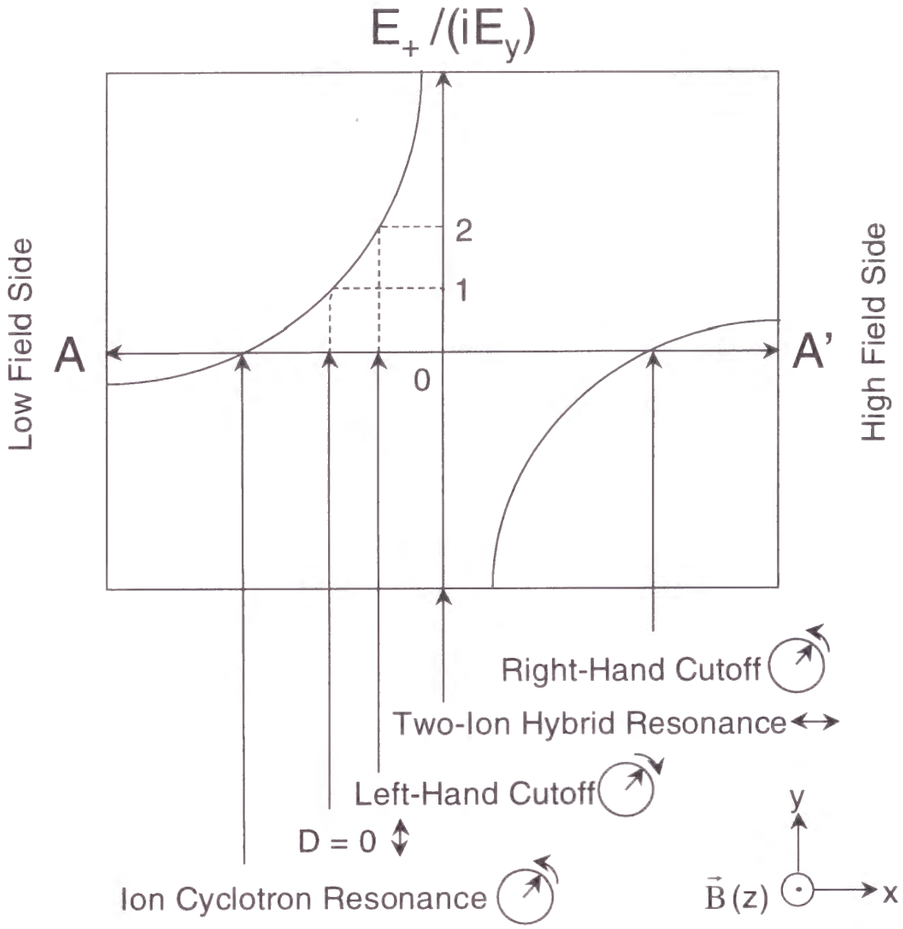

Fig. 3.3. The ratio of the left-hand RF electric field component E_+ to iE_y. The magnetic field direction is upward to the sheet. The abscissa corresponds to the line A - A' in Fig. 3.1. The polarization is purely right-handed at the right-hand cutoff and the cyclotron resonance layers. The RF field is purely left-hand polarized at the left-hand cutoff layer. At the hybrid resonance and D = 0 layers, the field is linearly polarized.

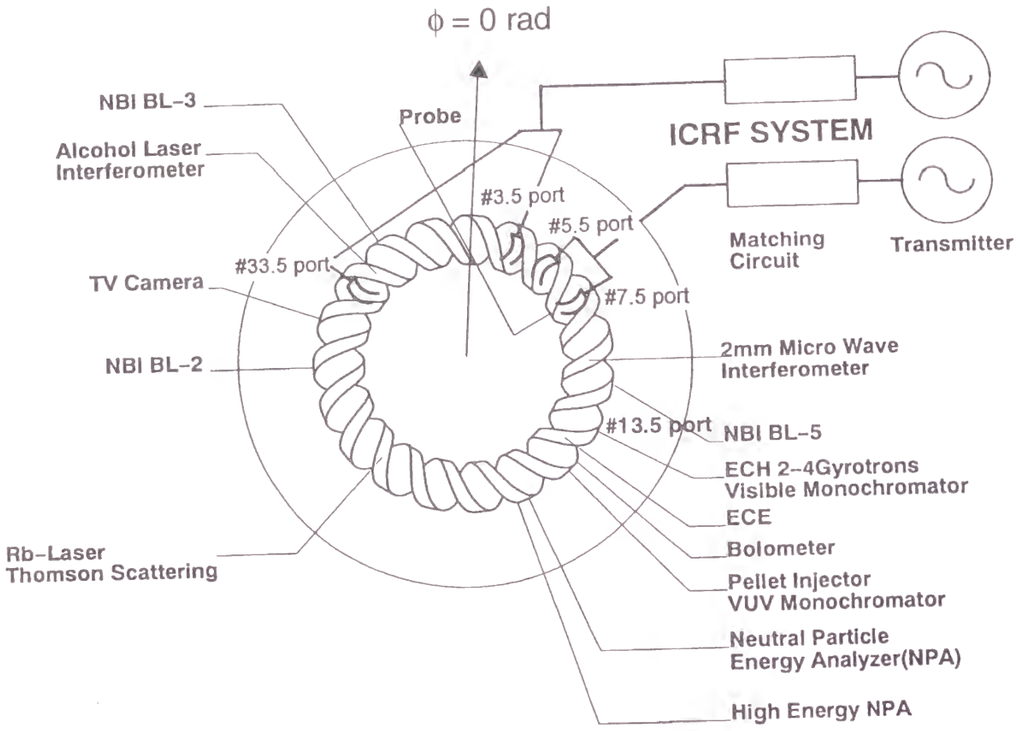

Fig. 3.4. The arrangement of the equipment in the ICRF experiment. ICRF power was introduced to the eight antenna loops inside the vacuum chamber from the two transmitters. A pair of antenna loops was installed on the upper wall or lower wall in the poloidal plane as shown in Fig. 3.1 and the phase between them was 0 rad.

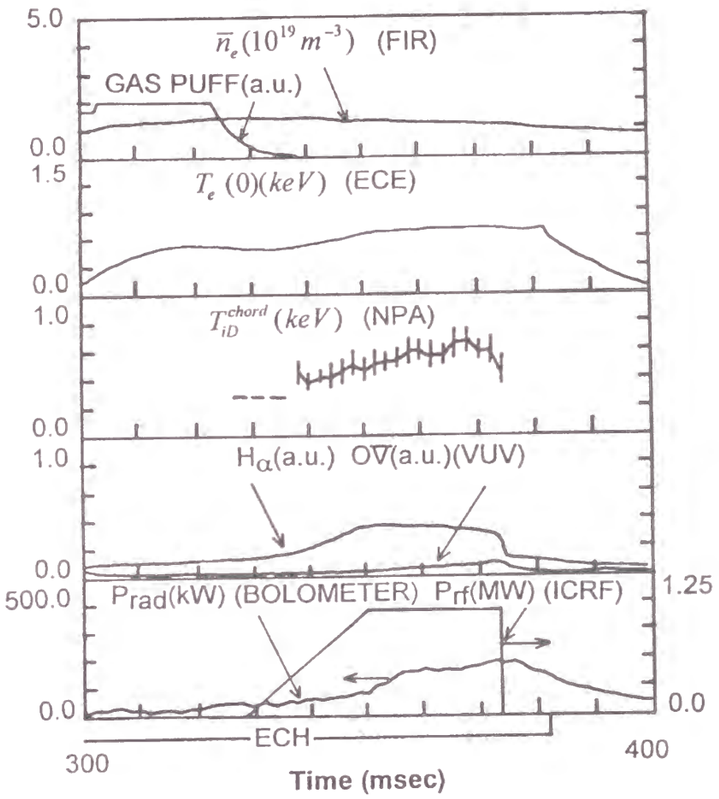

Fig. 3.5(a). Time evolutions of plasma parameters. In this case, $B_{\phi 0}$ = 1.9 T, $n_e(0) = 1.6 \times 10^{19}$ m^{-3} and ICRF power was 0.96 MW for 350 - 373 msec. The ICRF pulse was started at t = 328 msec. The ion temperature, T_i, measured from the deuterium fluxes gradually increased during the ICRF pulse. The H_α line intensity increased and saturated at t = 350 msec. The OV line intensity also increased gradually until the end of the ICRF pulse.

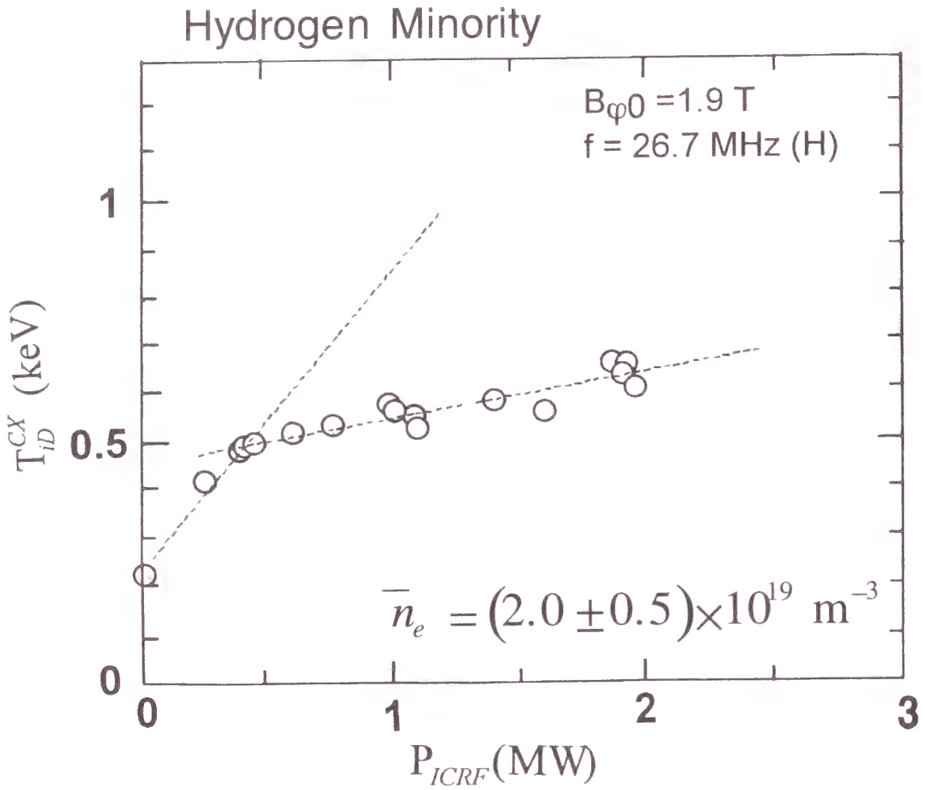

Fig. 3.5(b). Ion temperature of bulk deuterons measured by the neutral particle energy analyzer as a function of the transmitter power P_{ICRF}. The radiated RF power from the antenna is estimated to be $(0.6 - 0.7) \times P_{ICRF}$.

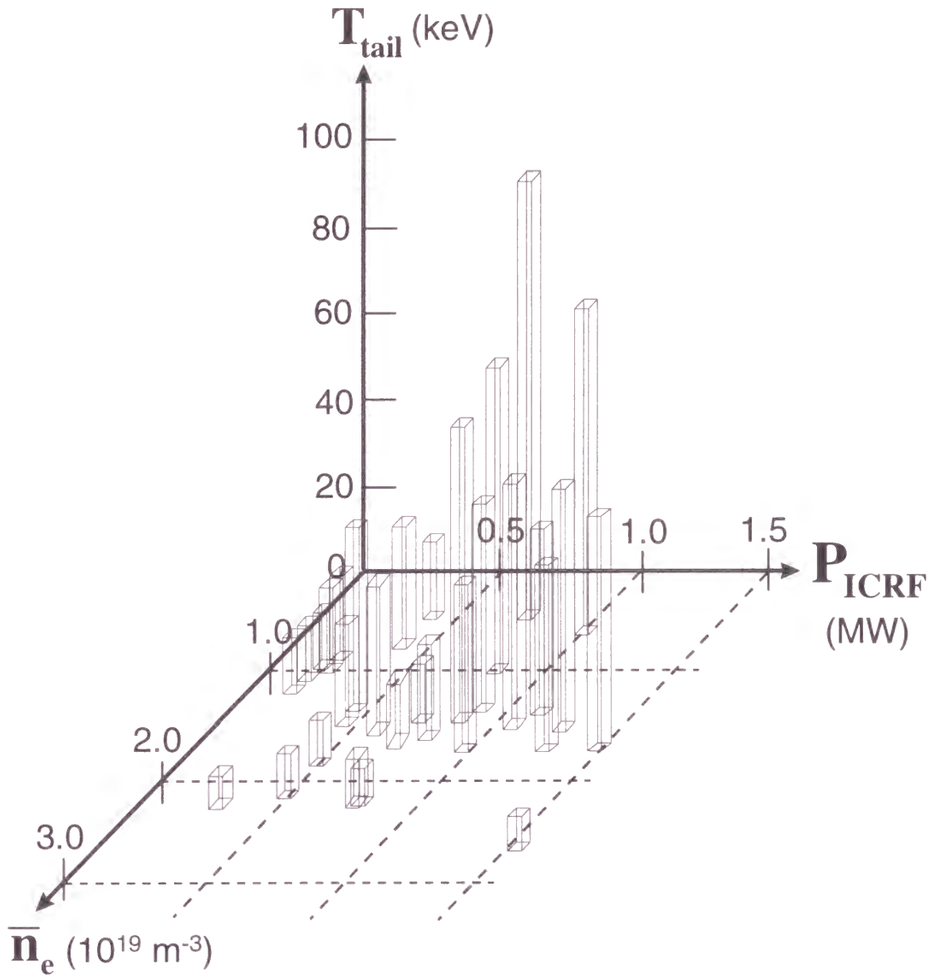

Fig. 3.6. Tail temperature as functions of the line average electron density and the RF power.

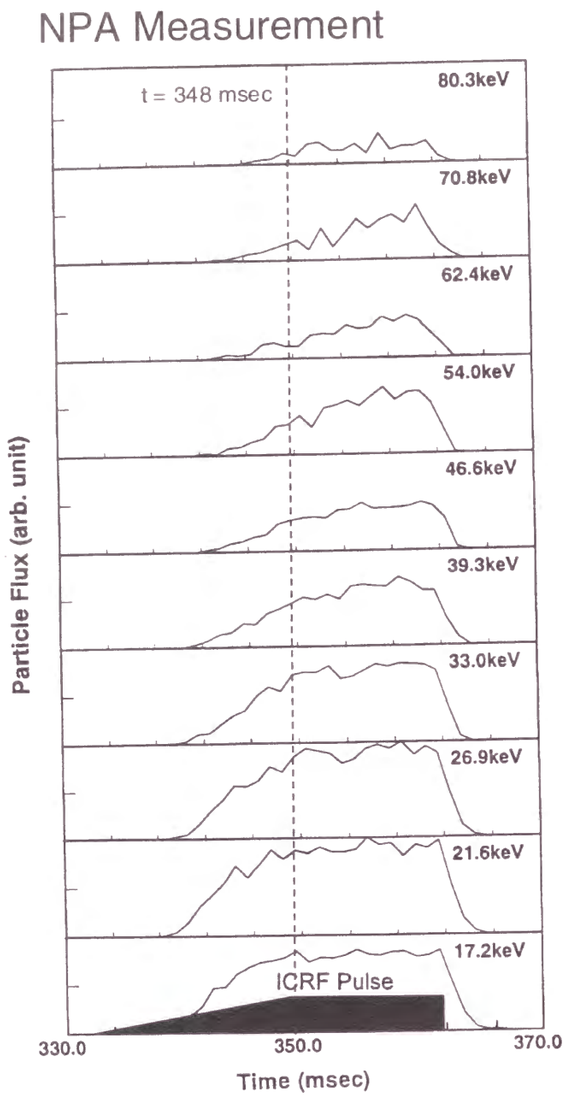

Fig. 3.7. Minority hydrogen fluxes measured by NPA. The ICRF pulse was applied from t = 335 to 378 msec. In the low energy range (< 30 keV) the fluxes increased with ICRF power and saturated when the ICRF power became constant. The high-energy (> 39 keV) fluxes still increased gradually. $\bar{n}_e = 0.7 \times 10^{19}$ m^{-3}, $B_{\phi 0} = 1.76$ T, and $P_{ICRF} = 0.82$ MW.

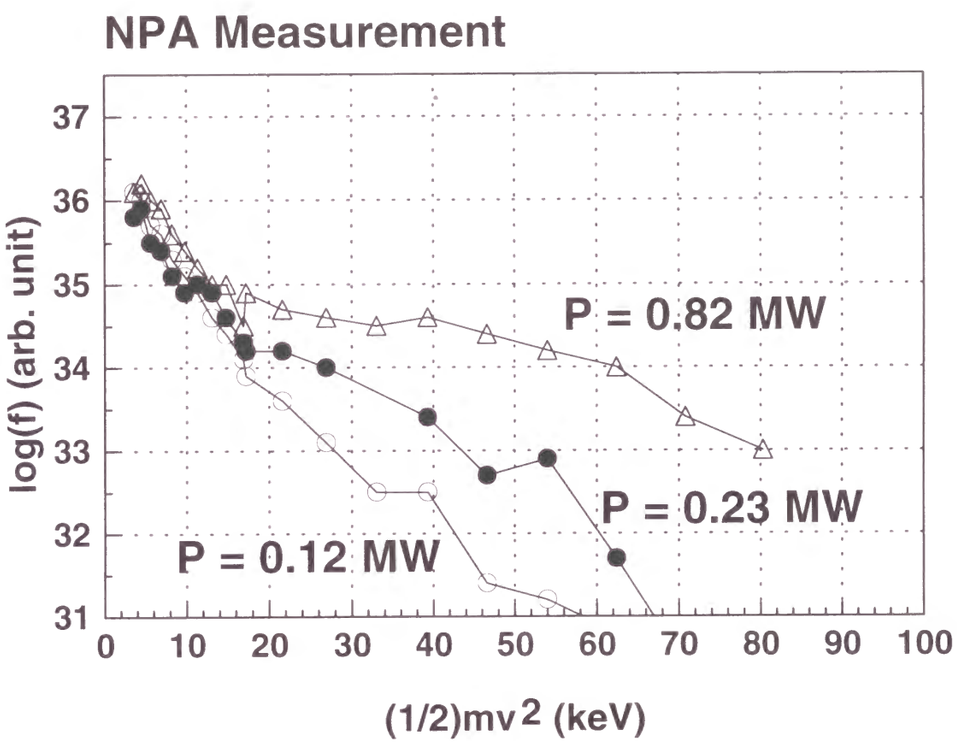

Fig. 3.8(a). The velocity distribution of the minority ions measured by NPA for RF powers of 0.12 MW, 0.23 MW, and 0.82 MW. The tail temperature increased with the RF power. Here $\bar{n}_e = 0.7 \times 10^{19}$ m^{-3}, $B_{\phi 0} = 1.76$ T, and f = 26.7 MHz. The tail temperatures of protons were 14 keV (0.12 MW), 22 keV (0.23 MW), and 45 keV (0.82 MW). The bulk temperatures of deuterons measured by the other NPA were 400 eV (0.12 MW), 750 eV (0.23 MW) and 800 eV (0.82 MW).

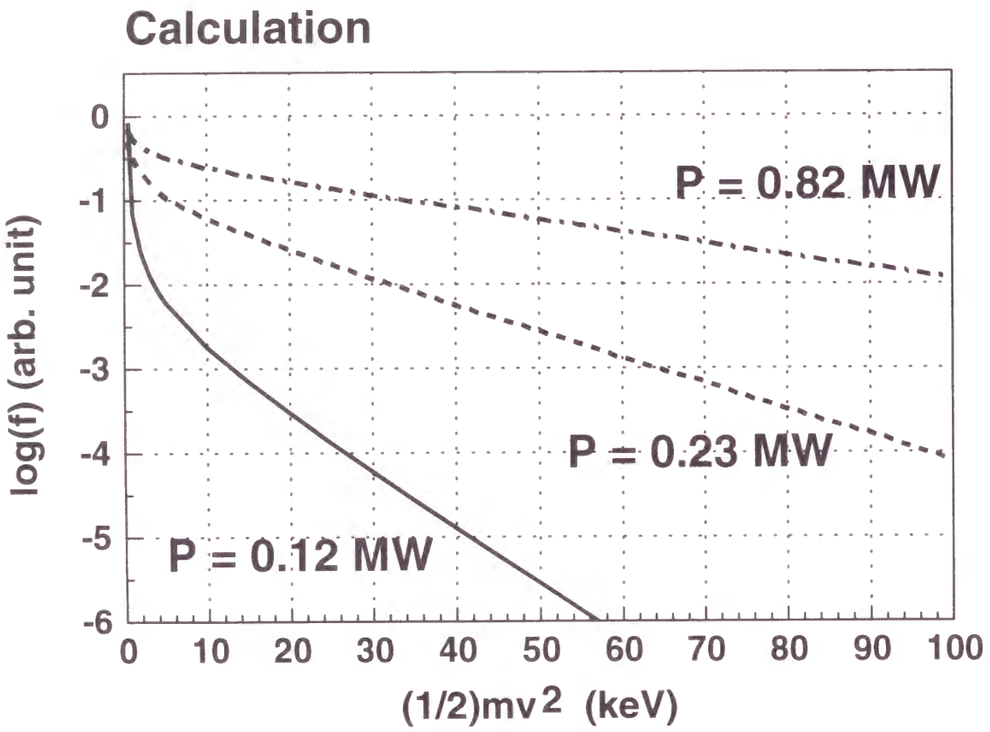

Fig. 3.8(b). High-energy tail formation calculated from Stix's expression using the experimental plasma parameters: $\bar{n}_e = 0.7 \times 10^{19}$ m^{-3}, $T_e = 300$ eV, $B_{\phi 0} = 1.76$ T, and the minority proton ratio $n_H/(n_H+n_D)$ of 0.05, where n_H (n_D) is the proton (deuteron) density. The calculated tail temperatures were 16 keV (0.12 MW), 32 keV (0.23 MW), and 70 keV (0.82 MW).

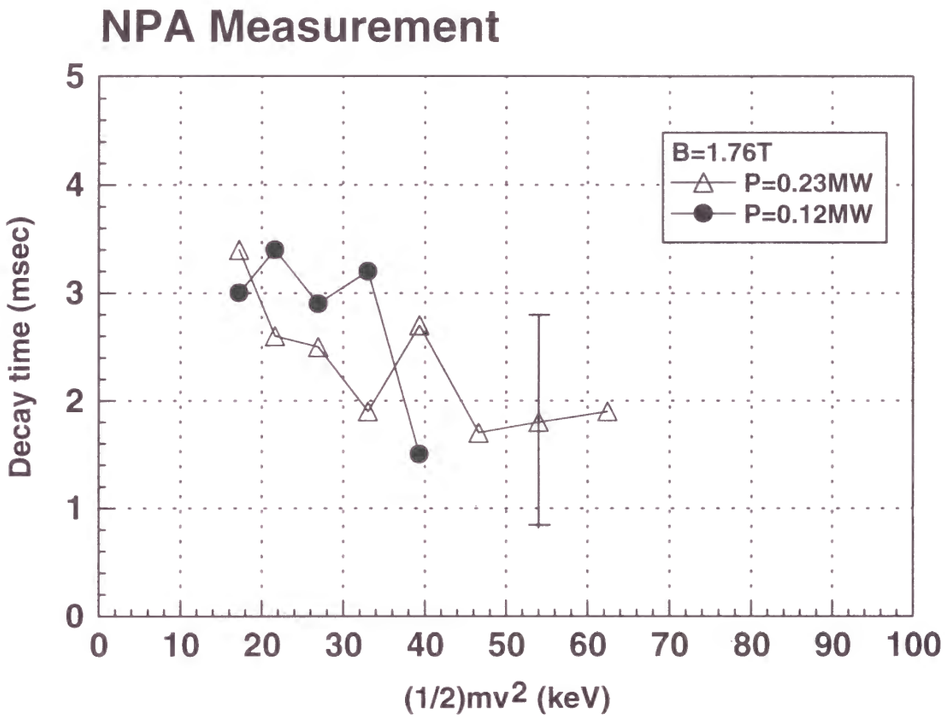

Fig. 3.9. Decay times of the measured high-energy ion fluxes in Fig. 3.7. The decay time decreased with the increase of the ion energy.

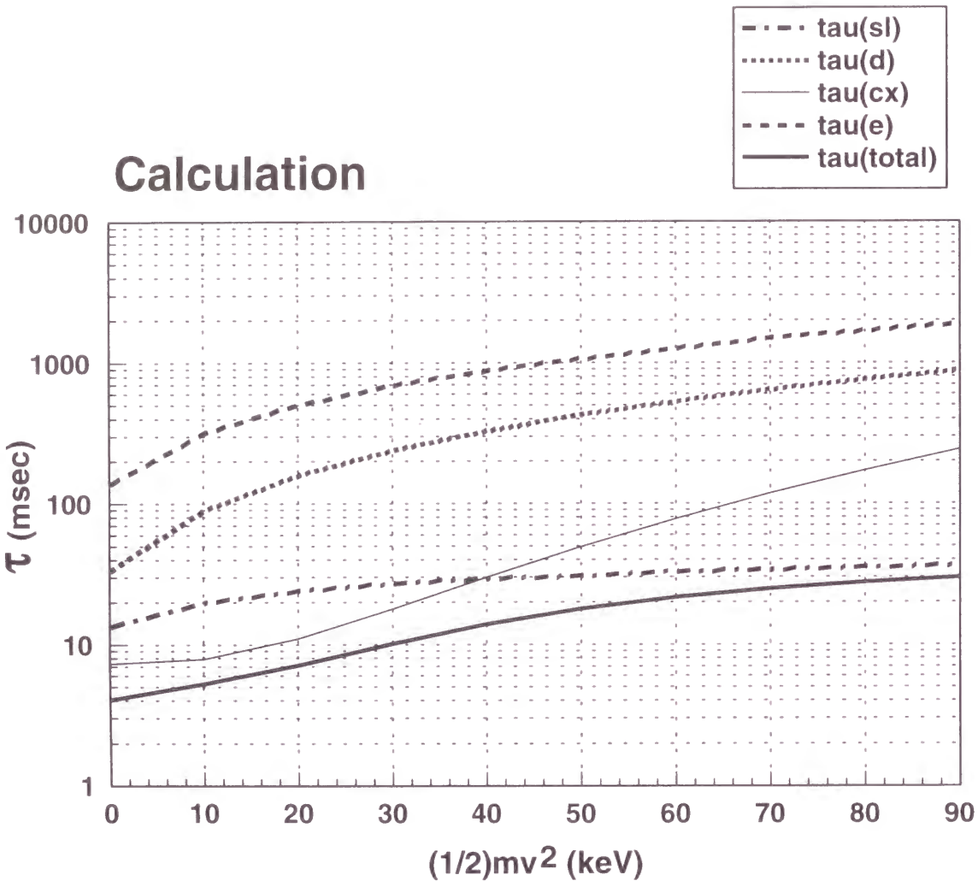

Fig. 3.10. Characteristic times for reactions with the high-energy minority ions: the broken line, the dotted line, the thin solid line, and the dash-dotted line denote the energy exchange time (τ_E), the pitch-angle scattering time (τ_d), the charge exchange time (τ_{cx}), and the slowing down time (τ_{sl}), respectively. The thick solid line represents the total reaction time.

Chapter 4

Numerical Code for Analyzing the Behavior of Fast Ions in ICRF Heating Plasma

4.1 Introduction

A Monte Carlo code has been developed to analyze the behavior of the accelerated ions by the ICRF waves. The estimation of the orbit loss energy is necessary for evaluating the efficiency of the ICRF minority heating. The wave energy in the minority-heating scheme is first absorbed mainly by the minority ions and then the accelerated minority ions transfer their energy to the bulk particles via collisional processes. If the confinement time of the accelerated ions is not sufficiently long, the heating efficiency could be degraded. The acceleration processes and collisional processes should be included in the code self-consistently.

The velocity of the accelerated ion is changed randomly due to collisions, which affect the drift orbit. For example, pitch-angle scattering changes the particle motion from the trapped orbit to the transit orbit and vice versa. There are a number of methods for modelling these phenomena. In the present investigation, Boozer's model [93] for the orbit calculation and the collision operators [93, 94] are used. For modelling the wave heating, the particle acceleration term by the ICRF heating [88] is added to the model.

In this code [54, 95], the initial values are given as the input parameters, among which the velocity distribution is assumed to be Maxwellian to represent the ion temperature. The initial locations of the particles are given uniformly in the toroidal and poloidal

directions, and in the radial direction they are given in consistency with the radial density profile. The total number of ions should be large enough to simulate the behavior of the minority ions as a whole. During the orbit following of the minority ions, these ions experience the acceleration or deceleration by the ICRF wave and the collisions with bulk ions and electrons. Some of them can escape from the confinement region, when they enter the loss cone in velocity space. These ions contribute to the orbit-loss term in the energy balance equation, since they brought their energy to the wall.

There are a number of works for the orbit following calculations in tokamaks and stellarators [94, 96]. The neutral fluxes measured by NPA were studied using Monte Calro methods in Ref. [96], where the up-down asymmetry of the fluxes was investigated for NBI plasmas. However, the detailed simulation study of the fast ions accelerated by the ICRF wave under the existence of the loss cone has not been performed in spite of the importance of the comparison between the prediction and the measurement with regard to the tail formation.

All program modules were carefully checked by the comparison with the analytic results, then incorporated for use in the estimation of the heating efficiency and the emitting flux decay time of the fast ions. Numerical results will be presented in Chap. 5.

4.2 Modelling

4.2.1 Guiding Center Drift Equations

Toroidal plasmas can be confined with the nested toroidal magnetic surfaces. If the magnetic field line is followed long enough, (1) it will either close upon itself, (2) continue to cover a toroidal surface, or (3) continue to construct a toroidal ring when it

stays in a finite region. Other possibility is that the magnetic field line goes to infinity. The magnetic surface is defined as the toroidal surface of (2). Since charged particles move quickly along the field line, plasma parameters such as temperature and density become constant on the magnetic surface. Therefore, it is useful to define a radial coordinate with the magnetic flux enclosed by a magnetic surface when physical phenomena depend on plasma parameters as a function of the magnetic surface. Such coordinate systems are called 'magnetic coordinates'.

It is noted that there are several choices for choosing two angle variables. Since $\vec{B}$ is divergence-free, it can be represented by the Clebsch representation

$$\vec{B} = \vec{\nabla}\alpha \times \vec{\nabla}\psi \,, \tag{4.1}$$

where α and ψ are the functions of position and ψ (=const.) labels the magnetic surface. The other representation of the magnetic field is

$$\vec{B} = \vec{\nabla}\chi + \beta\vec{\nabla}\psi + \gamma\vec{\nabla}\alpha \,, \tag{4.2}$$

where χ is also the function of position. The coordinate α is an angle within a magnetic surface labeling the various field lines and χ is the coordinate along the field line. β and γ are arbitrary functions which represent non rotation-free part of the magnetic field. By making a scalar product of Eq. (4.1) and Eq. (4.2), the relation for the three scalar functions (α, ψ, χ) is given as

$$\vec{\nabla}\chi \cdot \left(\vec{\nabla}\alpha \times \vec{\nabla}\psi\right) = B^2 \,. \tag{4.3}$$

The left-hand side of the above equation is equal to the inverse of the Jacobian of the coordinate system (α, ψ, χ).

The guiding center drift equations describe the drift motion of charged particle in the magnetic field. Charged particles moving in the magnetic field are governed by the Lorentz force and the trajectories are spiral along the magnetic field line. The center of this spiral line is called 'guiding center' [97] (see Fig. 4.1). The trajectory of the guiding center is usually treated as the particle trajectory because the difference between these trajectories is small under the condition of the strong magnetic field. The drift velocity $\vec{v}_\perp$ across the nested magnetic surfaces is given as follows [97, 98]:

$$\vec{v}_\perp = \frac{\vec{B}}{qB^2} \times \left(\mu \vec{\nabla} B + q \vec{\nabla} \Phi + m v_{//}^2 \hat{b} \cdot \vec{\nabla} \hat{b} \right), \tag{4.4}$$

where $\hat{b} = \vec{B} / B$ is the unit vector along the magnetic field line, Φ is the electric potential, μ is the magnetic moment, $\vec{v}_{//}$ is the velocity of the particle along the magnetic field line, and q is the charge of particle.

The guiding center drift equations [93] are expressed using magnetic coordinates, α, ψ, and χ, as follows:

$$\frac{d\alpha}{dt} = v_{//} B \left(\frac{\partial \rho_{//}}{\partial \psi} - \frac{\partial (\beta \rho_{//})}{\partial \chi} \right), \tag{4.5}$$

$$\frac{d\psi}{dt} = -v_{//} B \left(\frac{\partial \rho_{//}}{\partial \alpha} - \frac{\partial (\gamma \rho_{//})}{\partial \chi} \right), \tag{4.6}$$

$$\frac{d\chi}{dt} = v_{//} B \left(1 - \frac{\partial (\gamma \rho_{//})}{\partial \psi} + \frac{\partial (\beta \rho_{//})}{\partial \alpha} \right), \tag{4.7}$$

where $\rho_{//} = m v_{//} / qB$. In the above equations, $v_{//}$ is calculated from the energy conservation relation,

$$E = \frac{1}{2} m v_{//}^2 + \mu B + q\Phi . \tag{4.8}$$

At the turning point of the particle moving along the field line, $v_{//}$ changes its sign. In Eq. (4.7), the sign of $v_{//}$ is needed, while the others need only $v_{//}^2$. To avoid this difficulty, the equation for $\rho_{//}$ is solved with the following form:

$$\frac{d\rho_{//}}{dt} = \vec{v} \cdot \vec{\nabla} \rho_{//} = v_{//} B \left[\frac{\partial \rho_{//}}{\partial \chi} - \rho_{//} \left(\frac{\partial \rho_{//}}{\partial \alpha} \frac{\partial \beta}{\partial \chi} - \frac{\partial \rho_{//}}{\partial \chi} \frac{\partial \beta}{\partial \alpha} \right) + \rho_{//} \left(\frac{\partial \rho_{//}}{\partial \psi} \frac{\partial \gamma}{\partial \chi} - \frac{\partial \rho_{//}}{\partial \chi} \frac{\partial \gamma}{\partial \psi} \right) \right]. \tag{4.9}$$

For the rotation free field, the drift equations, (4.5), (4.6), (4.7) and (4.9), become simpler. In this case the second and the third terms in Eq. (4.2) become zero. Thus, the magnetic field is also represented as

$$\vec{B} = \vec{\nabla} \alpha \times \vec{\nabla} \psi = \vec{\nabla} \chi . \tag{4.10}$$

For the vacuum field, the drift equations of motion are shown as

$$\frac{d\alpha}{dt} = -\frac{\partial \Phi}{\partial \psi} - \left(\frac{\mu}{q} + \frac{qB}{m} \rho_{//}^2 \right) \frac{\partial B}{\partial \psi}, \tag{4.11}$$

$$\frac{d\psi}{dt} = \frac{\partial \Phi}{\partial \alpha} + \left(\frac{\mu}{q} + \frac{qB}{m} \rho_{//}^2 \right) \frac{\partial B}{\partial \alpha}, \tag{4.12}$$

$$\frac{d\chi}{dt} = \frac{q}{m} \rho_{//} B^2, \tag{4.13}$$

$$\frac{d\rho_{//}}{dt} = -\frac{\partial \Phi}{\partial \chi} - \left(\frac{\mu}{q} + \frac{qB}{m} \rho_{//}^2 \right) \frac{\partial B}{\partial \chi}. \tag{4.14}$$

In the numerical code, Eqs. (4.11) - (4.14) are solved by neglecting the finite beta effect on particle motions.

4.2.2 Collision Operators

When the particle orbit is followed for a long time, it is natural to include Coulomb collisions. The collision operators were developed for studying the behavior of

distribution function: the pitch-angle scattering operator and the energy scattering operator. For the pitch-angle scattering operator, the Lorentz type operator was used [94, 99, 100].

$$\frac{\partial f}{\partial t} = \frac{\nu_d}{2}\frac{\partial}{\partial \lambda}\left(1-\lambda^2\right)\frac{\partial f}{\partial \lambda}, \tag{4.15}$$

where $f(\mu, \lambda, t)$ is the particle velocity distribution function and $\lambda = v_{//}/v$. Here ν_d is the pitch-angle scattering frequency expressed as

$$\nu_d = \frac{3}{2}\left(\frac{\pi}{2}\right)^{\frac{1}{2}}\left(\frac{A_i}{A}\right)^2\left(\nu_{B_i}\frac{\Phi(x_i)-\Psi(x_i)}{x_i^{\,3}}\frac{Z^2 Z_{eff} n_e}{Z_i^{\,4} n_i} + \nu_{B_e}\frac{\Phi(x_e)-\Psi(x_e)}{x_e^{\,3}}\frac{m_e^{\,2} Z^2 n_e}{2^{1/2} m_i^{\,2} Z_i^{\,2} n_i}\right), \tag{4.16}$$

$$\nu_{B_i} = \frac{\Lambda e^4 Z_i^{\,4} n_i}{12\pi^{3/2}\varepsilon_0^2 m_i^{\,1/2} T_i^{\,3/2}} \quad \text{(for ions)} \tag{4.17a}$$

$$\nu_{B_e} = \frac{2^{1/2}\Lambda e^4 Z_i^{\,2} n_i}{12\pi^{3/2}\varepsilon_0^2 m_e^{\,1/2} T_e^{\,3/2}} \quad \text{(for electrons)} \tag{4.17b}$$

by using Braginskii's collision frequencies, ν_{B_i} and ν_{B_e} [101], where Λ is the Coulomb logarithm [89]. A_i, Z_i, n_i, m_i and T_i are the atomic mass, the ionic charge, the density, the mass and the temperature (in the unit of Joule) of the bulk ions, respectively. A and Z are the atomic mass and the ionic charge of the minority ions. Also n_e, m_e, and T_e are the density, the mass and the temperature of the electrons, respectively. In Eqs. (4.17a) and (4.17b), e is electronic charge, ε_0 is the permittivity in vacuum, and Z_{eff} is the effective ionic charge. In Eq. (4.16), x_e (x_i) denotes v / v_{T_e} (v / v_{T_i}), where v_{T_e} (v_{T_i}) is the electron (ion) thermal velocity. The functions Φ and Ψ in Eq. (4.16) are given by

$$\Phi(x) = \frac{2}{\pi^{1/2}}\int_0^x \exp(-t^2)dt, \tag{4.18}$$

$$\Psi(x) = (\Phi - x\Phi')/2x^2. \tag{4.19}$$

Next the mean value $\langle\lambda\rangle$ and the variance σ^2 of the pitch angle will be derived, where

$$\langle\lambda\rangle = \int_{-1}^{1}\lambda f\, d\lambda. \tag{4.20}$$

When λ is multiplied on the both sides of Eq. (4.15) and integrated with respect to λ,

$$\frac{d\langle\lambda\rangle}{dt} = -\nu_d\langle\lambda\rangle \tag{4.21}$$

is obtained. Similarly,

$$\frac{d\langle\lambda^2\rangle}{dt} = \nu_d\left(1-3\langle\lambda^2\rangle\right) \tag{4.22}$$

is obtained. It is noted that the variance σ^2 is equals to $\langle\lambda^2\rangle - \langle\lambda\rangle^2$. Therefore,

$$\frac{d\sigma^2}{dt} = \frac{d\langle\lambda^2\rangle}{dt} - 2\frac{d\langle\lambda\rangle}{dt}\langle\lambda\rangle = \nu_d\left(1-3\langle\lambda^2\rangle+2\langle\lambda\rangle^2\right). \tag{4.23}$$

It is also noted that

$$\frac{d\langle\lambda\rangle}{dt} = -\nu_d\lambda_0,\ \frac{d\sigma^2}{dt} = \nu_d\left(1-\lambda_0^2\right), \tag{4.24}$$

when f is the delta function proportional to $\delta(\lambda-\lambda_0)$. From the above equations, we can derive a useful expression for the Monte Carlo method of pitch-angle scattering. After a short time, τ, the pitch angle changes as

$$\lambda = \lambda_0(1-\nu_d\tau) \pm \left[\left(1-\lambda_0^2\right)\nu_d\tau\right]^{1/2}. \tag{4.25}$$

Here the sign of the last term is chosen randomly for describing the pitch-angle scattering process with the equal probabilities for plus and minus.

As for the energy scattering, the Lorentz scattering operator is given by

$$\frac{\partial f}{\partial t}=\frac{1}{v^2}\frac{\partial}{\partial v}\left[v^2\nu_{E_i}\left(vf+\frac{T_i}{m}\frac{\partial f}{\partial v}\right)+v^2\nu_{E_e}\left(vf+\frac{T_e}{m}\frac{\partial f}{\partial v}\right)\right], \tag{4.26}$$

where ν_{E_i} and ν_{E_e} are the energy-exchange frequency by ions and electrons,

$$\nu_{E_i}=\frac{\Lambda e^4 Z^2 Z_{eff} A_i n_e}{2^{5/2}\pi\varepsilon_0^2 A m_i^{1/2} T_i^{3/2}}\frac{\Psi(x_i)}{x_i}, \tag{4.27a}$$

$$\nu_{E_e}=\frac{\Lambda e^4 Z^2 A_i m_e^{1/2} n_e}{2^{5/2}\pi\varepsilon_0^2 A m_i T_e^{3/2}}\frac{\Psi(x_e)}{x_e}, \tag{4.27b}$$

respectively. By multiplying by $(1/2)mv^2 4\pi v^2$ and integrating with respect to v, the time derivative of the minority ion energy E is obtained from Eq. (4.26).

$$\frac{d\langle E\rangle}{dt}=-2\langle\nu_{E_i}E\rangle+3T_i\langle\nu_{E_i}\rangle+2T_i\left\langle\frac{d\nu_{E_i}}{dE}E\right\rangle-2\langle\nu_{E_e}E\rangle+3T_e\langle\nu_{E_e}\rangle+2T_e\left\langle\frac{d\nu_{E_e}}{dE}E\right\rangle. \tag{4.28}$$

With the same procedure for multiplying by $(1/4)\ m^2v^4 4\pi v^2$,

$$\begin{aligned}\frac{d\langle E^2\rangle}{dt}=&-4\langle\nu_{E_i}E^2\rangle+10T_i\langle\nu_{E_i}E\rangle+4T_i\left\langle\frac{d\nu_{E_i}}{dE}E^2\right\rangle\\&-4\langle\nu_{E_e}E^2\rangle+10T_e\langle\nu_{E_e}E\rangle+4T_e\left\langle\frac{d\nu_{E_e}}{dE}E^2\right\rangle.\end{aligned} \tag{4.29}$$

It is noted that ν_{E_i} and ν_{E_e} are considered as a function of E (or x in Eq. (4.16)). The variance for the energy scattering $\sigma_E^2\ (=\langle E^2\rangle-\langle E\rangle^2)$ is given as

$$\frac{d\sigma_E^2}{dt}=\frac{d\langle E^2\rangle}{dt}-2\frac{d\langle E\rangle}{dt}\langle E\rangle. \tag{4.30}$$

Here the mean temperature for ions and electrons is defined as

$$T=\frac{T_i\nu_{E_i}+T_e\nu_{E_e}}{\nu_{E_i}+\nu_{E_e}}. \tag{4.31}$$

When the initial energy is represented as E_0, the time derivatives of the mean energy as well as the variance are given by

$$\frac{d\langle E\rangle}{dt}=-2\nu_E\left[E_0-\left(\frac{3}{2}+\frac{E_0}{\nu_E}\frac{d\nu_E}{dE}\right)T\right],\quad \frac{d\sigma_E^2}{dt}=4TE_0\nu_E, \tag{4.32}$$

where ν_E is the total energy-exchange frequency given by

$$\nu_E=\nu_{E_i}+\nu_{E_e}. \tag{4.33}$$

From Eq. (4.32), an expression of the energy scattering is obtained for the Monte Carlo method as

$$E=E_0-(2\nu_E\tau)\left[E_0-\left(\frac{2}{3}+\frac{E}{\nu_E}\frac{d\nu_E}{dE}\right)T\right]\pm 2\left[TE_0(\nu_E\tau)\right]^{1/2}. \tag{4.34}$$

Here, the sign $\pm$ is also chosen randomly for describing the energy scattering process.

4.2.3 Particle Acceleration by ICRF Wave

It is known that the ICRF wave is absorbed by cyclotron damping in high temperature plasmas. It is noted that collisionless cyclotron damping [102] for the waves is the same as the absorption of the wave energy by the particles through the acceleration by the wave electric field at their cyclotron frequency. Here we will derive the change of the velocity [88] as ions pass through the cyclotron resonance layer. An ion moving along the magnetic field line passes through the resonant layer four times for each complete poloidal revolution around the magnetic axis as shown in Fig. 4.1.

The x and y components of the equation of motion of a charged particle perpendicular to $\vec{B}=B_0\hat{z}$ in the presence of $\vec{E}=(E_x\hat{x}+E_y\hat{y})e^{-i\omega t}$ are

$$\frac{dv_x}{dt} - \Omega v_y = \frac{q}{m} E_x e^{-i\omega t}, \tag{4.35}$$

$$\frac{dv_y}{dt} + \Omega v_x = \frac{q}{m} E_y e^{-i\omega t}, \tag{4.36}$$

where $\Omega(t)$ denotes the cyclotron frequency at the instantaneous particle position. By expanding $\Omega(t)$ around the time of the resonance satisfying $\Omega(t_0) = \omega$,

$$\Omega(t) = \omega + (t - t_0)\frac{d\Omega}{dt}(t_0) + \ldots \tag{4.37}$$

is obtained. For combining Eqs. (4.35) and (4.36), two variables, $E_\pm \equiv E_x \pm iE_y$ and $v_\pm \equiv v_x \pm iv_y$ are introduced. The plus sign denotes the left-hand polarization component and the other is the right-hand one. Then the two equations of motion are shown in the following from:

$$\frac{dv_\pm}{dt} \pm i\Omega(t)v_\pm = \frac{q}{m} E_\pm e^{-i\omega t}. \tag{4.38}$$

Here only the resonant driving term is considered and Eq. (4.38) is integrated,

$$v_+ \exp\left(i\int_{-\infty}^{t} \Omega(t')dt'\right) = v_+(-\infty) + \frac{qE_+}{m}\int_{-\infty}^{t} dt' \exp\left(\frac{i}{2}\frac{d\Omega}{dt'}(t'-t_0)^2 + i\phi_0\right). \tag{4.39}$$

In these calculations, it is considered that the particle passes through the resonance surface at $t = t_0$, and ϕ_0 denotes the phase difference between the particle and the electric field at $t = t_0$. To integrate the velocity change of the passing particle by the acceleration field, the upper limit of the integration is assumed to be a large value. Therefore, the last integration term becomes,

$$\frac{qE_+}{m}\int_{-\infty}^{t} dt' \exp\left(\frac{i}{2}\frac{d\Omega}{dt'}(t'-t_0)^2\right) \rightarrow \frac{qE_+}{m}\left(\frac{2\pi}{|d\Omega/dt|}\right)^{1/2} e^{\pm\frac{\pi}{4}i}. \tag{4.40}$$

The change of the v_+ is equivalent to the change of the $v_\perp$ since the ions are accelerated in the plane normal to the z direction. As a consequence, the change of the perpendicular velocity after passing through the resonance surface is represented as

$$\Delta v_\perp = \mathrm{Re}\left(\frac{qE_+}{2m}\left(\frac{2\pi}{|d\Omega/dt|}\right)^{1/2} e^{i\phi_0}\right). \tag{4.41}$$

The heating power in this code is determined as follows: the minority ions are accelerated by the waves as given by Eq. (4.41). A part of the energy of the minority ions is given to the bulk ions and electrons and the rest of the energy are lost by the fast ions escaping from the plasma. The energy transferred from the wave to the plasma is a sum of the deposition energy of the accelerated minority ions onto the bulk ions and electrons and the lost energy of the escaping ions. The input parameter that determines the input power is E_+. It is noted here that the same E_+ does not mean the same input power since the input power depends not only on E_+ but also on the plasma parameters such as the temperature and the density.

4.3 Numerical Algorithm

In the Monte Carlo code, three important physical processes are included, that is, the acceleration (or deceleration) process by RF wave, the collisional processes between the fast ions and the bulk plasma which includes several ion species and electrons, and the collisionless orbit calculation in the Boozer coordinates. The flow of numerical calculation is as follows:

(1) Give the initial velocities and positions to the fast ions. The velocity is chosen in consistency with the bulk ion temperature using the random numbers. The position of

the particle is determined to reproduce the density profile in the radial direction and is uniform in the poloidal and toroidal directions. Here the input parameters, shown in Table 4.1, are the RF electric field (E_+), the plasma density, the plasma temperature, the minority ion ratio, and so on. It is noted that the minority ion ratio is defined as the ratio of the minority ion density to the sum of the minority ion density and the bulk ion density.

(2) The drift orbit is followed with Eqs. (4.11) - (4.14). The position of each fast ion is determined discretely with the time interval Δt.

(3) The pitch-angle scattering and energy scattering are introduced with Eqs. (4.25) and (4.34). By this step the pitch angle and the energy of each particle are changed. The Coulomb energy transfer rate from the fast ions to the bulk ions and electrons is also calculated.

(4) Check whether the fast ion passes through the resonance surface or not. After it is confirmed, the change of perpendicular velocity is estimated and then it is added to the velocity of the fast ion.

(5) If the fast ion escapes from the plasma confinement region, the following of the fast ion orbit is terminated. In this case, the energy of the lost ion is counted as the energy loss.

Figure 4.2 shows the flow chart. In this investigation, the Heliotron-E magnetic field strength is modelled by the following simple form:

$$B = B_0\left[1 - \varepsilon_t \frac{r}{a_p}\cos\theta - \varepsilon_h\left(\frac{r}{a_p}\right)^{\ell}\cos(\ell\theta - m\phi)\right], \tag{4.42}$$

where B_0 is the magnetic field strength at the axis, r is the minor radius, a_p is the plasma minor radius, ε_t is the toroidal ripple, ε_h is the helical ripple, ℓ is the pole number, and m is the pitch number. Here the radial variable, r, corresponds to the flux function ψ, and θ (ϕ) denotes the poloidal (toroidal) angle. The following values are used in the calculation,

$$\varepsilon_t = 0.0909, \quad \varepsilon_h = 0.3, \quad \ell = 2, \quad \text{and} \quad m = 19.$$

The rotational transform profile is given by

$$\iota(r) = \iota_0 + (\iota_a - \iota_0)\left(\frac{r}{a_p}\right)^2, \tag{4.43}$$

where $\iota_0 = 0.51$ and $\iota_a = 2.5$.

4.4 Energy Conservation and Collisional Processes in the Numerical Treatment

In order to incorporate the orbit following with the collisional processes, the choice of the appropriate time step is important. When the shorter time step is selected, the calculation takes a longer time. On the other hand, numerical results are not accurate with a too large time step.

Three examples of the orbit following calculations, in which the time step was chosen to be 0.1 μsec, are shown in Fig. 4.3. These collisionless particle trajectories are plotted in the coordinates of (r/a_p, θ, ϕ). The particle energy is 100 keV and the magnetic field strength at the axis is 1.76 T. The initail pitch angle in Fig. 4.3(a) is $\pi/36$ rad, and the starting point is at (r/a_p, θ, ϕ) = (0.25, π rad, 0 rad). It is noted that $\phi = 0$ rad corresponds to the cross-section in Fig. 3.1. This particle orbit shows one of the passing particles. Figure 4.3(b) shows the orbit of the deeply trapped particle. The pitch angle is $\pi/2$ rad, and the

starting point is $(r/a_p, \theta, \phi) = (0.75, \pi \text{ rad}, 0 \text{ rad})$. The last figure is an example of the trajectory of the lost particle started at the point of $(r/a_p, \theta, \phi) = (0.75, \pi \text{ rad}, 0 \text{ rad})$ with the pitch angle of $7\pi/18$ rad. The energy conservation was assured by the numerical scheme to solve the differential equations for the orbit following. In Fig.4.3, the energy conservation after 10,000 steps was within 10^{-7} as a relative error.

Numerical results including the collisional processes in the Monte Carlo method are shown in Figs. 4.4(a) and (b). The former shows the behavior of relatively low energy particles. 1,000 particles were used for each calculation. At the initial state, all particles have the same energy and the same pitch angle in velocity space. For 10 keV particles, the velocity after 1 msec spreads widely by the pitch-angle scattering and the energy scattering as shown in Fig. 4.4(a). The initial point in the velocity space is indicated with the large open circle. The spread in the velocity space is narrower for the 100 keV particles (see Fig. 4.4(b)) as expected. The comparison of collision processes between the numerical (Monte Carlo) results and the analytic solutions was made for the check of the numerical procedure.

For the pitch-angle scattering, the mean value and variance of pitch angle are obtained analytically from Eqs. (4.21) and (4.22),

$$\langle \lambda \rangle = \langle \lambda \rangle_{t_o} e^{-\nu_d t}, \tag{4.44}$$

$$\langle \lambda^2 \rangle = \frac{1}{3}\left(3\langle \lambda^2 \rangle_{t_o} - 1\right)e^{-3\nu_d t} + \frac{1}{3}, \tag{4.45}$$

$$\sigma^2 = \langle \lambda^2 \rangle - \langle \lambda \rangle^2 = \frac{1}{3}\left(3\langle \lambda^2 \rangle_{t_0} - 1\right)e^{-3\nu_d t} - \langle \lambda \rangle_{t_0}^2 e^{-2\nu_d t} + \frac{1}{3}. \tag{4.46}$$

When the initial pitch angle is given by the delta function form, the mean value and variance are expressed as

$$\langle \lambda \rangle = \lambda_0 e^{-\nu_d t}, \tag{4.47}$$

$$\sigma^2 = \frac{1}{3}\left(3\lambda_0^2 - 1\right)e^{-3\nu_d t} - \lambda_0^2 e^{-2\nu_d t} + \frac{1}{3}. \tag{4.48}$$

The mean pitch angle and its variance given by Eqs. (4.47) and (4.48) are plotted in Fig. 4.5(a) for various initial energies with the fixed initial pitch angle of 45 degrees. The mean value decreases, as the energy becomes small because the parallel velocity of some particles becomes negative. The pitch-angle scattering in the Monte Carlo code is estimated using Eq. (4.25). If the large τ value, which is equivalent to the calculation time step, is used, the collision operators can not simulate the collisions in the plasma [78]. The following calculations, the time step was chosen to be $(10^{-3} - 10^{-4})\nu_d^{-1}$. The results obtained by Monte Carlo code in Fig. 4.5(b) agree well with the analytic results in Fig. 4.5(a). The errors of the mean values and the variances in the code calculation were less than 1% after 10,000 time steps. Therefore, the collision operators worked well with the time step 10^{-7} sec under the plasma conditions in Table 4.1. The difference between the calculation results with the time steps 10^{-7} and 10^{-8} was less than 0.1% after 0.1 msec. It was found that the time step 10^{-7} sec was sufficient in this investigation. In the low energy case of Fig. 4.4(a), the pitch angle spreads widely since the energy scattering is included in this calculation. Particle energy is reduced by the energy scattering with the low energy bulk particles, and the pitch-angle scattering occurs more frequently than in the case without the energy scattering. Thus, the pitch-angle scattering is enhanced with the energy scattering. The result of the energy scattering is summarized for the various initial energies in Fig. 4.6. In the higher-energy region of $\geq$ 40 keV, the relative change of energy is small, and the numerical results in Fig. 4.5(b) agree well with those in Fig. 4.6.

However, the discrepancy can be seen in the low energy region because of the energy scattering.

It is noted that it is difficult to solve Eq. (4.28) and Eq. (4.29) analytically. The term with $d\nu_{E_i}/dE$ and $d\nu_{E_e}/dE$ are negligibly small when the high-energy tail is considered. Thus, it is assumed that ν_{E_i} and ν_{E_e} are constant. Under this condition, the mean energy and its variance can be obtained analytically,

$$\langle E\rangle = \left(\langle E\rangle_{t_0} - \frac{3}{2}T\right)e^{-2\nu_E t} + \frac{3}{2}T, \tag{4.49}$$

$$\langle E^2\rangle = \left\{\langle E\rangle_{t_0}^2 - 5T\left(\langle E\rangle_{t_0} - \frac{3}{2}T\right) - \frac{15}{4}T^2\right\}e^{-4\nu_E t} + 5T\left(\langle E\rangle_{t_0} - \frac{3}{2}T\right)e^{-2\nu_E t} + \frac{15}{4}T^2, \tag{4.50}$$

$$\begin{aligned}\sigma_E^2 = \langle E^2\rangle - \langle E\rangle^2 = &\left(\langle E^2\rangle_{t_0} - \langle E\rangle_{t_0}^2 - 2T\langle E\rangle_{t_0} + \frac{3}{2}T^2\right)e^{-4\nu_E t} \\ &+ 2T\left(\langle E\rangle_{t_0} - \frac{3}{2}T\right)e^{-2\nu_d t} + \frac{3}{2}T^2 .\end{aligned} \tag{4.51}$$

If all of the particles are mono-energetic at the initial state,

$$\langle E\rangle = \left(E_0 - \frac{3}{2}T\right)e^{-2\nu_E t} + \frac{3}{2}T \tag{4.52}$$

and

$$\sigma_E^2 = \left(-2TE_0 + \frac{3}{2}T^2\right)e^{-4\nu_E t} + 2T\left(E_0 - \frac{3}{2}T\right)e^{-2\nu_d t} + \frac{3}{2}T^2 \tag{4.53}$$

are obtained from Eqs. (4.49) and (4.51). The analytic estimations of <E> and σ_E^2 are shown in Fig. 4.7(a). These results agree well with the Monte Carlo calculation shown in Fig. 4.7(b). The relative change of the mean energy and the ratio of the standard deviation to the mean energy are larger in the lower energy region. This is the reason of the larger pitch-angle scattering for the low-energy ions in Fig. 4.6. From these comparisons it was

confirmed that the numerical procedure works well, reproducing the relevant collisional processes.

4.5 Summary

In this chapter, the numerical model for analyzing the behavior of the fast ions was discussed. The guiding center equations in the Boozer coordinates were described first. Then, the Monte Carlo method was introduced. This technique is very useful to simulate the behavior of the minority ions in the ICRF heating since the fast minority ions can be considered to be test particles in the plasma. The Monte Carlo method is based on Coulomb collisions, which are essentially the random processes. Finally the acceleration by the ICRF wave was modelled as a change of particle energy when the fast ion moves across the ion cyclotron resonance layer in the Heliotron-E configuration.

The energy conservation during the orbit following in the numerical code has been checked. The relative error of the energy in Fig. 4.3 was 10^{-7}. This value was smaller than that of Ref. [94] where the relative error was 10^{-5}. The analytic solutions for the pitch-angle scattering and the energy scattering were derived for the comparison of these results with the Monte Carlo results. The accuracy of the model of Coulomb collisions depends on the time step in the calculation. As for the pitch-angle scattering, the results of the analytic solution and the Monte Carlo calculation without the energy scattering agreed well. However, the discrepancy of the results between the analytic solution and the Monte Carlo calculation with the energy scattering was found in the lower-energy region. The energy scattering effect was considered to be large in this energy region. This

consideration was confirmed by the comparison of results between the analytic solution and the Monte Carlo calculation for the energy scattering.

The agreement of the two results for the pitch-angle scattering (without the energy scattering) and the energy scattering was reasonably well with the time step 10^{-7} sec in the code. Therefore, the numerical procedure was found to be applicable to analyze the behavior of the fast ions produced by ICRF heating in the Helitoron-E experiment.

Density and Temperature

	center	edge	index 1	index 2
density	$1.5 - 6 \times 10^{19}$ m^{-3}	0.001 × central value	2	2
T_e	300 eV	0.001 × central value	2	2
T_i	500 - 700 eV	0.001 × central value	2	2

Profiles of temperature and density are defined as follow:

$$(central\ value - edge\ value)\left(1-\left(r/a_p\right)^{index1}\right)^{index2} + edge\ value\,,$$

where r is the minor radius and a_p is the plasma minor radius.

Majority ions:	deuteron
Minority ions:	proton or helium 3
Magnetic field strength:	1.76 T or 1.9 T

Table 4.1. Input parameters for the numerical code.

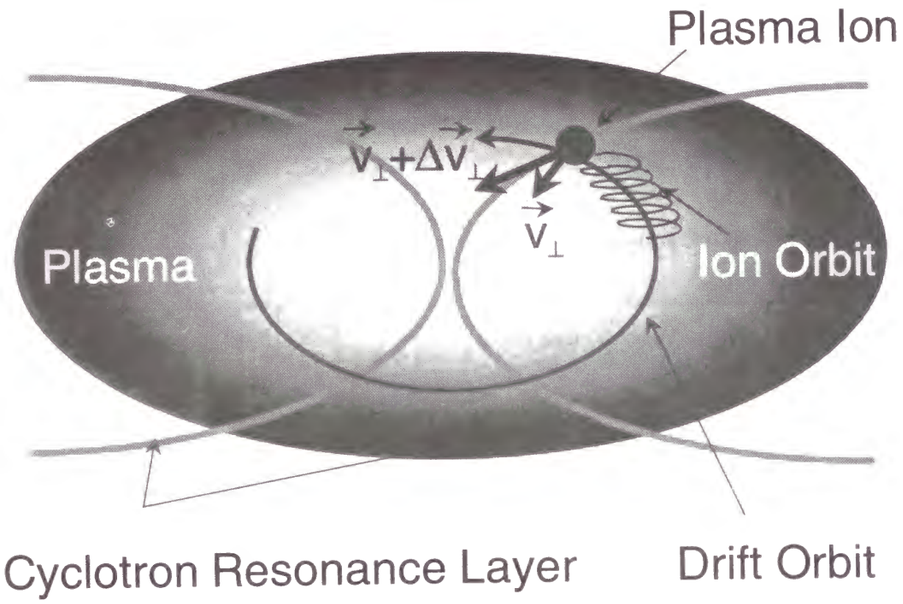

Fig. 4.1. A schematic view of the acceleration of the minority ion by ICRF waves at the cyclotron resonance layer.

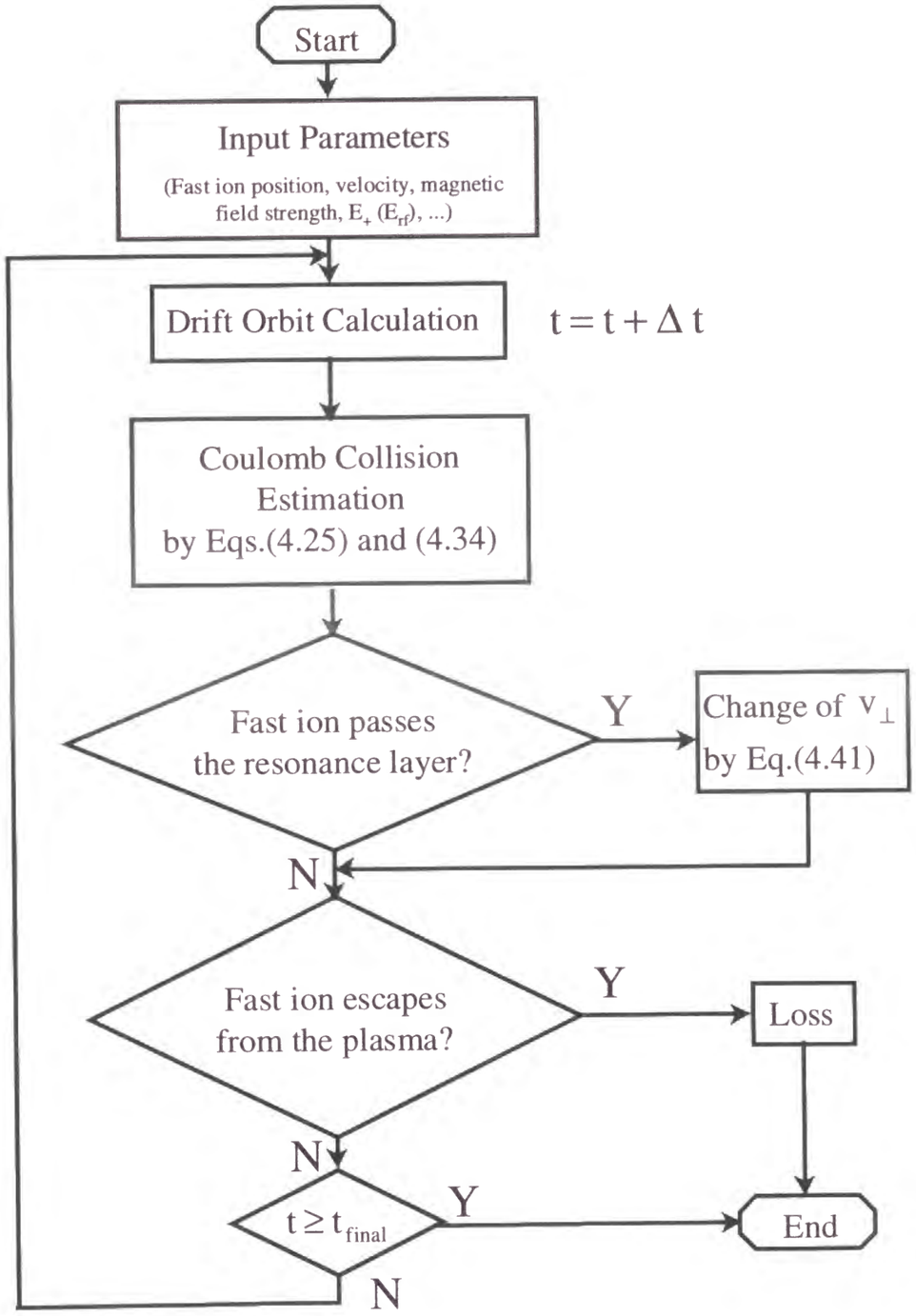

Fig. 4.2. Flow chart.

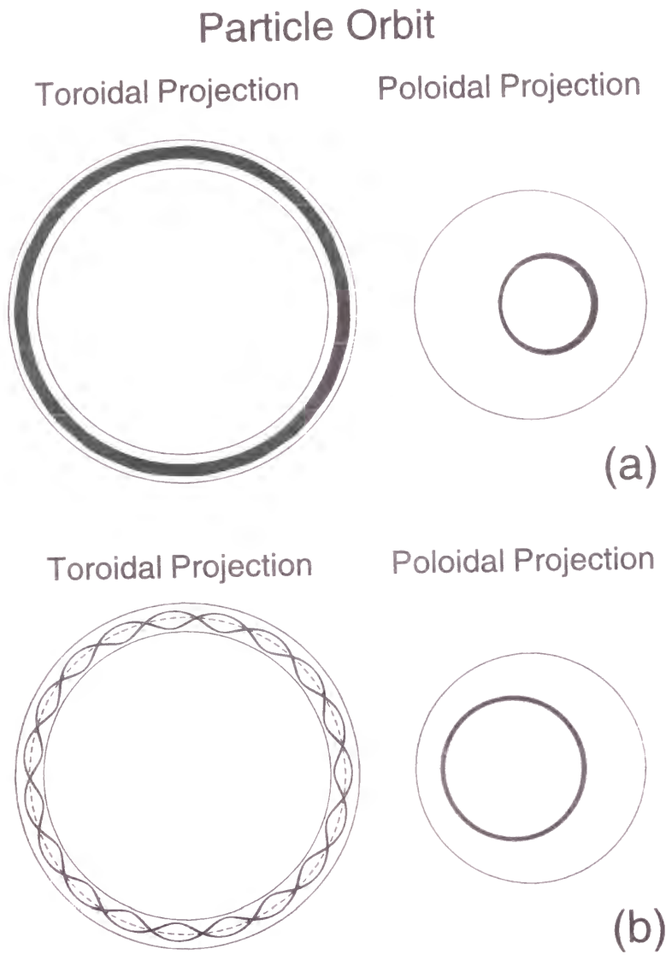

Fig. 4.3(a). A typical orbit trajectory for the passing particle. The left figure is the toroidal projection and the right one is the poloidal projection of the particle orbit. The initial pitch angle was $\pi/36$ rad, the initial energy was 100 keV, and the initial position was $(r/a_p, \theta, \phi) = (0.25, \pi \text{ rad}, 0 \text{ rad})$.

Fig. 4.3(b). A typical orbit trajectory for the deeply trapped particle. The left figure is the toroidal projection and the right one is the poloidal projection of the particle orbit. The initial pitch angle was $\pi/2$ rad, the initial energy was 100 keV, and the initial position was $(r/a_p, \theta, \phi) = (0.75, \pi \text{ rad}, 0 \text{ rad})$.

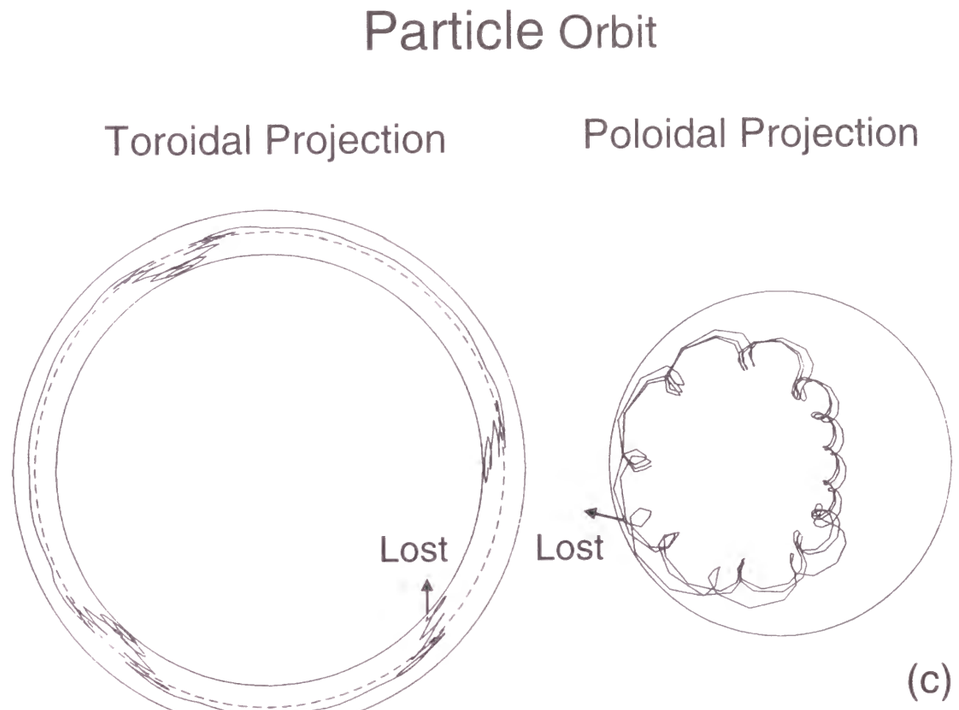

Fig. 4.3(c). An orbit trajectory for the lost particle. The left figure is the toroidal projection and the right one is the poloidal projection of the particle orbit. The initial pitch angle was $7\pi/18$ rad, the initial energy was 100 keV, and the initial position was $(r/a_p, \theta, \phi) = (0.75, \pi \text{ rad}, 0 \text{ rad})$.

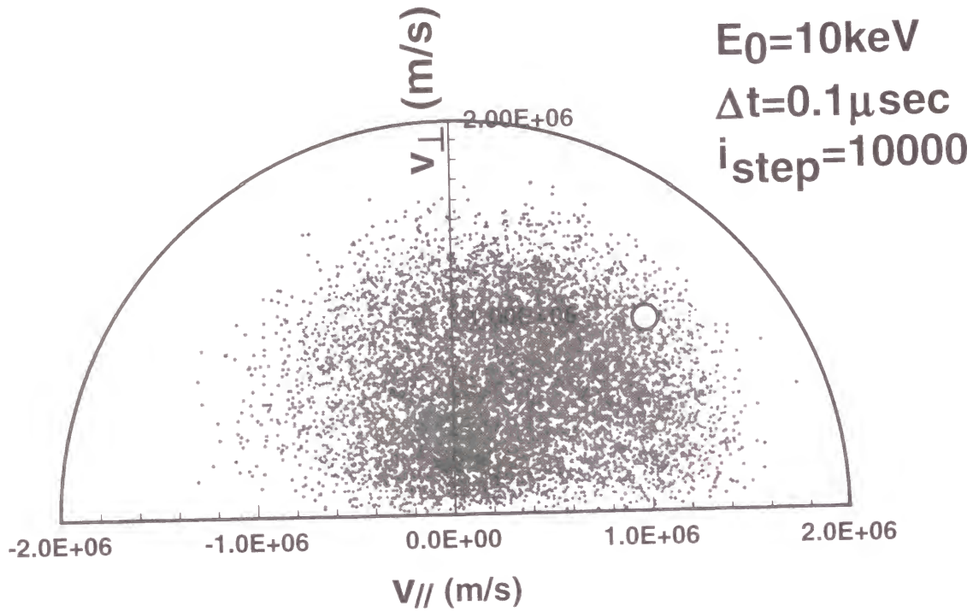

Fig. 4.4(a). The velocity scattering after 10,000 steps (time step is 0.1 μsec). The initial velocity is indicated by the large open circle (E_0 = 10 keV).

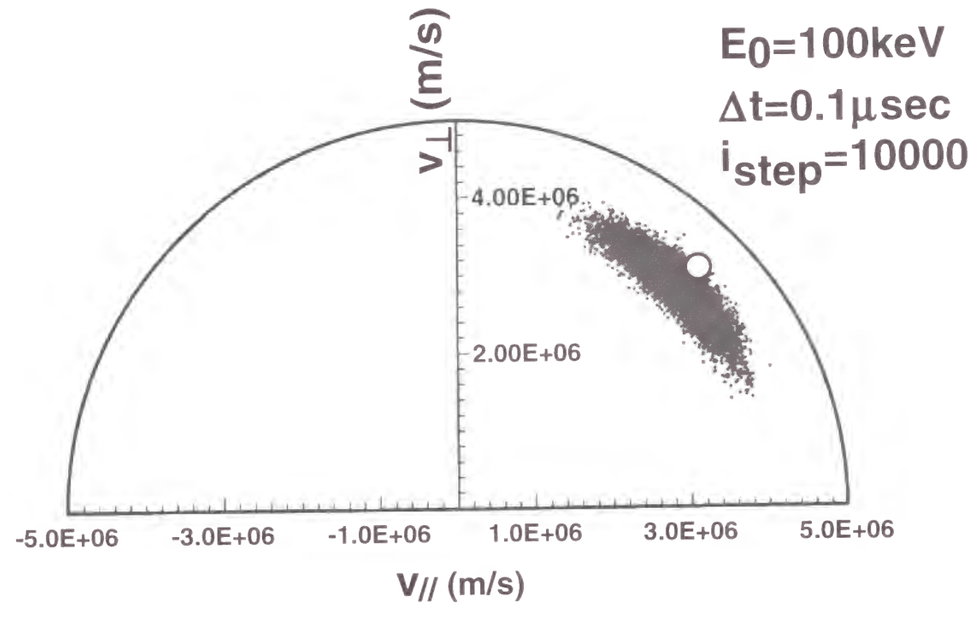

Fig. 4.4(b). The velocity scattering after 10,000 steps (time step is 0.1 μsec). The initial velocity is indicated by the large open circle (E_0 = 100 keV).

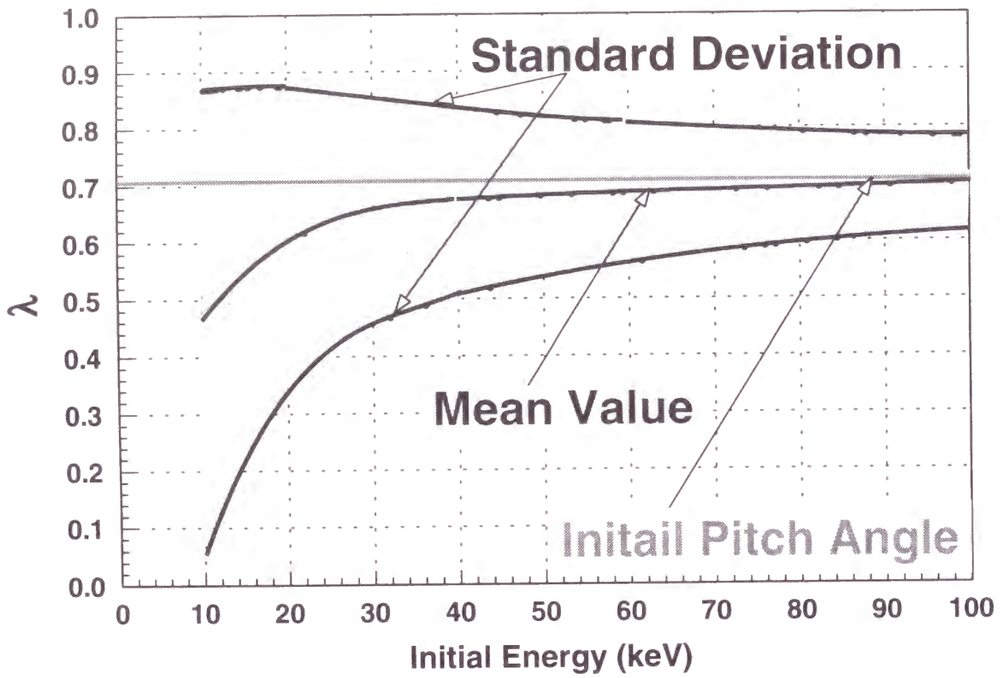

Fig. 4.5(a). Analytic pitch-angle scattering after 1 msec at various initial energies (the mean pitch angle and its standard deviation).

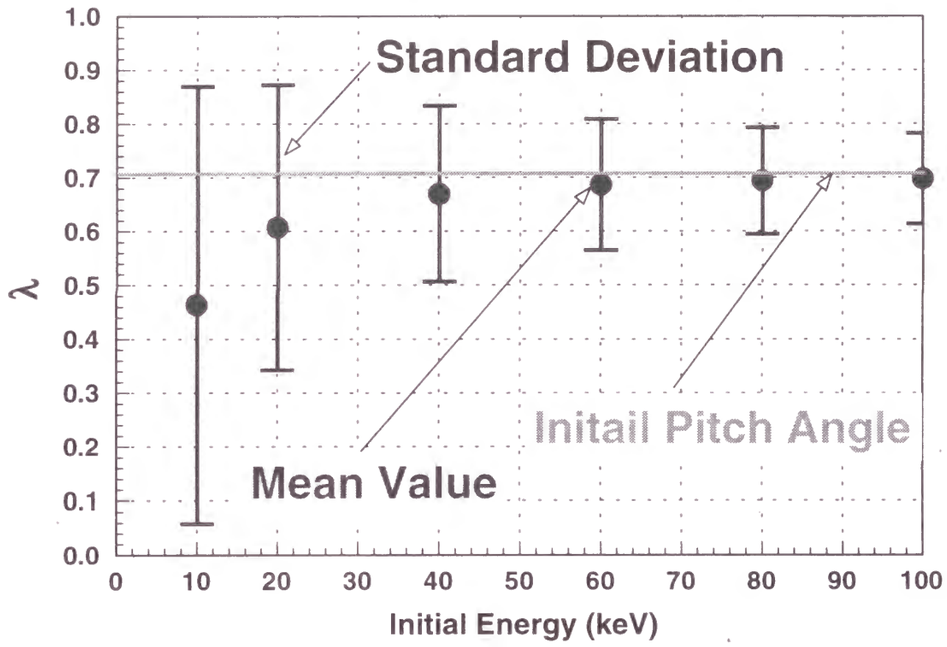

Fig. 4.5(b). The pitch-angle scattering by the Monte Carlo calculation after 1 msec at various initial energies (the mean pitch angle and its standard deviation without the energy scattering).

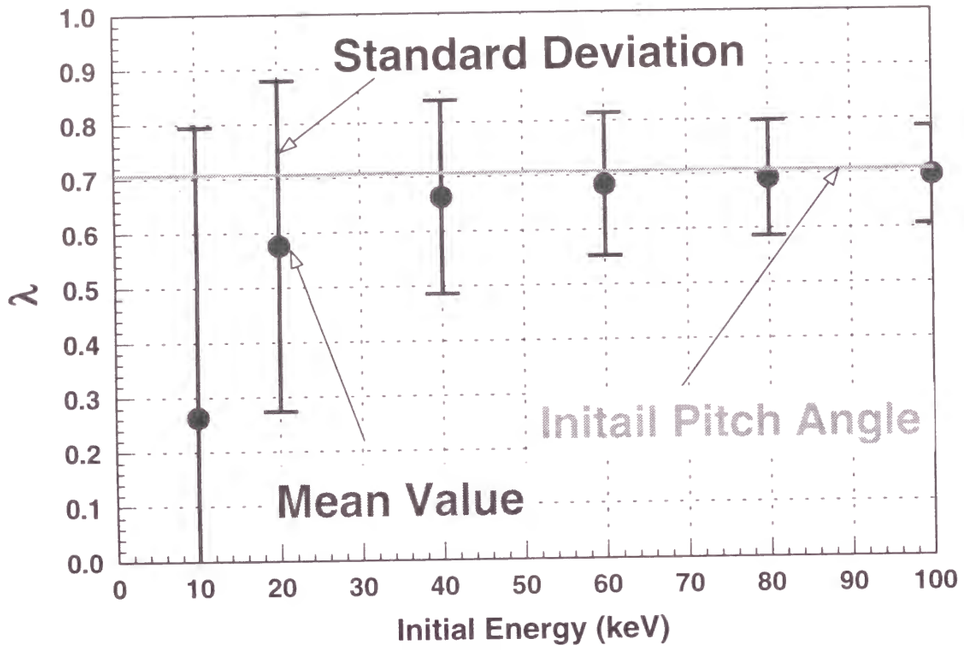

Fig. 4.6. The pitch-angle scattering by the Monte Carlo calculation after 1 msec at various initial energies (the mean pitch angle and its standard deviation with the energy scattering).

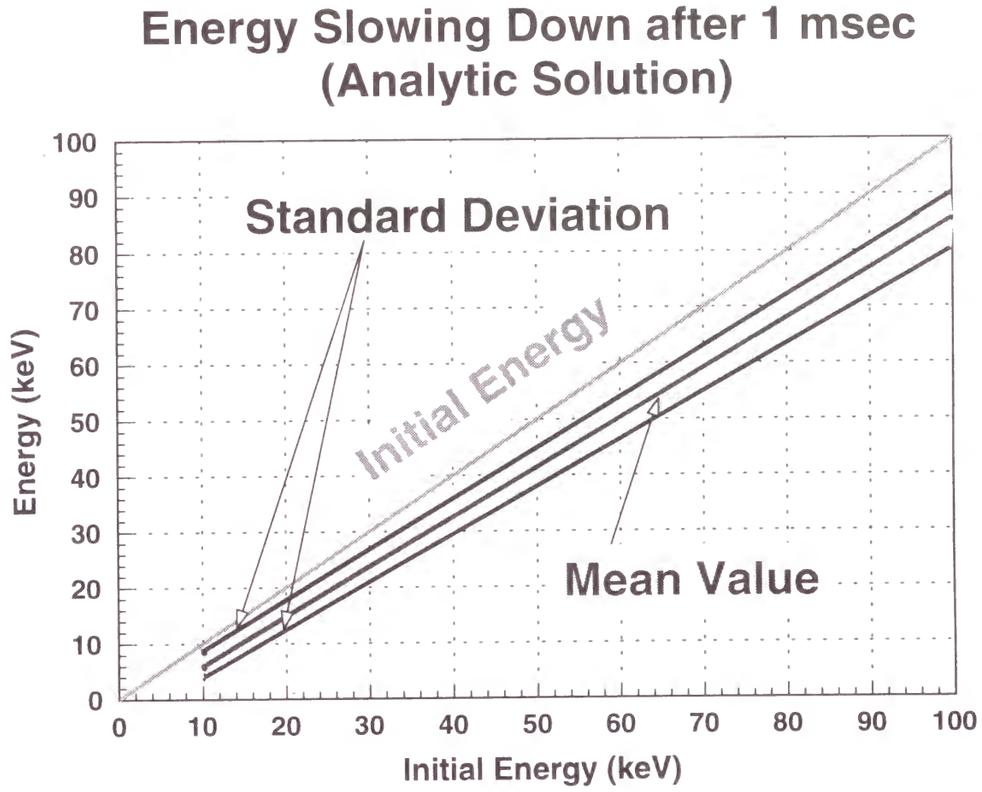

Fig. 4.7(a). Analytic mean energy and its standard deviation after 1 msec at various initial energies.

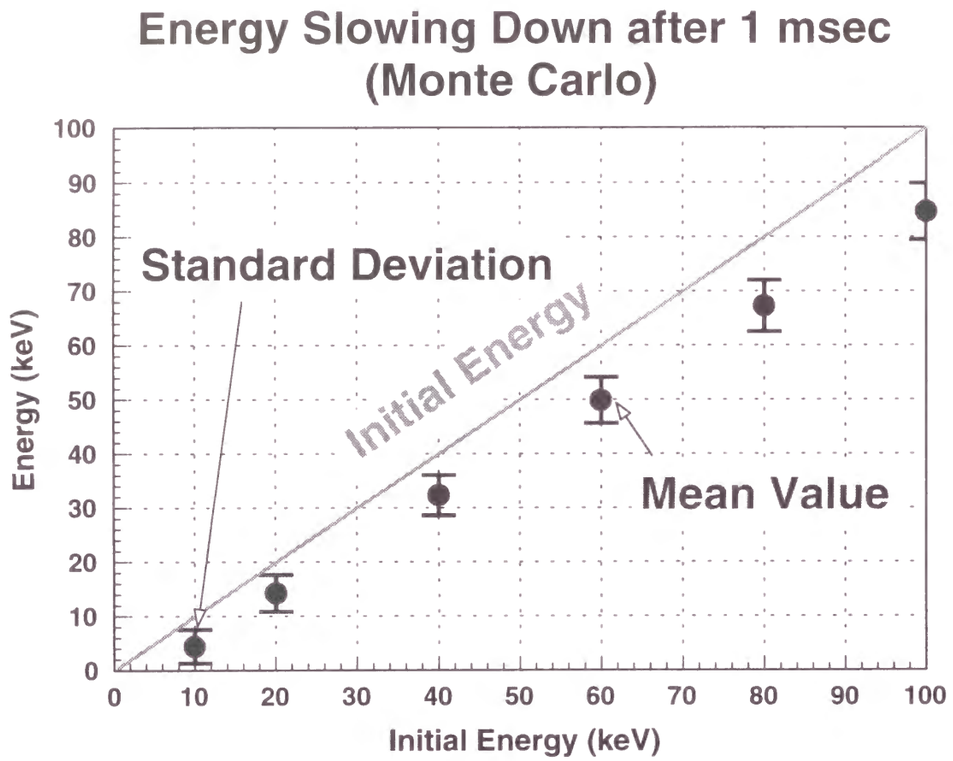

Fig. 4.7(b). Mean energy and its standard deviation by the Monte Carlo calculation after 1 msec at various initial energies.

Chapter 5

Simulation of the Fast Ions Produced by ICRF Heating

5.1 Introduction

A large number of fast ions were produced in the ICRF heating experiment of Helitoron E [24, 53]. The energy of accelerated ions up to 100 keV was measured by NPA. The production and confinement of these ions were studied through the change of the high-energy neutral particle fluxes. The high-energy tail in the minority-heating scheme was formed rapidly after the ICRF pulse was turned on. The decay times of the fluxes were, on the other hand, shorter than those expected from the classical collision theory.

To investigate the production and confinement of the fast ions, the numerical code described in Chap. 4 was developed for simulating the experimental results. Here the RF electric field profile should be determined for the calculation. For this purpose, the two-dimensional wave calculation is presented in Sec. 5.2. It is shown in Sec. 5.3 that the appearance of the high-energy tail should be very fast within 1 msec from the numerical calculation. It is also shown that the decay times of the neutral fluxes become shorter owing to an enhancement of orbit loss. The orbit loss can be the dominant loss channel for the high-energy ions.

The low-density operation is preferable for the fast ion production. However, as the collisionality decreases, the higher-energy particles tend to be lost since they might have larger loss cones in the three-dimensional confinement geometry. This means that the

high-density plasmas are preferable for the bulk plasma heating. The dependence of the heating efficiency on the density is also estimated numerically in Sec. 5.4. The orbit loss problem will be discussed in Sec. 5.5.

5.2 Absorption Profile of RF Electric Field

The RF electric field E_+ profile in Eq. (4.41) must be settled in order to simulate the experimental results using the numerical code [54, 95]. Usually many standing waves of the RF electric field are excited inside the plasma column in the fast wave heating [50]. The RF electric field excited by the ICRF antenna was numerically determined by the same code as shown in Ref. [50]. In this code, the magnetic field of Heliotron E is approximated with a straight helical magnetic field. The antenna is defined as the two-dimensional structure in the x-y plane. The abscissa is the x direction and the ordinate is the y direction as shown in Fig. 5.1(a). For the electric field calculation, the wave propagation equation is solved in the helically symmetric plasma with the hot plasma conductivity tensor. The boundary condition is that the vacuum wall shown in Fig. 5.1(a) as a racetrack shape is an ideal conductor. The profiles of the RF electric field components such as the real part of E_x and Imaginary part of E_y, the absorption powers by electrons, deuterons and protons ($P_{abs}^{electrons}$, $P_{abs}^{deuterons}$ and $P_{abs}^{protons}$) are shown as a contour plot. Solid lines represent the positive electric field and the broken lines represent the negative electric field. The plasma boundary is approximated with the elliptic shape, which is shown in the right three figures. Also the magnetic surfaces are assumed to be the nested ellipses. Plasma parameters such as the temperature and the density are given as functions of the magnetic surface. The real part of E_x and the imaginary part of E_y are shown in the

left two figures of Fig. 5.1(a). Here the electric field of the left-hand wave prevails over the plasma cross section. The profile of the left-hand component of the RF electric field is approximated with a parabolic form. The parabolic profile for the left-hand polarized RF electric field shown in Fig. 5.1(b) is assumed in the Monte Carlo calculations. The other three plots show the absorption profiles of RF power by the electrons, the deuterons (the majority ions), and the protons (the minority ions), respectively. In Fig. 5.1(c), the absorption power profiles are shown with an arbitrary unit. The dashed lines show the integrated absorption power as a function of radius. As a consequence of these calculations, most of the ICRF wave energy is found to be delivered to the minority ions (94%). Therefore, the major heating mechanism is the fundamental cyclotron damping. Second harmonic damping for majority deuterons (< 1%) and Landau damping and transit-time damping for electrons (6%) are negligibly small for this situation. Hereafter, in the numerical code, all RF power was assumed to be absorbed by the minority ion species. For the Monte Carlo calculations, 5,000 to 20,000 test particles are used.

The charge exchange process was neglected and the loss boundary of particle orbit was assumed to be at the last closed magnetic surface. For the Helitoron E plasmas, the charge exchange reactions may not be important in studying the fast particle confinement since the orbit loss is dominant compared with the charge exchange loss when the neutral density is less than 1.0×10^{15} m^{-3}. The definition of the loss boundary for the orbit following also changes the estimation of the orbit loss power. The estimation using the last closed magnetic surface as the loss boundary gives the upper limit of the orbit loss.

The radial electric field in the plasma is also important for the orbit following, especially in helical confinement devices [95, 103, 104]. The radial electric field in the

ICRF experiments was measured from the Doppler shift of the carbon line radiation in the Heliotron-E experiment [105]. Since the measured radial electric field was less than 2 kV/m in the range of density, $\bar{n}_e \approx 1.0\times10^{19}$ m^{-3}, this electric field does not affect the motion of fast ions with 20 – 100 keV drastically. If the larger electric field on the order of 5 kV/m (this value is equivalent to the potential difference of 1 kV in Heliotron E) is formed, the considerable change of the loss cone appears in the energy range below 40 keV [106].

The effect of the electric field on the trapped particles can be roughly estimated by the ratio of the angular frequency of the E×B drift motion, ω_E, to the angular frequency of the banana axis circulation, ω_h. ω_E and ω_h are defined as follow [2]:

$$\omega_E = \frac{E_r}{B_0 r}, \tag{5.1}$$

$$\omega_h = -2\ell\left(\frac{F(\kappa)}{G(\kappa)} - \frac{1}{2}\right)\varepsilon_h\omega_0, \tag{5.2}$$

$$F(p) = \int_0^{\pi/2}\left(1 - p^2\sin^2 x\right)^{1/2} dx, \tag{5.3}$$

$$G(p) = \int_0^{\pi/2}\frac{dx}{\left(1 - p^2\sin^2 x\right)^{1/2}}, \tag{5.4}$$

$$\omega_0 = -\frac{mv_\perp^2}{2qB_0 r^2}, \tag{5.5}$$

$$p^2 = \frac{E - \mu|B_0|(1 - \varepsilon_t(r)\cos\theta - \varepsilon_h(r)) - q\phi(r)}{2\mu|B_0|\varepsilon_h(r)}, \tag{5.6}$$

where E_r is the radial electric field, r is the position in the minor-radius direction, B_0 is the magnetic field strength at r = 0, ℓ is the pole number , ε_h is the helical ripple, ε_t is the

toroidal ripple, E, m, $v_\perp$, q and μ are the energy, the mass, the perpendicular velocity, the electric charge and the magnetic moment of a fast ion, respectively. If the ratio of ω_E/ω_h is near unity, the electric field effect can not be neglected. However, this value is 0.01 for the 100 keV ions under the present experimental conditions. Therefore, this electric field effect becomes small.

5.3 High-Energy Tail Formation

The velocity distribution of the fast ions under the steady-state condition was calculated with the developed code. The experimental ion and electron temperatures and densities were used in the calculation. Here the input parameter is the RF electric field, E_{rf} (the left-hand wave component, which is denoted as E_+ in Chap. 4). E_{rf} was estimated from the ICRF input power. The input power is defined to be the sum of the absorption power of the bulk particles via Coulomb collisions with accelerated ions and the delivered power to the high-energy tail ions. The saturated high-energy tails obtained by the Monte Carlo code are shown in Fig. 5.2 for the E_{rf}'s of 2,000 V/m and 1,000 V/m. Here the total absorbed power from RF wave is about 0.25 MW in the case of E_{rf} = 2,000 V/m or about 0.1 MW in the case of 1000 V/m. The velocity distributions of the minority protons in Fig. 5.2 agreed well with the measured ones shown in Fig. 3.8(a) for the case of the power level of 100 - 200 kW.

To analyze the tail formation processes and the loss mechanisms, the formation time of high-energy tail was calculated. In the initial stage, the tail portion of the minority velocity distribution is increased. The typical time evolution of the average energy of the

fast ions is shown in Fig. 5.3(a). The average energy is defined as $\overline{E} = \sum_{i}^{N} E_i / N$, where N is the number of fast ions and E_i is the energy of the i-th fast ion. The solid line represents the total energy and the broken line indicates the perpendicular component. In this theoretical model, the ICRF wave increases only the perpendicular velocity component of charged particle (see Eq. (4.41)). Therefore, almost all energy is the perpendicular component for the minority ions. The average energy increases until 1.5 msec from the start of the calculation, and then it saturates. This saturation is mainly caused by the increment of the loss energy due to the escaping ions from the confinement region. The loss energy ratio, which is defined as the ratio of the orbit loss energy to the total absorbed energy by the fast ions is shown in Fig. 5.3(b). It linearly increases until about 2 msec, and then the increment becomes small.

Figure 5.4 shows an example of the calculated time evolution of the velocity distribution of the fast ions in the case of E_{rf} = 2,000 V/m. The initial Maxwellian distribution was determined from the bulk ion temperature of T_i = 500 eV. The velocity distribution in the lower energy range saturates rapidly, however, the higher-energy tail increases slowly. It is seen that the velocity distribution below 20 keV saturates within 1 msec. This time scale is the same as the saturation time of the average energy of the fast ions. After 1 msec, the calculated orbit loss becomes the dominant energy loss for the higher-energy ions. However, the higher-energy portion of the tail does not saturate in this time scale. The reason is that in the higher-energy range, both the acceleration process and the orbit loss process become competitive. From the comparison between the experimental results and the numerical calculations, it is confirmed that the fast ion tail is determined by the competition among the RF acceleration, the collisional relaxation and

the orbit loss. This competition is balanced in a short time scale, about 1 msec, for the lower energy region.

5.4 Confinement of Fast Ions and Resultant Heating Efficiency

To simulate the measured decay times of the particle fluxes shown in Fig. 3.9, which are also shown in Fig. 5.5, the heating term was removed artificially after the velocity distribution have reached a stationary state. Figure 5.5 shows the dependence of the decay time of the particle flux on the particle energy by the experiment and the simulation. The decay time becomes shorter in the higher-energy range. Above 50 keV, the calculated decay time is less than 1 msec. In this high-energy range, ions are lost mainly by entering the loss cone with the small pitch-angle scattering. In this situation, there is only small particle source due to the relaxation from the higher-energy particles. In the low energy range, however, there is substantial particle source due to the slowing down from the higher-energy range since the loss region in velocity space becomes smaller. Therefore, the decay time also becomes longer. The decay time and its energy dependence obtained from the numerical code agree well with the experimental results as shown in Fig. 5.5. It is shown that the energy loss by escaping particles from the velocity space loss cone cannot be neglected after the high-energy tail is formed owing to the acceleration by the ICRF wave. From the viewpoint of the bulk plasma heating, it is better to suppress the high-energy tail formation by enhancing the energy transfer to the bulk particles.

For the estimation of the heating efficiency, the deposited RF power to the bulk particles and the total RF input power must be calculated. The injected RF power is considered to be equal to the RF power absorbed by the minority species, and then the

absorbed energy is distributed to the fast ions, the bulk ions, the electrons and the orbit loss ions. In the parameter region under investigation, the calculated power deposition ratio depends on the plasma density and the RF input power as shown in Fig. 5.6. The percentage of the power deposited on the bulk plasma is decreased and the orbit loss power is increased with the increase of RF power, or with the decrease of the density. When the input power (E_{rf}, here) is small, the acceleration of the minority ions is slow compared to the time scale of the collisional phenomena. Therefore, the average energy of the fast ions is kept low. Therefore, the deposition ratio is increased since the orbit loss is decreased. It was found that the deposition ratio shows the inversely proportional dependence on E_{rf} in the range of 1,000 V/m to 2,000 V/m. In the low-density range (2×10^{19} m^{-3}), Coulomb collisions of high-energy ions with the bulk particles are rare. In this case, the high-energy tail is easily formed. However, it should be noted that the particle orbit loss also becomes large and that the ratio of the energy deposited on the bulk particles becomes small. There is also the plot in the case of the higher density of $n_e(0) = 6\times 10^{19}$ m^{-3} in Fig. 5.6. The loss ratio is decreased to 0.46 at E_{rf} = 2,000 V/m. Due to the higher collision rate, the average energy of the high-energy tail is decreased, therefore, the orbit loss ratio is also decreased. As a consequence, the efficiency of energy transfer from the tail to the bulk plasma increases.

5.5 Discussion

It is shown that the fast ion production competes with the orbit loss as well as the energy transfer by Coulomb collisions. To understand this relation, the loss cone in velocity space was calculated. An example of the loss cone is shown in Fig. 5.7. The

trajectories of the ions started at the half-radius on the outer equatorial plane were calculated. Dots in this figure mean that the ion which had the initial velocity of the corresponding $v_{//}$ and $v_{\perp}$ in velocity space was not lost after traveling about 500 m. The total number of ions was 5,000. There are loss cones on both sides of the $v_{//}/v = 0$ line. From this figure, it is found that the loss cone becomes larger for the higher-energy ions and that the loss cone disappears in the very low energy region. Next, the collisional diffusion of particles in velocity space was investigated. In Fig. 5.8, the slowing down and pitch-angle scattering of the monoenergetic ions with the initial energy of 100 keV are shown. It is seen that within 1msec, the particle distribution in velocity space does not reach the loss cone. Therefore, a high-energy tail can be formed in the existence of the loss cones. In practice, some ions can be situated near the loss cone at the initial timing of the calculation. Therefore, the loss ratio is not zero just after the start of the calculation shown in Fig. 5.3(b). After the high-energy tail is formed, the velocity distribution is determined by the balance between the acceleration of the low energy particles by the ICRF wave and the orbit loss processes associated with Coulomb collisions, and then the orbit loss ratio also becomes constant.

The decay time of high-energy ions was calculated after the ICRF pulse was terminated. The numerical results were in general agreement with the observed values. The time evolutions of the loss power due to the orbit losses and due to the collisional energy transfer are shown in Fig. 5.9. The origin of the time is the termination timing of the ICRF pulse. After the ICRF acceleration was terminated, the orbit loss appears as the dominant loss channel until 0.6 msec. Thus, it is concluded that the orbit loss determines the decay time of the fast particle fluxes.

It is important to take into account the orbit loss just after the termination of the ICRF pulse. In other words, the estimation of the orbit loss is important in the presence of the high-energy tail. In the later phase of the tail decay process, the average energy of the fast ions is decreased since there is no acceleration by the ICRF wave. In this case, the contribution of the orbit loss is also decreased because the loss region in the low energy region is small. Therefore, the collisional energy transfer becomes dominant in the later phase.

5.6 Summary

The fast ion production and confinement were described in comparison of the experimental results with the numerical calculations. The steady-state velocity distributions in the experiment were reproduced by the Monte Carlo simulation. In the highest power case (0.82 MW), the numerical problem appeared in the Monte Carlo code. The number of the fast ions in the calculation became too small when the lost ratio was too high since no particle source term was involved in the code. In this case, the simulation result is not so reliable because of the statistical errors. The lost ions must be added in the proper manner for the more refined simulation. The magnitude of the RF field in the code was determined so that the RF input power becomes equal to the RF radiated power in the Heliotron-E experiment.

For analyzing the formation of the high-energy tail, the initial phase of the ICRF heating was also simulated. The numerical results showed that the obtained velocity distribution of the fast ions reproduced the experimental data to some extent. In the

experiment, the lower energy part of the tail was formed rapidly after the start of the RF pulse. According to the numerical results, the high-energy tail was formed within 1 msec.

The short decay time of the high-energy tail after the termination of the ICRF pulse in the experiment was explained with the simulation model. It was noted that the orbit loss can be the dominant loss channel in the presence of the large amount of the high-energy tail.

The deposition ratio of the heating power is a critical issue for the bulk plasma heating. As mentioned above, when the high-energy tail is formed, the energy loss is dominated by the orbit loss. It was confirmed that the high-density bulk plasma suppresses the tail formation with the enhancement of collisional processes. The quantitative estimation of the deposition ratio at various RF powers and plasma densities were made with the Monte Carlo code. In the high RF power and low-density case, the power deposition to the bulk particles became about 20% of the input power. The deposition power decreased almost linearly with the RF input power in this RF field range. By changing the plasma density at the center of plasma column from $2\times10^{19}\,m^{-3}$ to $6\times10^{19}\,m^{-3}$, which covers the range of the bulk-ion heating experiment, the power deposition ratio increased from 0.2 to 0.54 at E_{rf} = 2,000 V/m.

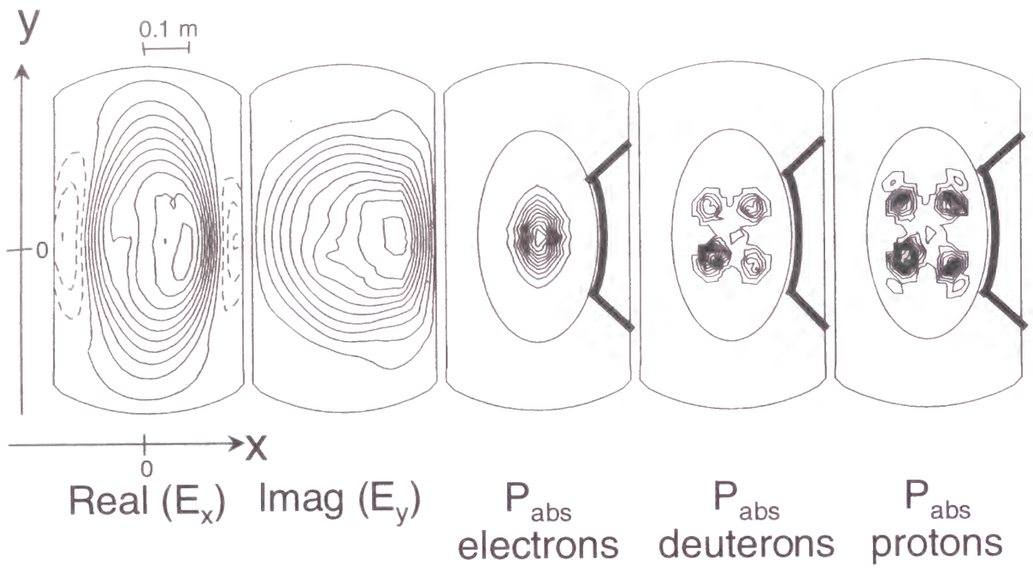

Fig. 5.1(a). From the left to the right, contours of Real (E_x), Imaginary (E_y) parts of RF electric field, electron absorbed power, majority ion absorbed power and minority ion absorbed power are shown. The percentages of the power absorbed by minority protons, majority deuterons and electrons are 94%, <1% and 6%, respectively. Input parameters are: $n_e(0) = 2.0 \times 10^{19}$ m^{-3}, $T_e(0) = 400$ eV, $T_i(0) = 600$ eV, B = 1.76 T, and the minority proton ratio is 0.1.

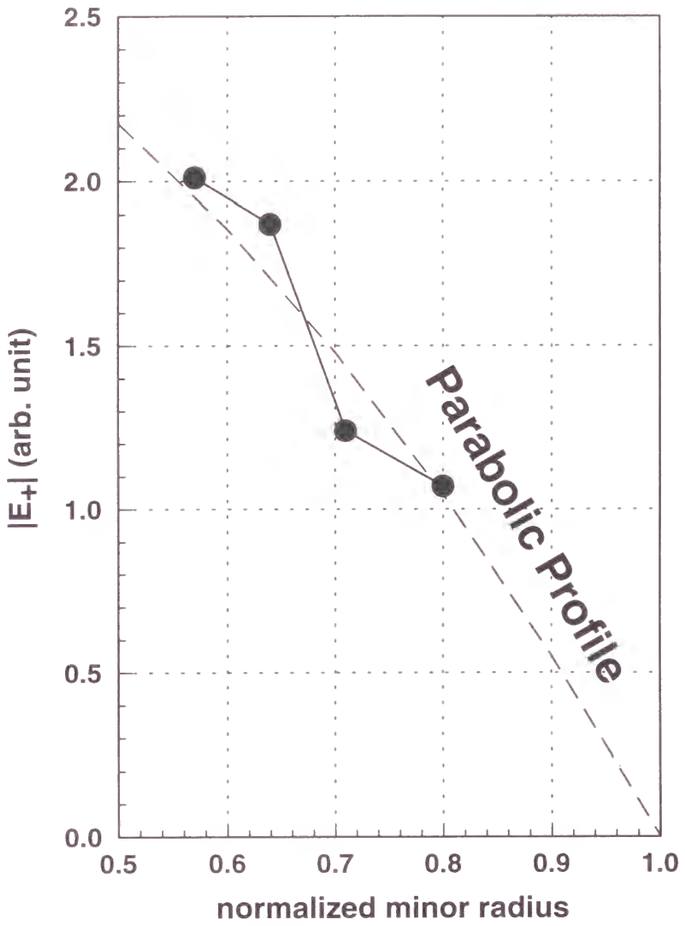

Fig. 5.1(b). The relative profile of the left-hand electric field $|E_+|$ in Fig. 5.1(a) (y = 0.14 m) as a function of the normalized minor radius. The parabolic profile is also illustrated as the reference.

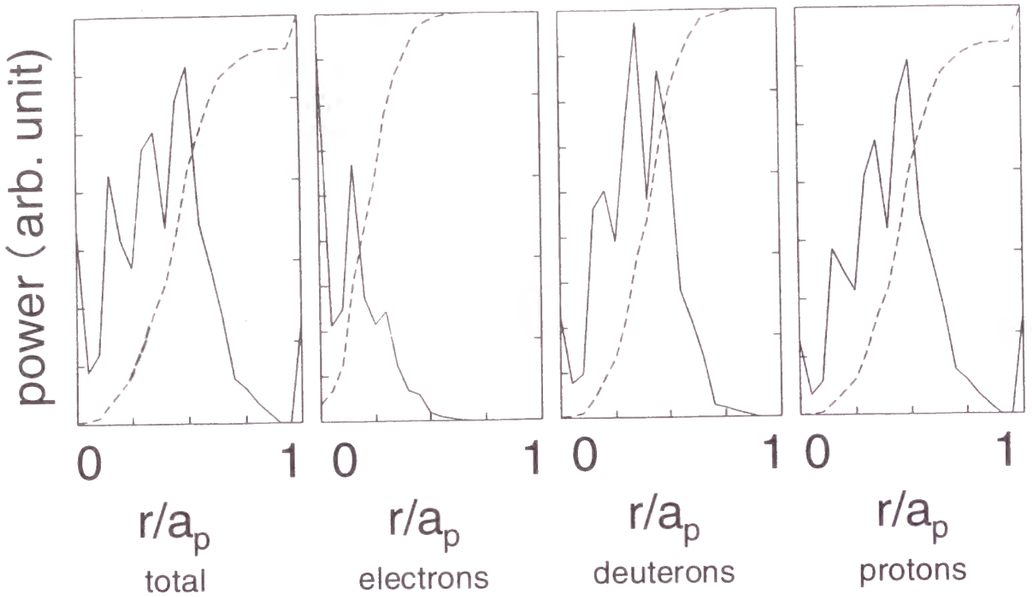

Fig. 5.1(c). Radial absorption profiles due to all species of charged particle, electrons, majority ions and minority ions, respectively. Input parameters are: $n_e(0) = 2.0 \times 10^{19}$ m^{-3}, $T_e(0) = 400$ eV, $T_i(0) = 600$ eV, B = 1.76 T, and the minority proton ratio is 0.1. The dashed lines show the integrated absorption power as a function of radius. The power absorbed outside the last closed magnetic surface is added to the value at the boundary ($r/a_p = 1$).

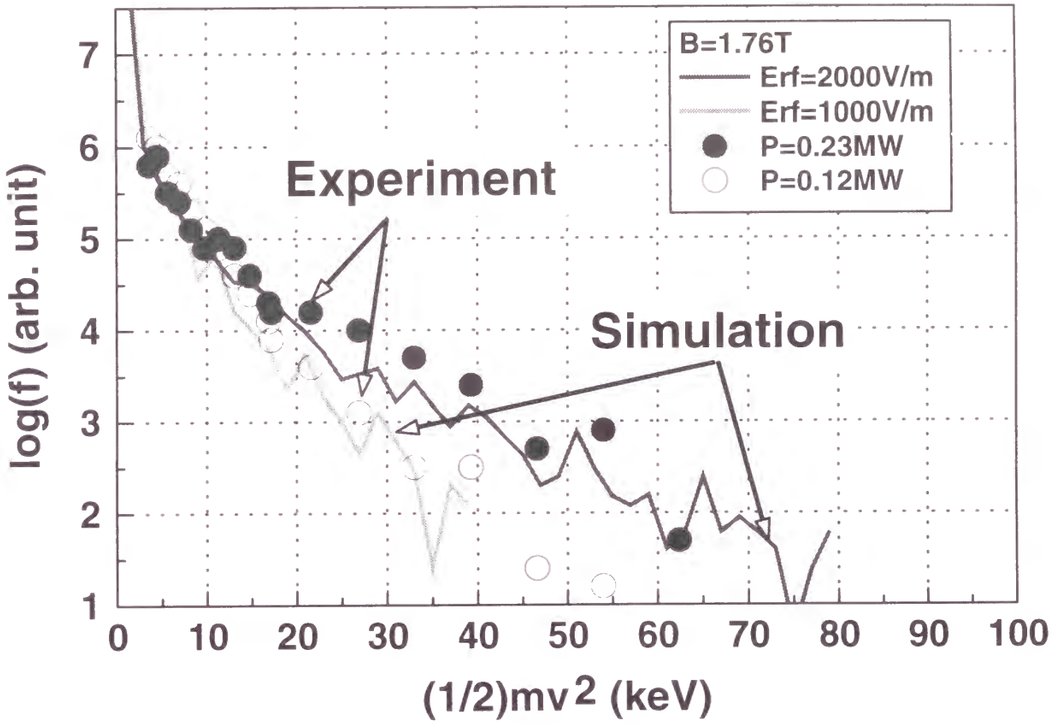

Fig. 5.2. Simulated minority-ion velocity distributions at various ICRF power levels with the number of minority ions of 5,000, $n_e(0) = 2.0 \times 10^{19}$ m^{-3} and $T_e(0) = 300$ eV. The tail temperatures from the calculation are 12 keV ($E_{rf} = 1000$ V/m) and 22 keV ($E_{rf} = 2000$ V/m), respectively.

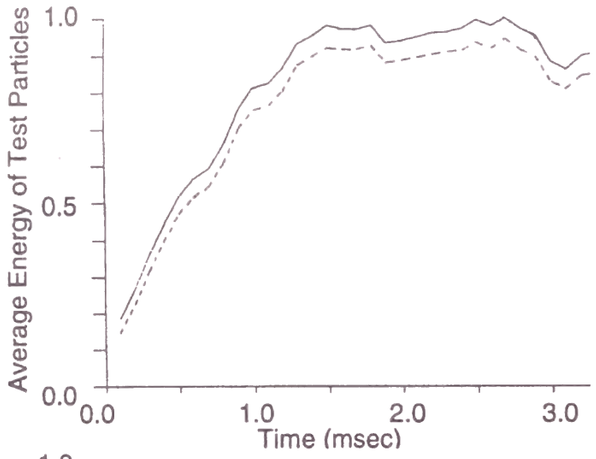

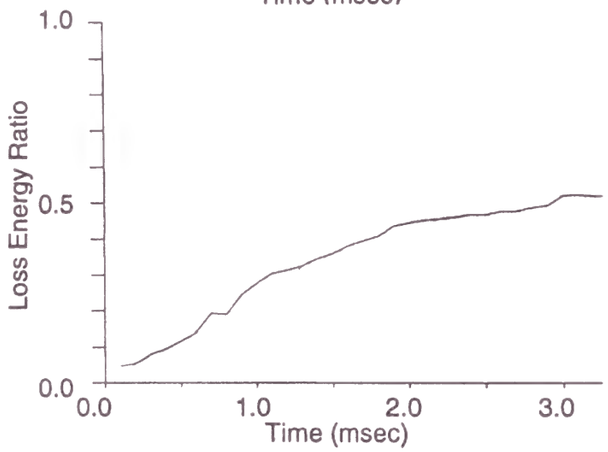

Fig. 5.3(a). Time evolution of the average energy of all fast ions. The solid line denotes the total energy and the broken line denotes the perpendicular component of the energy. The average energy is normalized with the value of maximum energy.

Fig. 5.3(b). Time evolution of the ratio of the loss power to the total absorbed power.

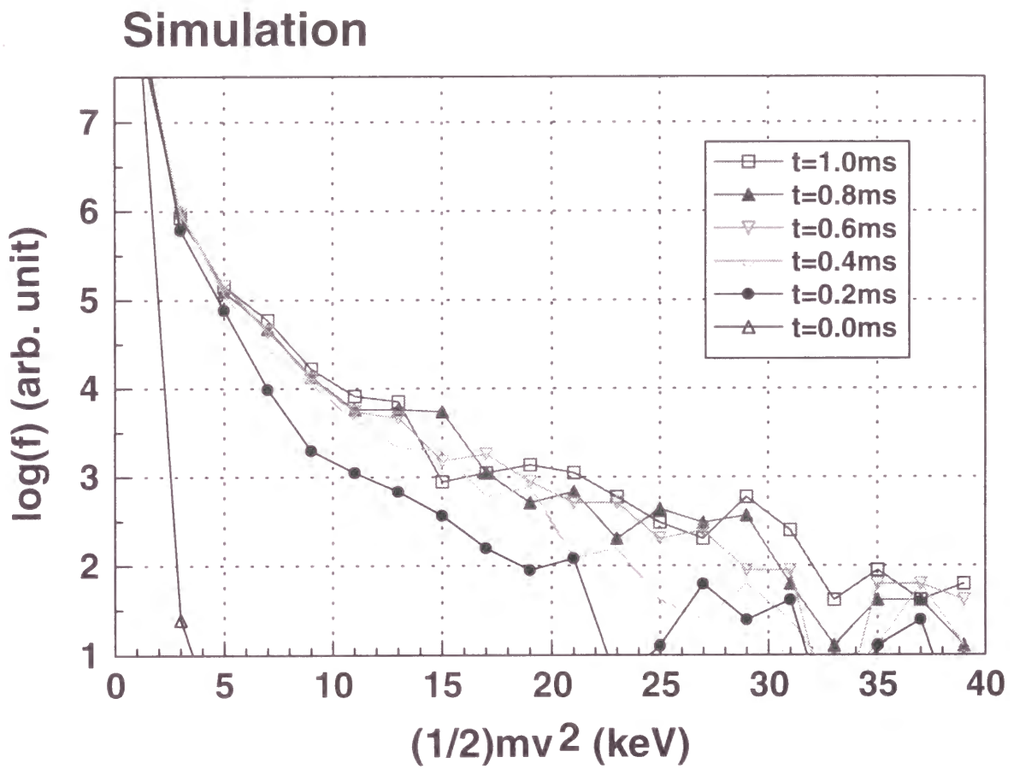

Fig. 5.4. Variation of velocity distribution during the initial 1 msec. The velocity distribution less than 20 keV becomes stationary within 1 msec.

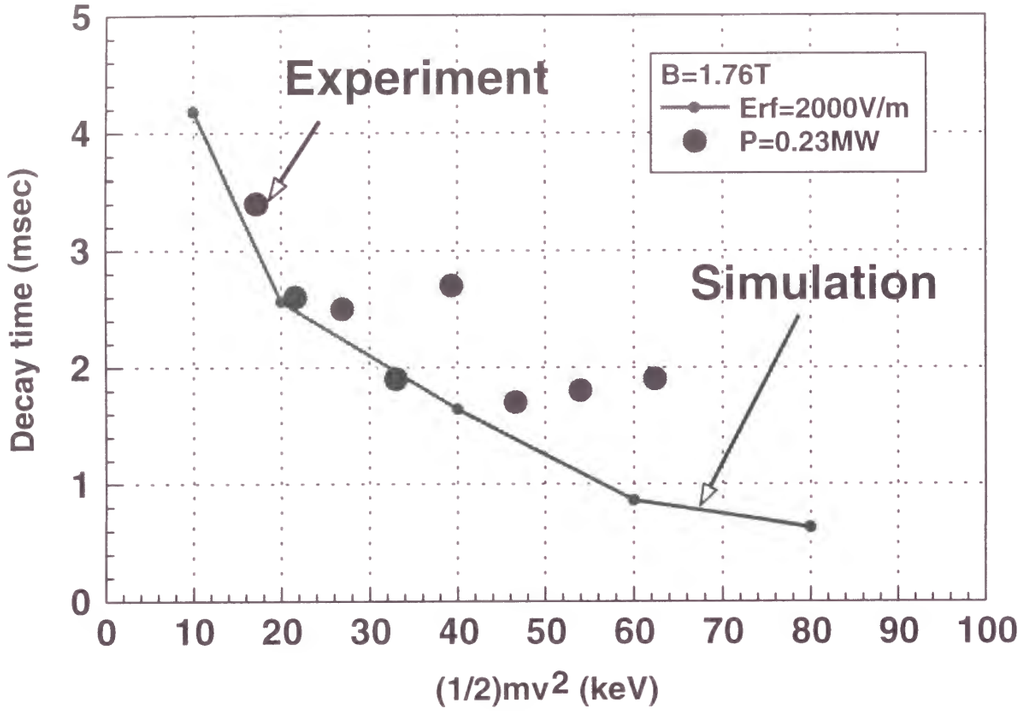

Fig. 5.5. Decay time of high-energy particle fluxes obtained from the numerical calculations after the termination of the ICRF wave pulse.

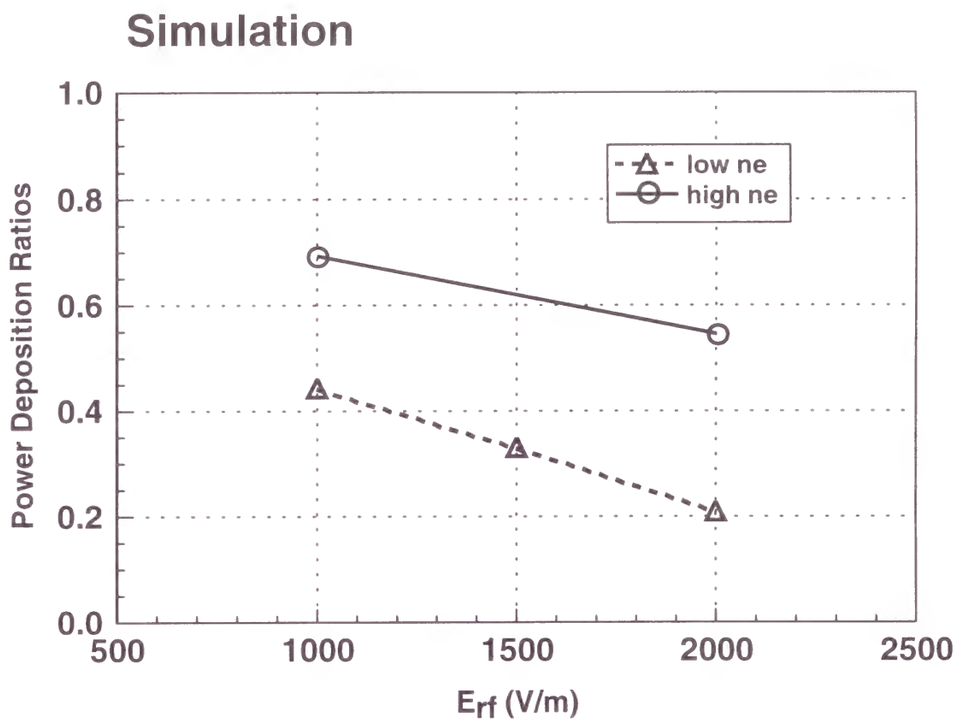

Fig. 5.6. Power deposition ratio, P_{bulk}/P_{ICRF}, is shown as a function of RF electric field. Here the power deposition ratio is defined as the ratio of the absorbed power by the bulk particles P_{bulk}, to the total input power P_{ICRF}. Triangles correspond to the low-density case of 2×10^{19} m^{-3} in Fig.3.8(a). Circles show the high-density case of 6×10^{19} m^{-3}.

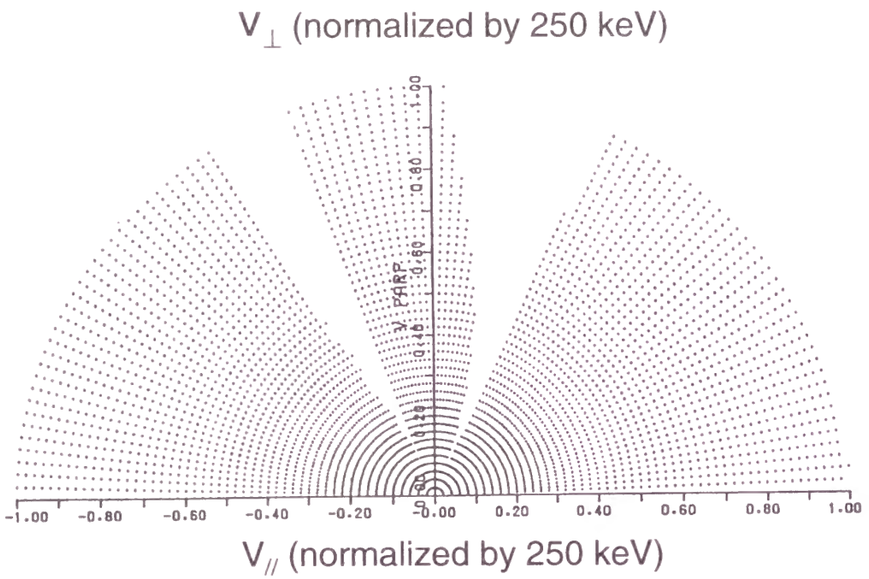

Fig. 5.7. Loss cone in velocity space ($v_{//}$, $v_{\perp}$), where $v_{//}$ and $v_{\perp}$ are the parallel and the perpendicular velocities of the test particles. The blank region in velocity space corresponds to the loss cone. All test particles start at r/a_p = 0.5 in the outer midplane of Helitoron E. The velocity is normalized by the value that corresponds to the energy of 250 keV. The magnetic field strength, $B_{\phi 0}$, is 1.76 T.

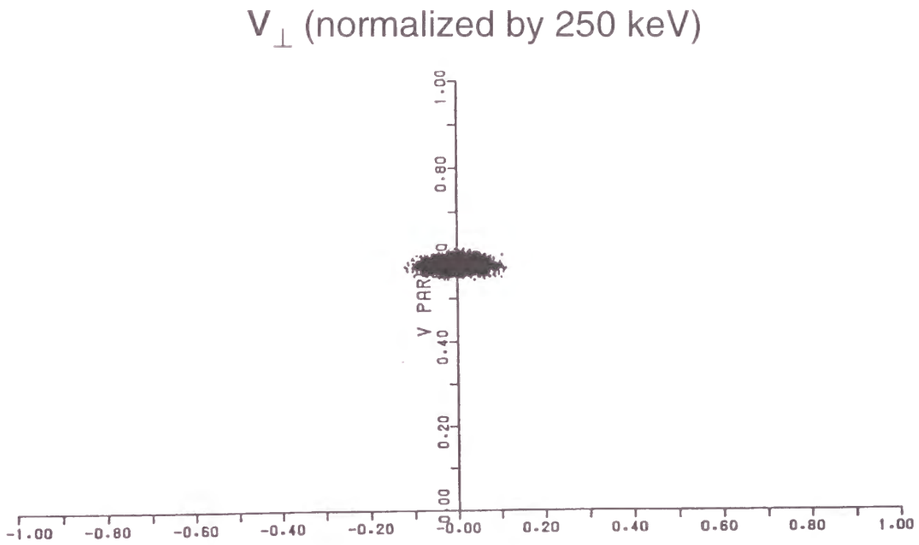

Fig. 5.8. Diffusion of particles in velocity space after 1 msec collisions in the case of $n_e(0)$ = 2×10^{19} m^{-3}, $T_e(0)$ = 300 eV and $T_i(0)$ = 500 eV as in Fig. 3.8(a). Here the initial particle velocity with $v_{//}$ = 0 is monoenergetic and the energy is 100 keV.

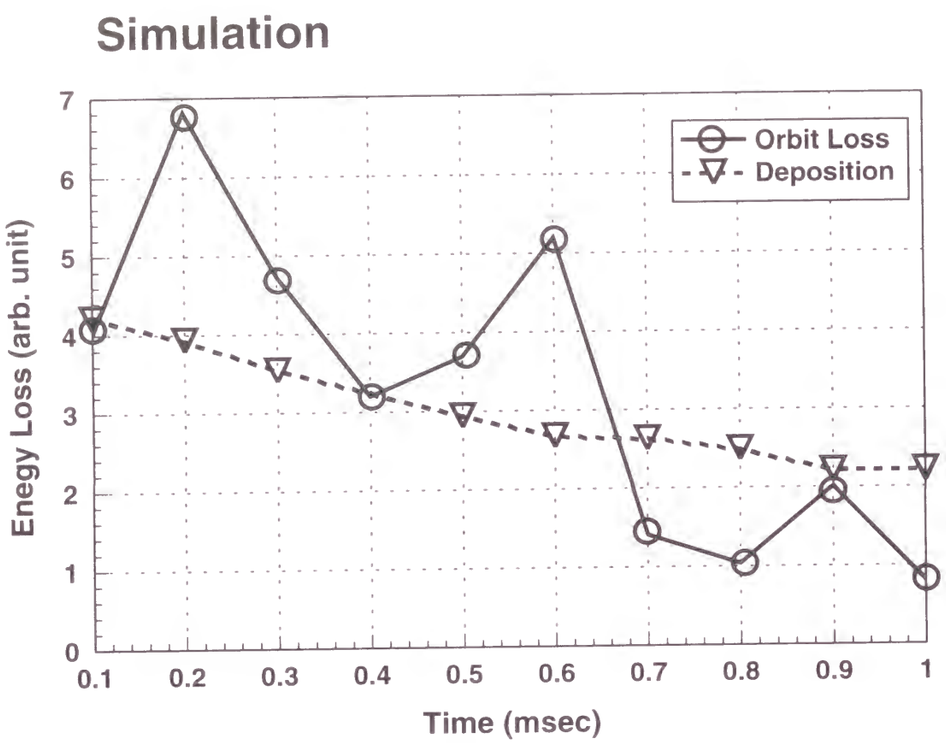

Fig. 5.9. Loss power of fast ions due to orbit loss (circles) and due to collisional energy transfer (triangles). At the end of the ICRF pulse, the time in the abscissa is chosen zero. Initially, the dominant energy loss channel is orbit loss. However, after t = 0.7 msec, the collisional energy transfer becomes the dominant loss channel.

Chapter 6

ICRF Heating with Helium Minority

6.1 Introduction

In the previous chapters, the ICRF heating results were discussed mainly from the viewpoint of the fast ion production and confinement. In this chapter, the experimental relationship between the fast ion production and the bulk heating efficiency will be discussed. The power deposition ratio of the minority ion heating depends chiefly on the plasma density and the imposed ICRF wave power. The increase of the heating efficiency is expected by replacing the minority hydrogen with the heavier species [107, 108]. The result of the heating experiment with ^{3}He-minority ions will be discussed in comparison with the hydrogen-minority case.

In ICRF heating with minority species, high-energy ions can be produced easily as discussed in Chap. 3. The high-energy ions should be confined for a sufficiently long time to heat the bulk particles through the collisional energy transfer. For helical devices, the fast ion confinement is a key issue because there can be a large loss cone in the velocity space [109, 110]. In a future fusion reactor, the high-energy ion tail enhanced by the ICRF wave will be utilized for the increment of fusion product by non-thermal reactions [1, 2]. D-^{3}He reaction is one of the promising reactions for a future fusion plasma [57, 111, 112]. Since $^3He^{2+}$ ion has the heavier mass and the doubled ionic charge number, the orbit loss and the charge exchange loss become smaller than those of proton and, therefore, more effective heating due to the helium minority can be expected

[95].

In ICRF heating of Heliotron-E plasmas, hydrogen or ^{3}He was used as the minority species [56]. From the measurements of the charge exchange neutral fluxes, the bulk deuteron temperature was 20 - 40% higher in the helium-minority case in the high power region. Helium minority has an advantage of its small particle loss region. The bulk heating is considered to be effective since the ion-ion collision cross section is larger and its charge exchange loss ratio is less than that of hydrogen. We will discuss the experimental data of the heating efficiency and the power loss due to the particle orbit loss in comparison with the numerical results based on the Monte Carlo code. The numerical results showed that the higher deposition ratio of approximately 40% could be obtained in the helium minority case. This numerical result agreed well with the experimental data in the high-power region.

The results of the minority heating experiment with ^{3}He or H minority will be discussed in Sec. 6.2. The velocity distributions in both the hydrogen-minority case and the helium-minority case are studied on the basis of the estimated orbit loss. The improvement of the heating efficiency will be discussed in Sections 6.3 and 6.4.

6.2 Experimental Comparison of the Bulk Heating Efficiencies in Helium-Minority Case and in Hydrogen-Minority Case

In the experimental setup shown in Fig. 3.4, two ICRF transmitters were used at the frequency of 17.8 MHz for the bulk plasma heating. The electron heating after the mode conversion at the hybrid resonance layer is also expected in the case of 1.9 T since the hybrid resonance layer is situated near the center of the minor radius. Four antenna pairs

(eight antenna loops) were used in the ^{3}He-heating experiment as in the H-minority case. The RF current with the same phase was fed to each of the antenna loops. Cross sections of the helical windings, the vacuum chamber, the ICRF antenna loops, the plasma surface, the cyclotron resonance and the cutoff layers are shown in Fig. 6.1 for the majority D^+ and minority $^3He^{2+}$ (for the case of D^+ and H^+, see Fig. 3.1).

The ICRF minority heating experiments in this chapter were performed with the toroidal magnetic field strength at the center of the minor radius, $B_{\phi 0}$ = 1.9 T and the line average electron density, $\bar{n}_e$ = 1.5-2.5$\times 10^{19}$ m^{-3}. The plasma confinement in the case of 1.9 T is better than that in the case of 1.76 T for the high-energy tail formation. The magnetic field strength and the electron density were set to be higher than those in the fast-ion production experiment. The target plasma was produced by applying ECH. The ECH input power was about 0.45 MW. The electron temperature of the target plasma was about 500 eV. ICRF pulse was injected during the ECH pulse. During the ICRF pulse, the electron density was almost constant. Figure 6.2 shows the dependence of the ion temperature on the RF power in both the H-minority and the ^{3}He-minority heating. The ion temperature of the bulk deuteron was measured by NPA, which was located in the opposite side of the torus with respect to the ICRF antenna position. The ion temperature was 20 - 40% higher in the ^{3}He-minority case especially in the high power region above 0.5 MW. Although the increment of the ion temperature in the H- minority case saturated as the ICRF power increased beyond 0.5 MW, the ion temperature in the ^{3}He-minority case increased linearly up to about 1 MW. The highest ion temperature, T_i = 1 keV, was obtained with the ^{3}He-minority ICRF heating. This result is consistent with the heating efficiency of 2.0×10^{19} keVm^{-3}MW^{-1} for $\bar{n}_e \approx 2\times 10^{19}$ m^{-3}.

The proton tail temperature was increased linearly from 12 keV to 20 keV with the input power even in the high power region for the H-minority experiment, although the bulk ion temperature saturates with the input power beyond 0.5 MW as shown in Fig. 6.3. Therefore, the tail temperature does not exactly represent the bulk heating efficiency. In Fig. 6.3, the electron temperature by the ECE signals was also presented. The electron density of this data set was slightly lower than that shown in Fig. 6.2, however, the obtained deuteron temperature was in the similar range and showed the same tendency against the RF power.

6.3 High-Energy Tail Formation for Helium ions and for Protons

The bulk ion temperature in ^{3}He-minority case increased even in the high power region as shown in Fig. 6.2. However, there was no measurement of energy spectrum of ^{3}He particle in these experiments. The difference between the dependencies of the ion temperature on the input power in Fig. 6.2 is expected to be due to the difference of the direct orbit losses and the charge exchange losses for the protons and the helium ions. By using the Monte Carlo code, the energy deposition ratios and the velocity distribution functions in both cases were estimated.

The calculated steady-state velocity distributions are shown in Fig. 6.4. The following plasma parameters were chosen in order to calculate the high-energy tail spectra. The ion and the electron temperatures are 500 eV, the line average electron density is 2×10^{19} m^{-3}, the effective ionic charge, Z_{eff}, is 3. Radial profiles of the temperature and the density are assumed to be $(1-(r/a_p)^2)^2$ in all cases. The initial velocity distribution of the fast ions is assumed to be Maxwellian, and the number of

fast ions is 5,000. The velocity distribution of ^{3}He ions and protons after they reached the steady state are shown in this figure*. The ICRF input power is chosen to be about 1.3 MW in both cases. The tail temperature of the ^{3}He-minority ions (16 keV) is higher than that of the minority protons (13 keV) since the orbit loss of ^{3}He-minority ions is less than that of protons and the acceleration rates are also different. The energy loss ratio due to the orbit loss in the hydrogen minority case was found to be 0.5 by the Monte Carlo code. On the other hand, the energy loss ratio due to the orbit loss in the ^{3}He-minority case was found to be 0.3. When the input energy was the same, the resulting energy transfer to the bulk particles was found to be higher in the helium 3 case by 40%.

Minority ions are accelerated in the perpendicular direction to the magnetic field. Therefore, the high-energy tail is anisotropic in this direction. Coulomb collisions slow down these fast ions and also scatter them isotropically in velocity space. If the high-energy ions enter into the loss cone during the slowing down process, the heating efficiency becomes small owing to the orbit loss. Here the loss cone structure was investigated for the protons and for the helium ions by the numerical code. The loss cones of the fast ions which started at the normalized radius, $r/a_p = 0.5$ in the outer equatorial plane of Heliotron E, are shown in Fig. 6.5(a) for the minority helium ions and in Fig. 6.5(b) for the minority protons. The loss cones for the protons appeared at the comparatively lower energy region ($E_{min} = 4$ keV) in Fig. 6.5(b). In the helium case, E_{min} was 7 keV. This result could explain the difference between the high-energy tail formations by ^{3}He ions and by protons in Fig. 6.4.

* It is noted that the charge exchange processes are not included in the numerical result of Fig.6.4.

6.4 Discussion

The kick of the ion, when it passes through the ion cyclotron resonance layer, or the increment of the velocity is represented by Eq. (4.41). From this equation, the perpendicular energy increment $\Delta E_\perp$ is given as follows:

$$\begin{aligned}\Delta E_\perp &= m v_\perp \Delta v_\perp \\ &= m\sqrt{\frac{2E}{m}}\frac{qE_{rf}}{2m}\left(\frac{2\pi}{|d\Omega/dt|}\right)^{1/2},\end{aligned} \tag{6.1}$$

where the phase factor is not expressed here. dΩ/dt in the denominator of the second expression can be expressed with the traveling length of the particle, s, and the velocity, v, and the magnetic field strength, B, as

$$\begin{aligned}\frac{d\Omega}{dt} &= \left(\frac{q}{m}\right)\frac{dB}{dt} \\ &= \frac{q}{m}\frac{\Delta B}{\Delta t} \\ &= \frac{q}{m}\frac{\Delta B}{\Delta s}v \\ &= \frac{q}{m}\frac{\Delta B}{\Delta s}\sqrt{\frac{2E}{m}}.\end{aligned} \tag{6.2}$$

With Eqs. (6.1) and (6.2) the energy increment is expressed as,

$$\Delta E_\perp = \left(\frac{mE}{2}\right)^{1/4}\left(q\pi\left|\frac{\Delta s}{\Delta B}\right|\right)^{1/2}E_{rf}. \tag{6.3}$$

This value denotes the maximum increment after a particle with energy, E, passes through the ion cyclotron resonance. If the particle has the same energy in the same wave field, E_{rf}, it receives the additional energy proportional to $q^{1/2}m^{1/4}$. From this consideration, the acceleration of the ^{3}He ions by ICRF waves is larger than that of

protons. The higher-energy tail obtained by the Monte Carlo code in the helium minority case in Fig. 6.2 is consistent with this analytic estimation.

The accelerated fast ions transfer their energy to the bulk ions and the electrons by Coulomb collisions. The advantage of the ^{3}He-minority scheme for the bulk ion heating is the higher ratio of the energy transferred to the ions to that to the electrons. The critical energy, at which the ratio is unity, is given in Eq. (3.11). The fast ions with the energy above this critical energy will transfer more energy to the electrons than to the bulk ions. When E_{crit} is larger, the ions are heated selectively. E_{crit} is proportional to the minority mass, therefore, the ^{3}He minority is preferable for the ion heating than the proton minority. The experiment revealed this behavior qualitatively.

6.5 Summary

In the minority ion heating experiment in Heliotron E, the higher ion temperature was obtained in the ^{3}He-minority case. Although the ion heating efficiency in the H-minority case decreased as the ICRF power increased beyond 0.5 MW, the ion temperature in the ^{3}He-minority case increased linearly up to 1 MW. The highest ion temperature, T_i = 1 keV was obtained with the ^{3}He-minority ICRF heating (The increment of the ion temperature by the ICRF heating was 0.8 keV).

The experimental information of the ^{3}He-minority ions could not be obtained in the Heliotron-E ICRF heating. Therefore, only the numerical analysis was carried out in order to investigate the difference between the heating efficiencies by the H minority and the ^{3}He minority. The results of the Monte Carlo simulation agreed well with the experimental results qualitatively. The tail temperature of the ^{3}He minority was higher

than that of the H minority. The simulation showed that the orbit loss was large especially in the hydrogen-minority case while in the ^{3}He-minority case the orbit loss was small. The resultant energy transfer to the bulk particles was found to be higher in the ^{3}He-minority case by 40% in the Monte Carlo simulation. This improvement can be partially explained by considering the acceleration rate by the ICRF wave and the energy transfer rate to the bulk ions from the fast ions.

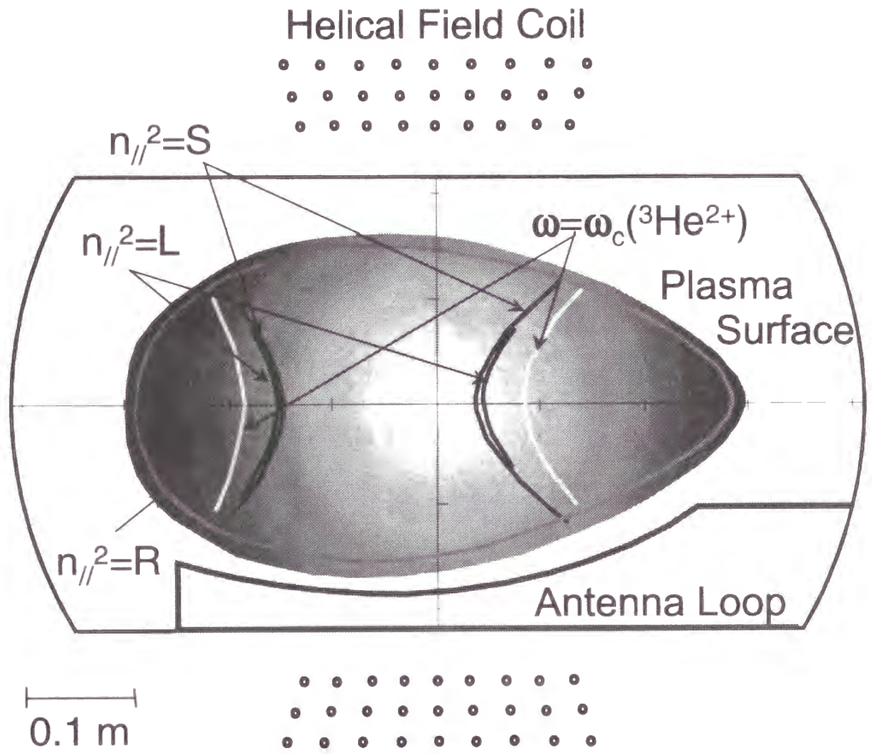

Fig. 6.1. A schematic view of the plasma cross section. The cyclotron resonance ($\omega = \omega_c(^3He^{2+})$), the two-ion hybrid resonance ($n_{//}^2$ = S), the right-hand cutoff ($n_{//}^2$ = R), and the left-hand cutoff ($n_{//}^2$ = L) layers are shown for the parameters: $B_{\phi 0}$ = 1.9 T, $n_e(0) = 4.0\times10^{19}$ m^{-3}, the frequency f=17.8 MHz and the minority ratio of 0.1. Antenna loops are installed on the high field side.

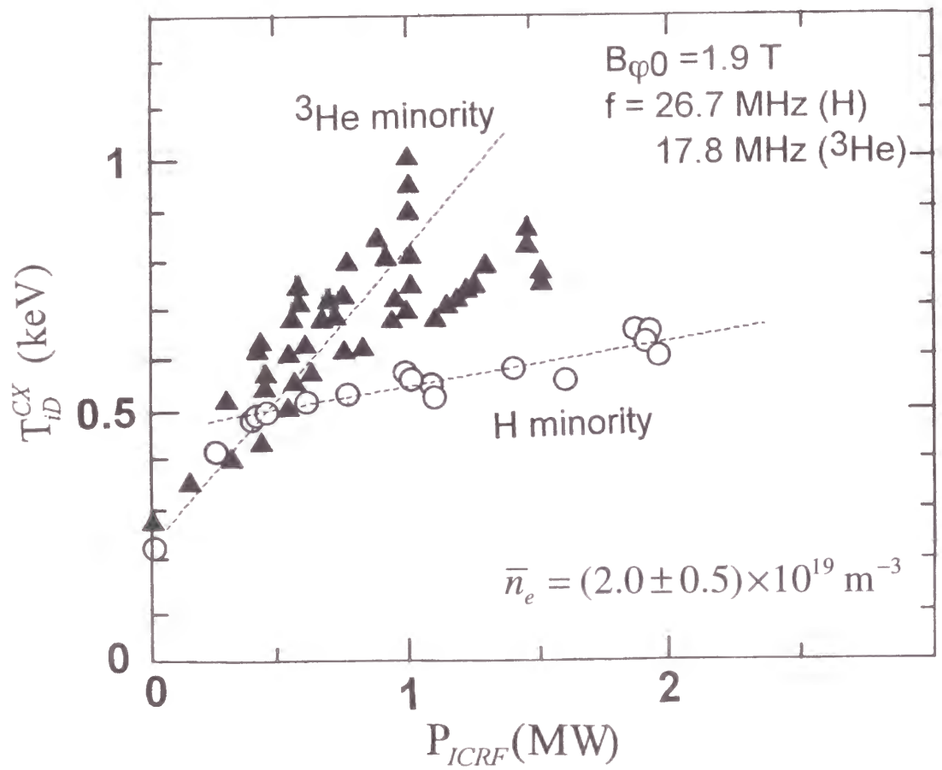

Fig. 6.2. Ion temperature of bulk deuterons measured by the neutral particle energy analyzer as a function of the transmitter power P_{ICRF}. The radiated RF power from the antenna is estimated to be $(0.6 - 0.7) \times P_{ICRF}$.

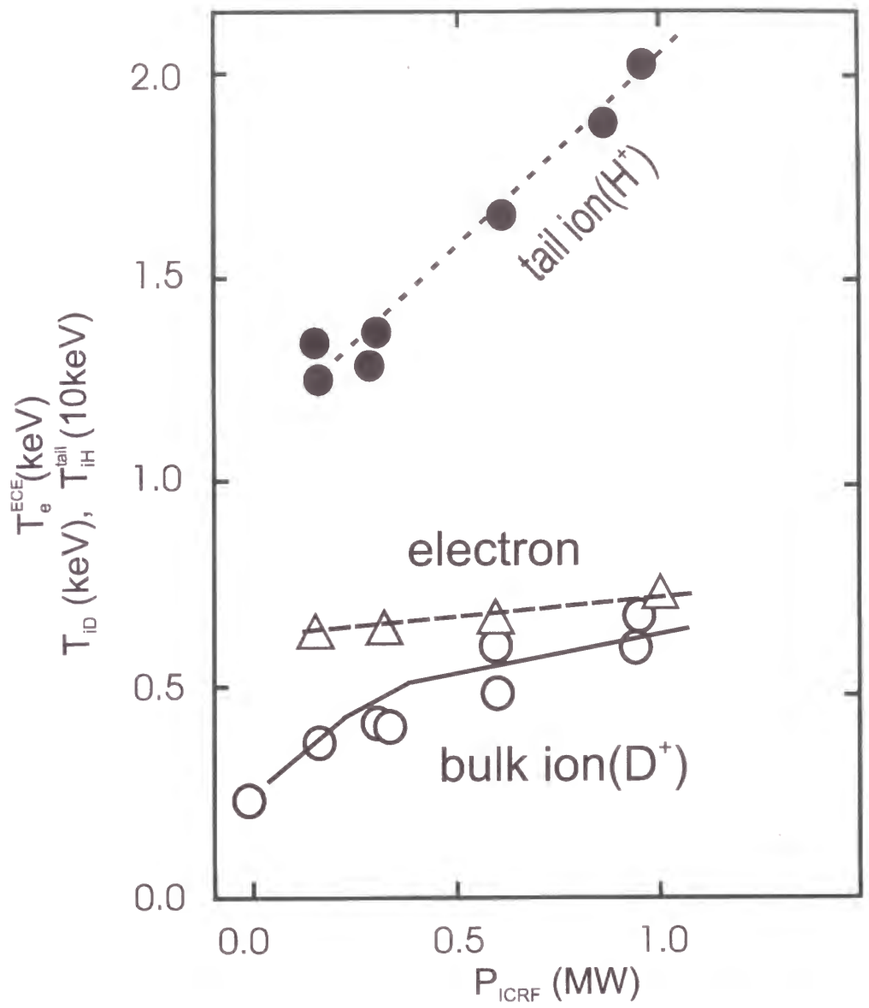

Fig. 6.3. The bulk deuteron temperature and the proton tail temperature measured by NPAs, and the electron temperature by ECE signal as a function of ICRF power: $B_{\phi 0}$ = 1.86 T, $\overline{n}_e$ = 1.3 - 1.5 $\times 10^{19}\ \mathrm{m}^{-3}$ and $T_e(0)$ = 800 eV.

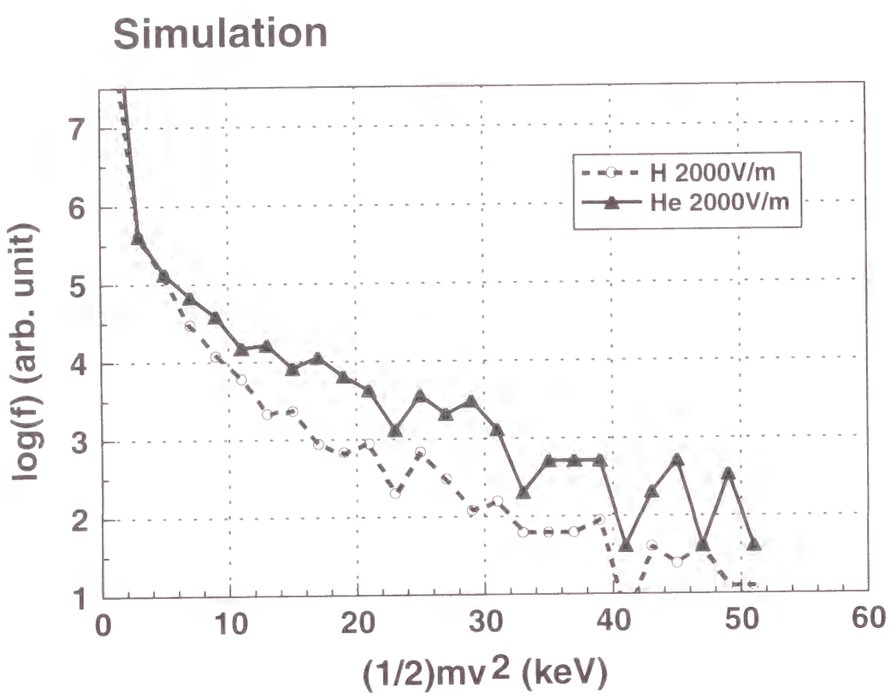

Fig. 6.4. The velocity distributions for the protons and for the helium 3 ions calculated by the Monte Carlo code (Number of the fast ions = 5,000, RF power = 1.3 MW, $n_e(0) = 4\times10^{19}$ m^{-3}, $T_e(0)$ = 500 eV). The tail temperatures estimated from the derivatives in the range from 15 keV to 35 keV are 16 keV for $^3He^{2+}$ and 13 keV for protons.

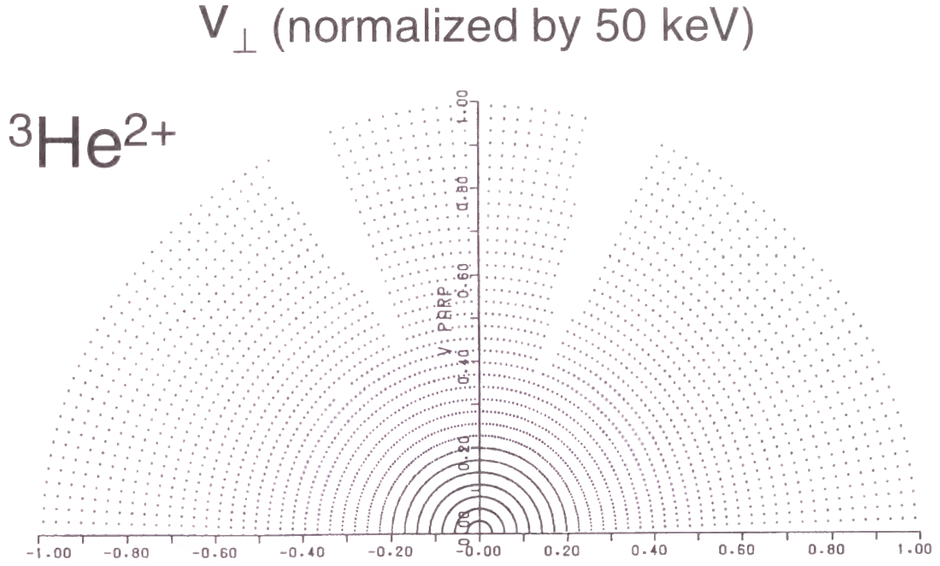

Fig. 6.5(a). The loss cones are shown for the ^3He ions, which start at $r/a_p = 0.5$ on the outer equatorial plane of Heliotron E. The energy is normalized by 50 keV. Here the values of the minimum energy of the loss cone, E_{min}, are 9 keV in the $v_{//} < 0$ region and 7 keV for $v_{//} > 0$ region.

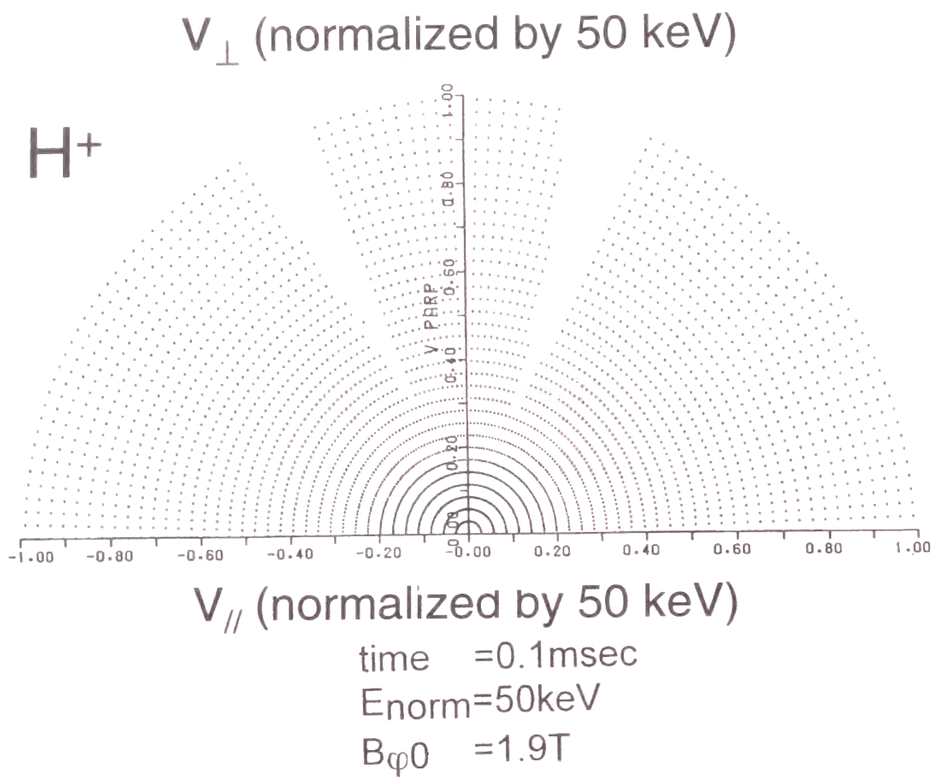

Fig. 6.5(b). The loss cones are shown for the protons, which start at $r/a_p = 0.5$ on the outer equatorial plane of Heliotron E. The energy is normalized by 50 keV. Here the values of the minimum energy of the loss cone, E_{min}, are 5 keV in the $v_{//} < 0$ region and 4 keV for $v_{//} > 0$ region.

Chapter 7

Conclusion

The minority-heating experiment was carried out in order to study the fast-ion production and confinement in Heliotron E. The ICRF antenna development was one of the key issues for this study. To improve the antenna-plasma coupling, the novel twisted antenna was developed for the minority-heating scheme in Heliotron E. The plasma loading resistance of this antenna was confirmed to be about 1 Ω, which was large enough to introduce large RF power into the vacuum chamber without causing high voltage break-down. The maximum input power of 2 MW could be radiated to the plasma with the eight-antenna system. The impurity increment during the ICRF pulse was kept small with the graphite side guards that were installed on the both sides of each pair of antennas as shown in Sec. 2.5.3.

A particular concern for the ICRF heating was about fast ions. The study on the behavior of the fast ions is very important for the reactor oriented research since the fusion rate enhancement by the high-energy tail as well as the plasma heating by the fusion alpha particles should be utilized in the reactor plasmas. It is noted that the ICRF heating experiment has an advantage for studying the confinement of fast ions since the ICRF heating can easily produce the fast ions whose energy is much higher than that of the neutral beam injection (NBI) heating. For the first time in this investigation, the applicability of the ICRF heating in the heliotron/torsatron device was demonstrated in such a way that the high-energy ions up to 100 keV could be produced and confined

efficiently. These fast ions had enough energy to study the dynamics of the fusion alpha particles as the experimental simulation study by adjusting the ratio between the Larmor radius to the plasma minor radius.

In this thesis, the condition of the formation of the high-energy tail by ICRF heating was clarified experimentally and numerically. The high-energy tail was produced more efficiently at the larger input power and the lower density. The high-energy tail was observed to be produced at densities lower than 2×10^{19} m^{-3}. This threshold density will be increased when the larger heating power is radiated without the increase of impurity and the degradation of the plasma confinement. In Heliotron E, the high-energy ion tail in the range of 10 - 30 keV was produced within 1msec after the injection of the ICRF pulse. After the termination of the ICRF pulse, the decay time of the high-energy ion fluxes was observed to be several milliseconds. However, this decay time was much shorter than that expected from Coulomb collisions.

A Monte Carlo code for simulating the fast-ion behavior in the ICRF heating of Heliotron E was developed. In this code, the ICRF wave acceleration, the collisional processes and the orbit following were included consistently. The velocity distributions, the time evolution of tail formation and the flux decay time after the termination of ICRF wave from the Monte Carlo simulation agreed well with those of the ICRF experiments in Heliotron E. For the estimation of the orbit loss, the combination of the Coulomb collisions and the orbit following were found to be essential because the loss cone structure was dependent on the particle position in real space. The key point was to solve both the collision processes and the orbit following under the acceleration by the ICRF wave. The orbit loss was the dominant energy loss channel for the fast ions near

100 keV and this loss was the origin of the reduced decay time of the fast ions in Heliotron E. For the high density regime, according to the decrease of the tail ion energy due to the energy transfer to the bulk plasma by the collisional processes, the orbit loss was gradually decreased. It was also found that the deposition ratio is a function of the RF power while it is also a function of the plasma density at constant RF power, because the high-energy tail formation significantly depends on the plasma density.

In the minority heating experiment in Heliotron E, the higher ion temperature was obtained in the ^{3}He-minority case than in the H-minority case. The increment of the bulk ion temperature of 800 eV at the line average density of 2×10^{19} m^{-3} was achieved in the ^{3}He-minority case. The results of the Monte Carlo simulation also provided a qualitative explanation of the experimental results. The heating efficiency in the ^{3}He-minority case by the Monte Carlo simulation was also found to be better than that in the H-minority case. However, it was noted that the orbit loss is relatively large in the high power range for both minority species in Heliotron E.

The effective heating and the fast ion production was carried out successfully by the ICRF minority heating in Heliotron E using the twisted fast wave antennas. The developed technology of the ICRF antenna optimization in the helical system is considered to be useful for its application to the larger-scale helical devices. In the LHD device, the twisted type antenna has been applied for the fast wave heating. The developed Monte Carlo code has also been utilized for the estimation of the efficiency in the minority heating in LHD. However, the influence of the orbit loss on the fast ion confinement and the heating efficiency was found to be significant especially in the high power range in Heliotron E. The improvement of the fast ion confinement in the helical

devices remains to be the key issue of ICRF heating from the viewpoint of the fusion-oriented research.

References

[1] KONDO, S., J. Fusion Energy, **3** (1983) 471.

[2] MIYAMOTO, K., "Plasma Physics for Nuclear Fusion", MIT press, Cambridge (1989).

[3] THOMPSON, W.B., Proc. Phys. Soc., Section B **70** (1957) 1.

[4] LAWSON, J.D., ibid., 6.

[5] SPITZER, Jr., L., Phys. Fluids **1** (1958) 253.

[6] ARTSIMOVICH, L.A., Nucl. Fusion **12** (1972) 215.

[7] PEASE, R.S., Plasma Phys. Contr. Fusion **28** (1986) 397.

[8] YAMANAKA, C., in Plasma Physics and Controlled Nuclear Fusion Research 1982 (Proc. 9th Int. Conf. Baltimore, 1982), Vol. 3, IAEA, Vienna (1983) 473.

[9] REBUT, P.H., BARTLETT, D.V., BAUMEL, G., BEHRINGER, K., BEHRISCH, R., et al., in Plasma Physics and Controlled Nuclear Fusion Research 1984(Proc. 10th Int. Conf. London, 1984), Vol. 1, IAEA, Vienna (1985) 11.

[10] JET Team, Nucl. Fusion **32** (1992) 187.

[11] YOUNG, K.M., BELL, M., BLANCHARD, W.R., BRETZ, N., CECCHI, J., et al., Plasma Phys. Contr. Fusion **26** (1984) 11.

[12] HAWRYLUK, R.L., ADLER, H., ALLING, P., ANCHER, C., ANDERSON, H., et al., in Plasma Physics and Controlled Nuclear Fusion Research 1994 (Proc. 17th Int. Conf. Seville, 1994), Vol. 1, IAEA, Vienna (1995) 11.

[13] YOSHIKAWA, M., ABE, T., AIKAWA, H., AKAOKA, A., AKASAKA, H., et al., in Plasma Physics and Controlled Nuclear Fusion Research 1986 (Proc. 11th Int. Conf. Kyoto, 1986), Vol. 1, IAEA, Vienna (1987) 11.

[14] USHIGUSA, K. and JT-60 TERM, in Fusion Energy 1996 (Proc. 16th Int. Conf. Montreal, 1996), Vol. 1, IAEA, Vienna (1997) 37.

[15] MCGUIRE, K.M., BARNES, C.W., BEER, M.A., BELL, M.G., BELL, R.E., et al., ibid., 19.

[16] AYMAR, R., CHUYANOV, V., MUGUET, M., PARKER, R., SHIMOMURA, Y., et al., ibid., 3.

[17] KOLESNICHENKO, YA.I., Nucl. Fusion **20** (1980) 727.

[18] UO, K., IIYOSHI, A., OBIKI, T., MOTOJIMA, O., MORIMOTO, S., et al., in Plasma Physics and Controlled Nuclear Fusion Research 1984 (Proc. 10th Int. Conf. London, 1984), Vol. 2, IAEA, Vienna (1985) 383.

[19] BAKAEV, V.V., BONDARENKO, S.P., BRONNIKOV, V.V., VOJTSENYA, V.S., VASIL'EV, M.P., et al., ibid., 397.

[20] BLAUMOSER, M., CATTANEI, G., CAVALLO, A., DORST, D., ELSNER, A., et al.., in Plasma Physics and Controlled Nuclear Fusion Research 1976 (Proc. 6th Int. Conf. Berchtesgaden, 1976), Vol. 2, IAEA, Vienna (1977) 81.

[21] AKULINA, D.K., ANDRYUKHINA, Eh.D., BEREZHETSKIJ, M.S., BLOKH, M.A., VORONOV, G.S., et al., ibid., 115.

[22] UO, K., IIYOSHI, A., YOSHIOKA, Sh., ISHIDA, T., KONOSHIMA, Sh., et al., in Plasma Physics and Controlled Nuclear Fusion Research 1970 (Proc. 4th Int. Conf. Madison, 1970), Vol. 3, IAEA, Vienna (1971) 109.

[23] UO, K., IIYOSHI, A., OBIKI, T., MORIMOTO, S., SASAKI, A., et al., in Plasma Physics and Controlled Nuclear Fusion Research 1976 (Proc. 6th Int. Conf. Berchtesgaden, 1976), Vol. 2, IAEA, Vienna (1977) 103.

[24] MOTOJIMA, O., MUTOH, T., SATO, M., ZUSHI, H., OKADA, H., et al., in Plasma Physics and Controlled Nuclear Fusion Research 1988 (Proc. 12th Int. Conf. Nice, 1988), Vol. 1, IAEA, Vienna (1989) 551.

[25] UO, K., IIYOSHI, A., OBIKI, T., MORIMOTO, S., WAKATANI, M., et al., in Plasma Physics and Controlled Nuclear Fusion Research 1980 (Proc. 8th Int. Conf. Brussels, 1980), Vol. 1, IAEA, Vienna (1981) 217.

[26] IIYOSHI, A., in Fusion Engineering 1989 (Proc. 13th Symp. Knoxville, 1989), Vol.2, IEEE, New York (1990) 1007.

[27] SALTMARSH, M.J., ANDERSON, F.S.B., BELL, G.L., BELL, J.D., BIGELOW, T.S., et al., in Plasma Physics and Controlled Nuclear Fusion Research 1988 (Proc. 12th Int. Conf. Nice, 1988), Vol. 2, IAEA, Vienna (1989) 349.

[28] MATSUOKA, K., KUBO, S., HOSOKAWA, M., TAKITA, Y., OKAMURA, S., et al., ibid., 411.

[29] BEIDLER, C.D., BESEDIN, N.T., BYKOV, V.E., CARRERAS, B.A., DOMINGUEZ, N., et al., in Plasma Physics and Controlled Nuclear Fusion Research 1990 (Proc. 13th Int. Conf. Washington D.C., 1990), Vol. 2, IAEA, Vienna (1991) 663.

[30] ALEJALDRE, C., ALONSO, J., BOTIJA, J., CASTEJÓN, F., CEPERO, J.R., et al., Fusion Technol. **17** (1990) 131.

[31] BLACKWELL, B.D., BORG, G.G., DEWAR, R.L., GARDNER, H.J., HAMBERGER, S.M., et al., in Plasma Physics and Controlled Nuclear Fusion Research 1994 (Proc. 15th Int. Conf. Seville, 1994), Vol. 2, IAEA, Vienna (1995) 337.

[32] BROSSMANN, U., DOMMASCHK, W., HERRNEGGER, F., GRIEGER, G., KISSLINGER, J., et al., in Plasma Physics and Controlled Nuclear Fusion Research 1982 (Proc. 9th Int. Conf. Baltimore, 1982), Vol. 3, IAEA, Vienna (1983) 141.

[33] GRIEGER, G., BEIDLER, C., HARMEYER, E., JUNKER, J., KISSLINGER, J., et al., in Plasma Physics and Controlled Nuclear Fusion Research 1988 (Proc. 12th Int. Conf. Nice, 1988), Vol. 2, IAEA, Vienna (1989) 369.

[34] IIYOSHI, A., MOTOJIMA, O., SATO, M., MUTOH, T., SUDO, S., et al., in Plasma Physics and Controlled Nuclear Fusion Research 1984 (Proc. 10th Int. Conf. London, 1984), Vol. 1, IAEA, Vienna (1985) 453.

[35] MUTOH, T., MOTOJIMA, O., SATO, M., OKADA, H., ZUSHI, H., et al., in Plasma Physics and Controlled Nuclear Fusion Research 1986 (Proc. 11th Int. Conf. Kyoto, 1986), Vol. 2, IAEA, Vienna (1987) 473.

[36] UO, K., IIYOSHI, A., OBIKI, T., MOTOJIMA, O., MORIMOTO, S., et al., in Plasma Physics and Controlled Nuclear Fusion Research 1982 (Proc. 9th Int. Conf. Baltimore, 1982), Vol. 2, IAEA, Vienna (1983) 209.

[37] JACQUINOT, J., BHATNAGAR, V.P., BURES, M., COTTRELL, G.A., ERIKSSON, L.G., et al., in Plasma Physics and Controlled Nuclear Fusion Research 1990 (Proc. 13th Int. Conf. Washington D.C., 1990), Vol. 1, IAEA, Vienna (1991) 679.

[38] TAYLER, G., MURAKAMI, M., ADLER, H., BELL, M.G., BRETZ, N.L., et al., in Plasma Physics and Controlled Nuclear Fusion Research 1994 (Proc. 15th Int. Conf. Seville, 1994), Vol. 1, IAEA, Vienna (1995) 431.

[39] SAIGUSA, M., KIMURA, H., FUJII, T., MORIYAMA, S., SATO, M., et al., ibid.,

453.

[40] IIYOSHI, A., OBIKI, T., SATO, M., SASAKI, A., MUTOH, T., et al., in Theoretical and Experimental Aspects of Heating of Toroidal Plasmas 1976 (Proc. 3rd Int. Meeting Grenoble, 1976), Vol. 2 (1976) 305.

[41] BROWM, I.G., ROTHMAN, M.A., and SINCLAIR, R.M., Phys. Fluids **12** (1969) 1318.

[42] ROTHMAN, M.A., SINCLAIR, R.M., BROWN, I.G., and HOSEA, J.C., ibid., 2211.

[43] HOSEA, J.C. and HOOKE, W.M., Phys. Rev. Lett. **31** (1973) 150.

[44] ONO, M., WONG, K.L., and WURDEN, G.A., Phys. Fluids **26** (1983) 298.

[45] ADAM, J. and SAMAIN, A., Report EUR-CEA-FC579 (1971), Association Euratom-CEA, Fontenay-aux-Roses.

[46] ADAM, J., CHANCE, M., EUBANK, H., GETTY, W., HINNOV, E., et al., in Plasma Physics and Controlled Nuclear Fusion Research 1974 (Proc. 5th Int. Conf. Tokyo, 1974), Vol. 1, IAEA, Vienna (1975) 65.

[47] BUCHSBAUM, S.J., Phys, Fluids **3** (1960) 418.

[48] KWON, M., SHEPARD, T.D., GOULDING, R.H., THOMAS, C.E., COLCHIN, R.J., et al., Nucl. Fusion **32** (1985) 1225.

[49] MUTOH, T., OKADA, H., MOTOJIMA, O., MORIMOTO, S., SATO, M., et al., Nucl. Fusion.**24** (1984) 1003.

[50] FUKUYAMA, A., OKAZAKI, N., GOTO, A., ITOH, S.-I., and ITOH, K., Nucl. Fusion **26** (1986) 151.

[51] OKADA, H., KOTANI, T., MUTOH, T., SANO, F., KONDO, K., et al., J. Plasma

and Fusion Res. SERIES, **1** (1998) 322.

[52] THEILHABER, K. and JACQUINOT, J., Nucl. Fusion **24** (1984) 541.

[53] OKADA, H., MUTOH, T., ZUSHI, H., OKAMOTO, M., OHNISHI, M., et al., Nucl. Fusion **36** (1996) 465.

[54] OHNISHI, M., OKAMOTO, M., ABE, Y., FUKUYAMA, A., MUTOH, T., and IIYOSHI, A., Report IPPJ-884 (1988), Inst. of Plasma Physics, Nagoya University, Nagoya.

[55] ROSENBLUTH, M.N., MACDONALD, W.M., and JUDO, D.L., Phys. Rev. **107** (1957) 1.

[56] OKADA, H., MUTOH, T., OKAMOTO, M., OHNISHI, M., FUKUYAMA, A., et al., Fusion Eng. and Design **26** (1995) 173.

[57] EMMERT, G.A. and PARKER, R., Fusion Tech. **21** (1992) 2284.

[58] UO, K., NAKASUGA, M., and HANATANI, K., Report PPLK-3 (1982), Plasma Physics Laboratory, Kyoto University, Uji.

[59] GIBSON, A. and MASON, D.W., Plasma Physics **11** (1969) 121.

[60] WAKATANI, M, Nucl. Fusion **23** (1983) 817.

[61] ZUSHI, H., KURIMOTO, Y., TANIGUCHI, S., SANO, F., WAKATANI, M., et al., in Plasma Physics and Controlled Nuclear Fusion Research 1992 (Proc. 14th Int. Conf. Würzburg, 1992), Vol. 2, IAEA, Vienna (1993) 597.

[62] ZUSHI, H., NAKASHIMA, Y., KONDO, K., IIYOSHI, A., and UO, K., J. Phys. Soc. Jpn. **51** (1982) 2673.

[63] SIRE, G., GERLACH, P., KALFON, C., et al., in Fusion Engineering 1983 (Proc. 10th Symposium Philadelphia), Vol. 1, IEEE, New York (1983) 1701.

[64] ODAJIMA, K., KIMURA, H., MATSUMOTO, H., YAMAMOTO, T., and IIZUKA, S., Report JAERI-M 9217 (1980), JAERI, Tokai.

[65] SOUTHWORTH, G.C., "Principles and Applications of Waveguide Transmission", D. Van Nostrand, Princeton (1950).

[66] Equip TFR, in Plasma Physics and Controlled Nuclear Fusion Research 1976 (Proc. 6th Int. Conf. Berchtesgaden, 1976), Vol. 3, IAEA, Vienna (1977) 39.

[67] KIMURA, H., ODAJIMA, K., IIZUKA, S., SENGOKU, S., SUGIE, T., et al., in Plasma Physics and Controlled Nuclear Fusion Research 1980 (Proc. 8th Int. Conf. Brussels, 1980), Vol. 2, IAEA, Vienna (1981) 105.

[68] MUTOH, T., Doctoral Thesis, Kyoto University, Kyoto (1984).

[69] ADAM, J., Report EUR-CEA-FC-1004 (1979), Association Euratom-CEA, Fontenay-aux-Roses.

[70] MULLEN, J.H. and DAVIS, J.W., IEEE Trans. Plasma Sci. **12** (1984) 79.

[71] NISHIMURA, K., KUMAZAWA, R., MUTOH, T., WATARI, T., SEKI, T., et al. in Plasma Physics and Controlled Nuclear Fusion Research 1994 (Proc. 15th Int. Conf. Seville, 1994), Vol. 1, IAEA, Vienna (1995) 783.

[72] MUTOH, T., KUMAZAWA, R., SEKI, T., SIMPO, F., NOMURA, G., et al., Plasma and Fusion Res. SERIES, **1** (1998) 334.

[73] WILSON, J.R., BELL, M.G., CAVALLO, A., COLESTOCK, P.L., DORLAND, et al., in Plasma Physics and Controlled Nuclear Fusion Research 1988 (Proc. 12th Int. Conf. Nice, 1988), Vol. 1, IAEA, Vienna (1989) 691.

[74] NOTERDAEME, J.-M., WUKITCH, S., HARTMANN, D.A., BRAMBILLA, M., BRAUN, F., et al., in Fusion Energy 1996 (Proc. 16th Int. Conf. Montreal, 1996),

Vol. 3, IAEA, Vienna (1997) 335.

[75] OBIKI, T., SANO, F., KONDO, K., ZUSHI, H., HANATANI, K., et al., in Fusion Energy 1996 (Proc. 16th Int. Conf. Montreal, 1996), Vol. 2, IAEA, Vienna (1997) 13.

[76] KURIMOTO, Y., ZUSHI, H., SANO, F., KONDO, K., MIZUUCHI, T., et al., J. Phys. Soc. Jpn. **66** (1997) 2033.

[77] JASSBY, D.L., Nucl. Fusion **17** (1977) 309.

[78] MYNICK, H.E., Phys. Fluids **26** (1983) 1008.

[79] HANATANI, K., WAKATANI, M., and UO, K., Nucl. Fusion **21** (1981) 1067.

[80] TAKAHASHI, H., J. Phys., Colloq. **38** (1977) C6-171.

[81] HOSEA, J., BERNABEI, S., COLESTOCK, P., DAVIS, S.L., EFTHIMION, P., et al., Phys. Rev. Lett. **43** (1979) 1802.

[82] SUDO, S., KONDO, K., MUTOH, T., ZUSHI, H., IIYOSHI, A., and UO, K., J.J.A.P. **22** (1983) 485.

[83] TALMADGE, J.N., ZUSHI, H., SUDO, S., MUTOH, T., SATO, M., et al., Phys. Rev. Lett. **52** (1984) 33.

[84] KONDO, K., ODA, T., OKADA, H., ZUSHI, H., et al., J.J.A.P. **27** (1988) 1287.

[85] HEALD, M.A. and WHARTON, C., B., "Plasma Diagnostics with Microwaves", John Wiley & Sons., New York (1965).

[86] VERON, D., "Submillimeter Interferometry of High Density Plasmas in Infrared and Millimeter Waves", Vol.II, Academic Press, New York (1979).

[87] KONDO, K., ZUSHI, H., NISHIMURA, S., KANEKO, H., SATO, M., et al., Rev. Sci. Instrum. **59** (1988) 1533.

[88] STIX, T.H., Nucl. Fusion **15** (1975) 737.

[89] SPITZER, Jr., L., "Physics of Fully Ionized Gases", Interscience, New York (1962).

[90] STIX, T.H., Plasma Phys. **14** (1972) 367.

[91] Lotz, W., Astrophys. J. Supple. Ser. No. 128, **14** (1967) 207.

[92] OKANO, D., UCHINO, K., SHIMIZU, A., MURAOKA, K., MAEDA, M., et al., J. Nucl. Mater. **145-147** (1987) 504.

[93] BOOZER, A.H., Phys. Fluids **23** (1980) 904.

[94] BOOZER, A.H. and KUO-PETRAVIC, G., Phys. Fluids **24** (1981) 851.

[95] MURAKAMI, S., OKAMOTO, M., NAKAJIMA, N., OHNISHI, M., and OKADA, H., Nucl. Fusion **34** (1994) 913.

[96] HANATANI, K., NAKASHIMA, Y., ZUSHI, H., SANO, F., MOTOJIMA, O., et al., Nucl Fusion **25** (1985) 259.

[97] MORZOV, A.I. and SOLOV'EV, L.S., in "Review of Plasma Physics" Vol.2, edited by LEONTOVICH, M.A., Consultants Bureau, New York (1966).

[98] HINTON, F.L. and HAZELTINE, R.D., Rev. Modern Phys. **48** (1976) 239.

[99] GAFFY, Jr., J.D., J. Plasma Phys. **16** (1976) 149.

[100] KRUSKAL, M.D. and BERNSTEIN, I.B., Phys. Fluids **7** (1964) 407.

[101] BRAGINSKII, S.I., in "Review of Plasma Physics" Vol.1, edited by LEONTOVICH, M.A., Consultants Bureau, New York (1965).

[102] STIX, T.H., "The Theory of Plasma Waves", McGraw-Hill, New York (1962).

[103] FURTH, H.,P. and ROSENBLUTH, M.N., in Plasma Physics and Controlled Nuclear Fusion Research 1968 (Proc. 3rd Int. Conf. Novosibirsk, 1968), Vol.1, IAEA,

Vienna (1969) 821.

[104] ITOH, K., ITOH, S.-I., FUKUYAMA, A., and HANATANI, K., Nucl. Fusion **29** (1989) 1851.

[105] OBIKI, T., MIZUUCHI, T., ZUSHI, H., KONDO, K., SANO, F., et al., in Plasma Physics and Controlled Nuclear Fusion Research 1988 (Proc. 12th Int. Conf. Nice, 1988), Vol.2, IAEA, Vienna (1989) 337.

[106] HANATANI, K., SANO, F., TAKEIRI, Y., KONDO, K., ZUSHI, H., et al., in Controlled Fusion and Plasma Physics 1987 (Proc. 14th Europ. Conf. Madrid 1987), Vol. 11 D Part 1, EPS (1987) 396.

[107] HOSEA, J.C., BOYD, D., BRETZ, N., CHRIEN, R., CHOEN, S., et al., in Plasma Physics and Controlled Nuclear Fusion Research 1980 (Proc. 8th Int. Conf. Brussels, 1980), Vol. 2, IAEA, Vienna (1981) 95.

[108] JACQUINOT, J., SADLER, G.J., and the JET TEAM, Fusion Technol. **21** (1992) 2254.

[109] WAKATANI, M., KODAMA, S., NAKASUGA, M., and HANATANI, K., Nucl. Fusion **21** (1981) 175.

[110] ROME, J.A., MCALEES, D.G., CALLEN, J.D., and FOWLER, R.H., Nucl. Fusion **16** (1076) 55.

[111] KULCINSKI, G.L., BLANCHARD, J.P., and EL-GUEBALY, L.A., Fusion Technol. **21** (1992) 2292.

[112] BESPOLUDENNOV, S.G., KHRIPUNOV, V.I., PISTUNOVICH, V.I., EMMERT, G.A., SANTARIUS, J.F., and KULCINSKI, G.L., in Plasma Physics and Controlled Nuclear Fusion Research 1992 (Proc. 14th Int. Conf. Würzburg, 1992), Vol. 3, IAEA, Vienna (1993) 311.

List of Publications

Chapter 2

[1] OKADA, H., KOTANI, T., MUTOH, T., SANO, F., KONDO, K., WAKATANI, M., and OBIKI, T., "Numerical Analysis of Small Movable ICRF Antenna Loading Resistance in Heliotron E", J. Plasma and Fusion Res. SERIES, **1** (1998) 322.

Chapter 3

[2] MUTOH, T., MOTOJIMA, O., SATO, M., OKADA, H., ZUSHI, H., KONDO, K., NODA, N., KANEKO, H., MIZUUCHI, T., BESSHOU, S., SANO, F., SUDO, S., TAKEIRI, Y., AKAISHI, K., KAWABATA, T., IJIRI, Y., ITOH, K., MORIMOTO, S., IIYOSHI, A., and UO, K., "ICRF Heating of Currentless Plasma in Heliotron E", in Plasma Physics and Controlled Nuclear Fusion Research 1986 (Proc. 11th Int. Conf. Kyoto, 1986), Vol. 2, IAEA, Vienna (1987) 473.

[3] MUTOH, T., OKADA, H., MOTOJIMA, O., MORIMOTO, S., SATO, M., ZUSHI, H., KONDO, K., SUDO, S., BESSHOU, S., MIZUUCHI, T., KANEKO, H., SANO, F., IIMA, M., OBIKI, T., IIYOSHI, A., and UO, K., "ICRF Heating of Currentless Plasma in Heliotron E", Nucl. Fusion **24** (1984) 1003.

[4] MOTOJIMA, O., MUTOH, T., SATO, M., ZUSHI, H., OKADA, H., NODA, N., KANEKO, H., MIZUUCHI, T., KONDO, K., SUDO, S., TAKEIRI, Y., SANO, F., ITOH, K., MORIMOTO, S., HANATANI, K., AKAISHI, K., OBIKI, T., IIYOSHI, A., YANAGI, N., BESSHOU, S., KOBAYASHI, S., IIMA, M., ICHIGUCHI, K.,

and WAKATANI, M., "High Power ECRH and ICRF Heating in the Heliotron E and DR Devices", in Plasma Physics and Controlled Nuclear Fusion Research 1988 (Proc. 12th Int. Conf. Nice, 1988), Vol. 1, IAEA, Vienna (1989) 551.

Chapter 4

[5] MURAKAMI, S., OKAMOTO, M., NAKAJIMA, N., OHNISHI, M., and OKADA, H., "Monte Carlo Simulation Study of ICRF Minority Heating in the Large Helical Device", Nucl. Fusion **34** (1994) 913.

Chapter 5

[6] OKADA, H., MUTOH, T., ZUSHI, H., OKAMOTO, M., OHNISHI, M., KONDO, K., MIZUUCHI, T., BESSHOU, S., SANO, F., NAGASAKI, K., WAKATANI, M., and OBIKI, T., "Study of High Energy Particles Produced by ICRF Heating in Heliotron-E", Nucl. Fusion **36** (1996) 465.

Chapter 6

[7] OKADA, H., MUTOH, T., OKAMOTO, M., OHNISHI, M., FUKUYAMA, A., ZUSHI, H., KONDO, K., MIZUUCHI, T., BESSHOU, S., SANO, F., NAGASAKI, K., WAKATANI, M., and OBIKI, T., "Ion Cyclotron Range of Frequency Heating with Hydrogen and Helium Minority Species in Heliotron E", Fusion Eng. and Design **26** (1995) 173.